COMPUTATIONAL MODELING OF GEOMETRY DEPENDENT PHONON TRANSPORT IN SILICON NANOSTRUCTURES

Drew A. Cheney

A DISSERTATION

in

Mechanical Engineering and Applied Mechanics

Presented to the Faculties of the University of Pennsylvania

in

Partial Fulfillment of the Requirements for the

Degree of Doctor of Philosophy

2013

Supervisor of Dissertation

_____

Dr. Jennifer R. Lukes
Associate Professor, Mechanical Engineering and Applied Mechanics

Graduate Group Chairperson

_____

Dr. Prashant K. Purohit
Associate Professor, Mechanical Engineering and Applied Mechanics

Dissertation Committee

Dr. John L. Bassani, Professor, Mechanical Engineering and Applied Mechanics

Dr. Vaclav Vitek, Professor, Materials Science and Engineering

Dr. Jennifer R. Lukes, Associate Professor, Mechanical Engineering and Applied Mechanics

ACKNOWLEDGMENT

I would like to thank Professor Jennifer Lukes for proposing and guiding this research project. She has been integral in my graduate study from the beginning and made many contributions to this dissertation and the technical papers from which it is based. She has been a consistent source of positive energy, encouragement, and advice about technical, academic, and career matters. I consider myself very lucky to have been one of her students.

I am also very grateful for the camaraderie and research support given to me by the current and former members of Professor Lukes' research group: Anuj Chaudhri, Jack Franklin, Neil Zuckerman, Ian Cosden, Mehdi Zanjani, Paul Barclay, and Ruiyuan Ma. Neil, Ian, and Mehdi were especially helpful to me as I worked through technical difficulties related to phonon physics, computational modeling, and mathematics.

I would also like to thank Professor John Bassani and Professor Vaclav Vitek for serving on my dissertation committee, the engineering and materials science faculty from which I learned so much, the MEAM staff for assisting with all of the logistics that go with graduate study, and all the students that make up the MEAM community.

A very special thanks should be given to my wife and best friend Eleanor Peacock. She has been my number one supporter in my graduate study and has always encouraged me and helped me keep things in perspective. I am incredibly grateful for the

support given to me by my parents, parents-in-law, and my broader network of family and friends.

This work has been funded by the Air Force Office of Scientific Research and the National Science Foundation.

ABSTRACT

COMPUTATIONAL MODELING OF GEOMETRY DEPENDENT PHONON TRANSPORT IN SILICON NANOSTRUCTURES

Drew A. Cheney

Dr. Jennifer R. Lukes

Recent experiments have demonstrated that thermal properties of semiconductor nanostructures depend on nanostructure boundary geometry. Phonons are quantized mechanical vibrations that are the dominant carrier of heat in semiconductor materials and their aggregate behavior determine a nanostructure's thermal performance. Phonon-geometry scattering processes as well as waveguiding effects which result from coherent phonon interference are responsible for the shape dependence of thermal transport in these systems. Nanoscale phonon-geometry interactions provide a mechanism by which nanostructure geometry may be used to create materials with targeted thermal properties. However, the ability to manipulate material thermal properties via controlling nanostructure geometry is contingent upon first obtaining increased theoretical understanding of fundamental geometry induced phonon scattering processes and having robust analytical and computational models capable of exploring the nanostructure design space, simulating the phonon scattering events, and linking the behavior of individual

phonon modes to overall thermal behavior. The overall goal of this research is to predict and analyze the effect of nanostructure geometry on thermal transport. To this end, a harmonic lattice-dynamics based atomistic computational modeling tool was created to calculate phonon spectra and modal phonon transmission coefficients in geometrically irregular nanostructures. The computational tool is used to evaluate the accuracy and regimes of applicability of alternative computational techniques based upon continuum elastic wave theory. The model is also used to investigate phonon transmission and thermal conductance in diameter modulated silicon nanowires. Motivated by the complexity of the transmission results, a simplified model based upon long wavelength beam theory was derived and helps explain geometry induced phonon scattering of low frequency nanowire phonon modes.

TABLE OF CONTENTS

LIST OF TABLES

LIST OF FIGURES

1 Introduction

1.1 Experimental and Theoretical Background

In contrast to most conventional engineering materials, semiconductor nanostructures exhibit thermal properties that depend on their size and geometry. For example, it has been experimentally demonstrated that sub-micron structures such as suspended silicon thin films [1] silicon on insulator layers [2] , and silicon nanowires [3][4] have much lower thermal conductivities than bulk silicon. Depending on temperature and nanostructure size, thermal conductivity can be reduced by a factor of 100 or more when compared to bulk silicon. Researchers have also demonstrated that nanostructures with augmented surface roughness can exhibit even further decreased thermal conductivity when compared with smooth nanowires [5], [6]. More recent experiments have shown that more ordered nanostructure geometries also exhibit geometry dependent thermal properties. For example, silicon nanowires with a controlled, corrugated boundary topology can reduce the thermal conductance relative to a smooth nanowire by factor of up to approximately 60% [7] and serpentine shaped nanowires exhibit a thermal conductance that is reduced by a factor of about 30% [8].

The unique thermal behavior of nanostructures is a consequence of the behavior of the systems' phonons. Phonons are quantized lattice vibrations that are the dominant carrier of heat in dielectric solids and semiconductors. At most length scales, phonons scatter heavily before encountering a structure's boundary. As a result, phonon-boundary

interactions have negligible impact on thermal transport and the thermal conductivity of a material is independent of structure size and geometry. However, if the size of a structure is greatly reduced so that the mean free path of the phonon, which is the characteristic length the phonon travels before scattering, is comparable to the structure's size, phonon-boundary interactions can significantly influence phonon transport in the system and cause size and geometry dependent thermal properties.

Phonon-boundary interactions impact aggregate phonon transport and thermal properties of nanostructures in two ways. First, the increased surface area to volume ratios characteristic of nanostructures increases the incidence of boundary scattering which suppresses phonon transport and results in lower thermal conductivity. For regimes where boundary scattering dominates other phonon scattering mechanisms, the geometric details of the boundary can strongly influence the scattering process and result in thermal properties that not only depend on size, but also on nanostructure shape. Second, coherent reflections of phonons off of nanostructure boundaries cause phonon interference and results in phonon spectra that are different from bulk materials. This phenomenon is referred to as phonon confinement and causes nanostructures to function as phonon waveguides analogous to acoustic or electromagnetic waveguides. In contrast to phonon transport in bulk materials where the phonon modes can be described as decoupled longitudinal or transverse modes, the continuous reflection off of the boundaries gives rise to coupled mode types which are unique to structures with confined boundaries. Both the boundary/geometry scattering effect and the phonon confinement

effect give rise to the possibility of using nanostructure geometry to control phonon transport and potentially tune the thermal performance of a material.

1.2 Motivating Application: Thermoelectric Materials

A primary and potentially immediate application area for nanostructures with geometrically tuned thermal properties is in the creation of high efficiency thermoelectric materials. Thermoelectric materials directly convert temperature differences to electric voltage and vice-versa. These materials are useful in the direct generation of electric power from waste thermal energy or in highly reliable and lightweight solid-state refrigeration or electronics cooling applications. The performance of a thermoelectric material is characterized by its figure of merit [9]:

$$ZT = \frac{S^2 \sigma T}{\kappa} \tag{1}$$

Here, σ is the electrical conductivity, S is the Seebeck coefficient, T is the temperature, and κ is the thermal conductivity. Conventional and commercially available thermoelectric materials have a figure of merit of ~0.8 and operate at efficiencies of ~5-6% [9]. ZT values of 3-4 are required to become competitive with conventional compressor based generation and refrigeration technologies [9]. One strategy for obtaining enhanced thermoelectric materials is to use nanostructures that impede the transport of phonons and reduce thermal conductivity without adversely affecting the material's electrical properties. This can be done through manipulation of nanostructure

size and boundary geometry resulting in phonon confinement effects and increased boundary/geometry scattering. Recent experiments have shown that 52 nm diameter rough silicon nanowires fabricated by the electroless etching technique can increase *ZT* from the bulk Si value of around 0.01 to around 0.60 [5]. When compared against smooth nanowires synthesized using the vapor-liquid-solid technique, the rough nanowires exhibited improvement in Z*T* by a factor of 5-10. Similar increases in figure of merit were observed for 10 and 20 nm diameter silicon nanowires fabricated using the superlattice nanowire pattern transfer method [10].

1.3 Previous Work and Modeling Approaches:

The aforementioned experimental results indicate that controlled nanostructure geometry can be used to suppress phonon transport resulting in geometrically controlled thermal properties and potentially enabling the creation of nanostructured materials with enhanced thermoelectric performance. Moreover, recent advances in nanofabrication technology have enabled the creation of a myriad of different nanoscale geometries [11-21] that could potentially be used to tune phonon-geometry interactions in order to obtain desired overall thermal properties. However, the ability to design nanostructure geometry for optimally tuned thermal performance is contingent upon first obtaining increased theoretical understanding of fundamental geometry induced phonon scattering processes, having robust analytical and computational models capable of exploring the nanostructure design space, simulating the phonon scattering events, and linking the

behavior of individual phonon modes to overall thermal behavior. To these ends, researchers have investigated geometrical effects on phonon transport and thermal properties of nanostructures using a variety of approaches.

1.3.1 *Particle-Specularity Parameter Based Models*

The simplest manner in which nanostructure geometry can be included into a model for nanostructure thermal transport is by including boundary scattering in a particle based formulation for the thermal conductivity. For example, the thermal conductivity of a nanostructure or material, κ, under the relaxation time approximation, is expressed as a summation of the contributions of each phonon mode indexed by the phonon's wave vector, **k**, and mode type, ν [22]:

$$\kappa = \sum_{\mathbf{k}} \sum_{\nu} c v^2 (\mathbf{k}, \nu) \tau (\mathbf{k}, \nu) \tag{2}$$

Here, c is the phonon modal specific heat, v is the phonon group velocity and $\tau(\mathbf{k},\nu)$ is the phonon relaxation time. The relaxation time is the characteristic time it takes for a phonon to scatter and decay and has contributions from phonon-phonon scattering which is associated with anharmonic interatomic interactions, phonon-impurity scattering, and phonon-boundary scattering. If phonon coherence is neglected and phonons are modeled as particles, the effective mean free path for boundary scattering in nanowires, L_B, is commonly expressed as $L_B = \frac{1+p}{1-p} D$ [23] where D is the nanowire diameter and p is the specularity parameter. The specularity parameter quantifies the degree to which phonon

scattering is specular (p=1) or diffuse (p=0) and is commonly calculated using the formula of Ziman as $p = \exp\left(-16\pi\delta^2/\lambda_{ph}\right)$ [23] where δ is the root mean square surface roughness and λ_{ph} is the phonon wavelength. The relaxation time can be calculated by dividing the mean free path by the phonon group velocity and combining with other scattering mechanisms such as phonon-phonon scattering and impurity scattering via use of Matthiessen's rule. That is, the inverse of the total relaxation time is equal to the sum of scattering rates associated with each process. In this way, two parameters, the nanowire diameter and the root mean square surface roughness, can be used to predict the geometry effects on nanostructure thermal conductivity.

Coarse changes in nanostructure boundary geometry can be modeled by including the specularity parameter model within a Monte Carlo (MC) particle tracking approach that includes irregular domain boundaries and solves for steady-state spatially dependent phonon populations and uses the phonon populations to extract the thermal conductivity. For example, Moore, *et al*. [24] adapted a MC model used for the calculation of thermal conductivity of straight silicon nanowires [25] for the calculation of thermal conductivity in symmetric sawtooth nanowires. Their work showed that periodic sawtooth patterning of nanowires can induce significant phonon backscattering and reduce the thermal conductivity below the diffuse surface limit ($\kappa_{diffuse}$). The diffuse surface limit refers to thermal conductivity obtained via purely diffuse phonon boundary scattering (p=0). In this limit the mean free path due to boundary scattering is equal to the nanowire diameter. In MC models for nanowire thermal conductivity that employ only a specularity

parameter and flat surface, thermal conductivity below $\kappa_{diffuse}$ can only be attained with specularity parameter between -1 and 0. Roberts and Walker used a similar approach to explore phonon transport in asymmetric sawtooth nanowires [26]. The model in their study was executed such that right traveling phonons scattered specularly from sawtooth facets while boundary scattering of left traveling phonons was either specular or diffuse depending on a probability determined by a specularity parameter. Their study showed that directionally dependent thermal conductivity is possible at lower temperatures and when one side of a sawtooth facet is treated as rough enough to induce frequency dependent diffuse roughness scattering.

The utility of these particle-specularity parameter based approaches is limited by the fact that they are only appropriate for modeling nanostructure surfaces with effectively random roughness. Though the MC approach enables coarse changes in nanostructure boundary geometry by allowing boundary surfaces to change orientation, each individual surface is still treated as being effectively rough. In addition, in the most rigorous calculation of phonon boundary scattering, specific mode dependency on scattering would be taken in account. However, in practice, most models for boundary scattering, including the aforementioned Ziman model, use simplified expressions for phonon mean free path that may only depend on one or a few phonon properties. This approach does not account for scattering that may vary between different phonon modes of the same wavelength (e.g. longitudinal or transverse phonon modes). Furthermore, since this approach is formulated based on the assumption that the phonons can be

modeled as particles, bulk type phonon propagation is assumed and phonon interference and waveguiding effects are neglected.

1.3.2 *Molecular Dynamics Models*

A much more detailed and realistic manner in which geometry effects can be included in the investigation of geometry dependent nanostructure thermal properties is through molecular dynamics (MD) simulation [27]. The MD approach models a nanostructure as a collection of classically behaving point particles. Empirical potential functions are used to model interatomic forces and particle trajectories are obtained by solving classical equations of motion using explicit numerical methods. Heat fluxes and temperature gradients can be directly modeled in MD and used to calculate nanostructure thermal properties such as thermal conductivity. Since molecular dynamics simulation models each atom individually, effects associated with wave coherence and specific mode dependence are implicitly included. Atomic level geometric detail and effects such as lattice strain can also be included. There is a great body of MD based research on thermal properties and phonon behavior in nanostructures. Among these are studies of size effects on phonon transport in confined nanostructures including silicon thin films [28], silicon nanowires [29-31], and carbon nanotubes [32].

In addition, there has been some limited MD research that has specifically probed boundary geometry. For example, Liu and Chen [34] investigated the effect of periodic ripple roughness on the thermal conductivity of silicon nanowires with square cross-

section. Their results showed that patterned roughness can significantly reduce the thermal conductivity of nanowires and that the reduction is greater for roughness of smaller wavelength and larger amplitude. Qiu, et. al performed a similar study on Bi_2Te_3 nanowires and found that roughness can produce a 35% reduction in thermal conductivity versus a smooth wire for a 5.2 nm diameter case [35]. An analytical model fitted to their MD produced data showed that the primary cause for thermal conductivity reduction in atomically smooth wires was strong phonon confinement resulting in "softening" of the phonon dispersion curve. Both phonon confinement and strong phonon scattering from roughness were the causes for reduced thermal conductivity in the rough nanowires. MD studies of smooth and rough graphene nanoribbons have also highlighted the ability of surface roughness to reduce thermal conductivity [36]. In another study, He and Galli calculated the room temperature thermal conductivity of 15 nm diameter silicon nanowires with 1.5 nm deep silica rippled surface and showed that the thermal conductivity of the rippled nanowire was reduced by approximately 90% versus the value calculated for the smooth silica free nanowire and a reduction of around 60% versus a nanowire with an amorphous silica layer [38]. From an analysis of the nanowire's vibrational density of states, they deduced that phonon scattering at all frequencies plays a role in the thermal conductivity reduction. Termentzidis et al. [39] performed a molecular dynamics study on the thermal conductivity of modulated SiC nanowires at a mean domain temperature of 300K. When they extrapolated their results for the infinitely long nanowire system, the thermal conductivity of the periodically modulated

nanowire was reduced by about 6% when compared with a straight SiC nanowire of diameter equal to the minimum diameter of the modulated nanowire (D≈2.23 nm). The reduction in thermal conductivity was about 21% versus a nanowire equal to the largest diameter in the modulated system (D≈3.35 nm).

The results of the previous molecular dynamics studies are consistent in that they all indicated that nanostructure boundary geometry can significantly impede phonon transport relative to a smooth and straight nanostructure. In addition, the MD based studies are advantageous over the particle based approach because they directly account for specific nanoscale geometry and wave interference effects. However, phonon behavior is only observed as the aggregate result of all possible modes and therefore information about how a specific phonon mode interacts with a geometric feature is not obtained. Such information could be useful for designing nanostructures for targeted thermal performance. Furthermore, since MD is a classical method, it will only yield accurate results for high temperatures when all phonon modes are occupied. This is because quantization of vibrational energy leads to high occupation of lower frequency phonon modes when the system temperature is low. Information about thermal behavior at low temperatures, where geometry induced scattering is expected to dominate phonon-phonon scattering, is not reliably obtained from an MD simulation.

1.4 Landauer approach to thermal transport

An alternative to using MD to aid in the understanding and simulation of thermal transport in nanoscale systems with irregular geometry is using the Landauer approach for energy carriers [40]. In this approach, thermal transport through a nanostructure geometric feature is analyzed by decomposing the nanoscale system into 3 parts: left and right nanostructure leads and an irregular geometric feature (Figure 1.1). The left and right leads are considered to be thermal reservoirs that continuously emit phonons toward the geometric feature. The total rate at which thermal energy is emitted from the left nanostructure lead can be expressed as a summation over all of the phonon modes in the left lead that are traveling in the positive *x* direction. Similarly, the total rate at which thermal energy is emitted from the right nanostructure lead can be expressed as a summation over all of the phonon modes in the right lead that are traveling in the negative *x* direction. The fraction of energy in a given normal mode that is transmitted across the geometric feature is the modal phonon transmission coefficient, α_{mode}. Thus, if the group velocity of a given mode is v_{mode} and each lead is of arbitrary length, *L*, the net heat flow across the geometric feature can be expressed as:

$$q_{net} = \sum_{\text{mode},+} \frac{\left|v_{\text{mode}}\right| \varepsilon_{\text{mode},+} \alpha_{\text{mode}}}{L} - \sum_{\text{mode},-} \frac{\left|v_{\text{mode}}\right| \varepsilon_{\text{mode},-} \alpha_{\text{mode}}}{L} \tag{4}$$

Here, $\varepsilon_{\text{mode},+}$ is the total energy in a given normal mode of the left nanostructure lead that is traveling in the positive x direction and $\varepsilon_{\text{mode},-}$ is the total energy in a given normal

mode of the right nanostructure lead that is traveling in the negative x direction. The summation over all of the normal modes can be expanded by indexing each normal mode by its wavenumber, *k*, and mode type, ν, so that the net heat flow across the geometry is given by:

$$q_{net} = \sum_{\nu}\sum_{k,+} \frac{\left|v_{k,\nu}\right| \varepsilon_{k,\nu} \alpha_{k,\nu}}{L} - \sum_{\nu}\sum_{k,-} \frac{\left|v_{k,\nu}\right| \varepsilon_{k,\nu} \alpha_{k,\nu}}{L} \tag{5}$$

Here, the summation over wavenumbers is restricted so that only positive traveling modes are included for modes in the left nanostructure lead and only negative traveling modes are included for modes in the right nanostructure lead. The total energy in a given mode is given by:

$$\varepsilon_{\text{mode},+/-} = \left(N_{\text{mode},+/-} + \frac{1}{2} \right) \hbar\omega \tag{6}$$

Where $N_{\text{mode},+/-}$ is the number of positive/negative traveling phonons of the given mode, $\hbar$ is Planck's constant divided by 2π and ω is the phonon's angular frequency. Since the density of states of a 1-D system with propagating phonons is $\frac{\partial n}{\partial k} = \frac{2\pi}{L}$ the summation over wavenumber can be converted to an integral over wavenumber so that the net heat flow can be expressed as:

$$q_{net} = \sum_{\nu} \int \frac{1}{2\pi} \hbar\omega_{k,\nu} \alpha_{k,\nu} \left(N_{k,\nu,+} - N_{k,\nu,-} \right) \left| v_{k,\nu} \right| dk \tag{7}$$

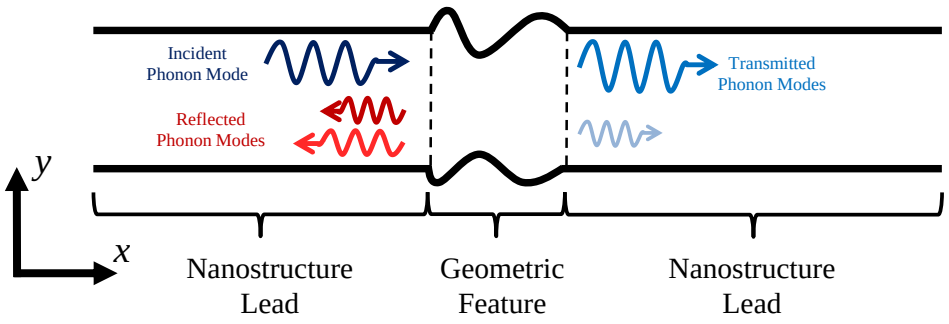

Figure 1.1: Illustration of nanostructure phonon-geometry scattering domain. A single incident phonon mode is incident upon the irregular geometric feature from the left side nanostructure lead. Energy is scattered into reflected phonon modes and transmitted phonon modes. Each nanostructure lead is considered to be perfectly smooth and straight and extends semi-infinitely along the length of the nanostructure.

In general, the number of phonons of each mode at either side of the irregular geometry is a complicated non-equilibrium quantity that will depend on the details of the geometry, anharmonic processes that occur throughout nanostructure, and the system temperature. It is commonly assumed that the system is in quasi-equilibrium so that the phonon distributions on either side of the interface can be approximated by equilibrium distributions corresponding to temperatures of the left and right nanostructure leads, T_L and T_R. Under this assumption, the number of phonons on either side is given by the Bose-Einstein distribution, f_ω^{BE}, which depends only on the lead temperatures and the phonon frequencies. This results in an expression for the net heat flow given by:

$$q_{net} = \sum_\nu \int \frac{1}{2\pi} \hbar \omega_{k,\nu} \alpha_{k,\nu} \left(f_\omega^{BE}(T_L) - f_\omega^{BE}(T_R) \right) \left| v_{k,\nu} \right| dk \tag{8}$$

In the limit of a small temperature difference across the irregular geometry, the thermal conductance, σ, across the irregular geometry can be calculated from:

$$\sigma = \frac{1}{2\pi}\sum_{\nu}\int \hbar\omega_{k,\nu}\alpha_{k,\nu}\frac{\partial f_{\omega}^{BE}(T)}{\partial T}\left|v_{k,\nu}\right|dk \tag{9}$$

Equation (9) provides a "bottom-up" approach by which one can relate the behavior of a particular phonon mode to the overall thermal performance of a nanostructure. Therefore, a critical step toward both understanding the physical processes that govern thermal transport in geometrically irregular nanostructures as well as in designing nanostructures for targeted thermal performance, such as in minimizing phonon transport for thermoelectric applications, is to determine the quantities necessary to calculate the thermal conductance.

1.5 Project Scope

This project's goal is to develop and implement computational and analytical models to analyze and predict how individual phonon modes are affected by irregular nanostructure geometry, use the models to compare to previous approaches assigned to the same task, and to investigate how nanostructure geometry affects overall thermal transport. These tasks are largely done within the context of the Landauer approach to thermal transport across an irregular geometry described in Section 1.4. Chapter 2 of this dissertation describes how the phonon spectra, which includes the phonon frequencies and group velocities, of the left and right nanostructure leads can be determined using an atomistic lattice-dynamics model. The model's correct implementation is verified through comparison with alternative computational approaches based on molecular

dynamics simulation and continuum elastic wave theory. Chapter 3 discusses a variety of approaches by which the modal phonon transmission coefficient can be calculated. Chapter 3 also describes and verifies the implementation of an atomistic lattice-dynamics based computational methodology known as the scattering boundary method. Chapter 4 uses the atomistic computational model developed in Chapters 2 and 3 to assess the accuracy and appropriate regimes of applicability of continuum theoretical approaches that have commonly been used to calculate phonon transmission in nanoscale systems. Chapters 5 and 6 are concerned with developing and using models for the goal of tuning thermal transport in nanowire systems with irregular geometries. Chapter 5 describes a simple model for phonon transmission that is based on long wavelength beam theory and is applicable to the four lowest frequency phonon branches that dominate thermal transport at low temperatures. Informed by the results obtained in Chapter 5, Chapter 6 uses the more comprehensive atomistic computational model developed in Chapters 2 and 3 to investigate aggregate phonon transport in nanowire systems with sections of modulated diameter. Chapter 7 summarizes the most important contributions that were made in the creation of this dissertation and suggests a few topics for future research.

Portions of the work contained in this dissertation were previously published in the ASME Journal of Heat Transfer, Proceedings of ASME 2012 3rd Micro/Nanoscale Heat & Mass Transfer International Conference, and Proceedings of the ASME/JSME 2011 8th Thermal Engineering Joint Conference.

2 Determination of Phonon Spectra and Mode Shapes

2.1 Introduction

In order to evaluate the Landauer heat flow and estimate the thermal conductance across a nanostructure geometric feature, one must determine the phonon spectrum associated with the nanostructure leads. This primarily involves being able to calculate the relationship between the phonon wavenumbers and frequencies associated with each phonon normal mode as well as the complex atomic displacement vectors associated with each mode. There are two primary approaches by which this can be done: continuum based models and atomistic models.

2.1.1 *Continuum Acoustic Analogy for Phonon Spectra*

Continuum methods rely on the assumption that phonons can be treated analogously to acoustic/elastic waves propagating through continuous, linearly elastic media. This is known as the continuum acoustic analogy (CAA). This approach involves finding solutions to elastic wave equations subject to chosen boundary conditions and appropriate for a given geometry. Since this approach is rooted in a field that has been established for well over one hundred years many different geometries and boundary conditions have been considered. Elementary isotropic elastic wave theory can be used to obtain analytical solutions for elastic wave propagation in plate waveguides and cylindrical beams [95]. These solutions are the archetype for guided elastic wave theory. Though they are elegantly formulated, their implementation is not without difficultly since they

usually require the numerical solution of transcendental equations. Further, since they are valid for isotropic materials, their usefulness toward the analysis of nanostructures is limited since the most common nanoscale materials such as silicon have anisotropic elastic properties. More complicated theoretical frameworks are available for the analysis of anisotropic systems and more complicated shapes [41], but require considerable computational effort. Additionally, CAA methods cannot include nanoscale effects such as phonon dispersion associated with discrete particles, irregular lattice strain, or atomistic granularity which is a type of roughness inherent to discrete systems. Another drawback of CAA methods is that they cannot model optical phonons. Optical phonons are associated with high frequency atomic motions when the dominant direction of movement of one atom is opposite that of its neighbors. This may not be a significant drawback because the contribution of optical modes to thermal transport is generally small due to slower group velocity, as compared to lower frequency acoustic modes, and relatively low occupation of optical modes at low and mid-range temperatures. However, recent computational studies of phonon transport in silicon thin films [42][43] have indicated that the role of optical phonons increases with decreasing film width. Therefore, neglecting optical phonons entirely as CAA models do may not always be appropriate. Overall, the CAA approach is likely faithful to the true physics of a nanostructure for low frequency, long-wavelength phonons. As such, it provides an important starting point for the analysis of phonon dynamics in nanostructures.

2.1.2 *Atomistic Models for Phonon Spectra*

Alternatively, phonon spectra may also be calculated using atomistic models. The atomistic approach treats each atom as a point particle with discrete mass. Atomistic studies of phonon dynamics commonly model interatomic interactions through the use of an empirical potential function. Potential functions are obtained through the consideration of general physical principles which determine the functional form and by fitting the function's parameters to experimental results. Potential functions vary in complexity and are tailored to model specific types of materials, but are always empirical in nature. Alternatively, interatomic interactions can be modeled through more accurate, but substantially more computationally demanding, ab initio quantum chemistry methods which involve numerical solution of the Schrödinger equation. In contrast to the CAA, atomistic methods directly account for nanoscale effects such as atomic discreteness and lattice strain. Furthermore, atomistic methods are applicable to the study of optical modes.

For these reasons, an atomistic approach for analyzing and calculating phonon spectra serves as the basis by which phonon transport is modeled throughout this dissertation. The remainder of this chapter describes the chosen atomistic approach, harmonic lattice dynamics, as applied to two geometric systems: silicon nanowires and silicon plates. In addition to describing the method, the method is verified through comparison with an alternative atomistic approach built around molecular dynamics simulation for the specific case of a silicon plate bounded by rigid walls. The lattice

dynamics calculations are further verified through comparison with continuum elastic wave theory for the case of a silicon plate with a free boundary condition. The comparison with continuum theory demonstrates that atomistic effects can cause deviation between an atomistic and a continuum approach and that continuum approaches to modeling phonon dispersion relations are only appropriate for some regimes.

2.2 Harmonic Lattice Dynamics

2.2.1 *Geometric Decomposition into Supercells*

Harmonic lattice dynamics (LD) analysis of phonon spectra is performed by decomposing the system of interest into unit cells such that periodically arraying the unit cell results in the entire structure. LD has typically and extensively been used to characterize the phonon spectra of bulk materials, i.e. systems that are considered to extend infinitely in all directions. In these systems phonons are able to propagate in all directions and most monatomic systems can be described by a unit cell consisting of one or only a few atoms. For instance, bulk silicon can be described by the two atom unit cell characteristic of the diamond lattice. In this work, the interest is on confined phonon propagation in nanostructures such that the bulk treatment with very simple and small unit cells is not appropriate. Instead, the nanostructures of interest are decomposed into supercells whereby each supercell spans the entire confined direction and contains many atoms. Supercells are arrayed periodically and infinitely along the non-confined directions to create a nanostructure that is finite in one or two directions but extends

infinitely in the other directions. This dissertation is specifically focused on two nanostructure systems: silicon nanowires and silicon plates. These nanostructures and their decomposition into supercells are shown in Figure 2.1.

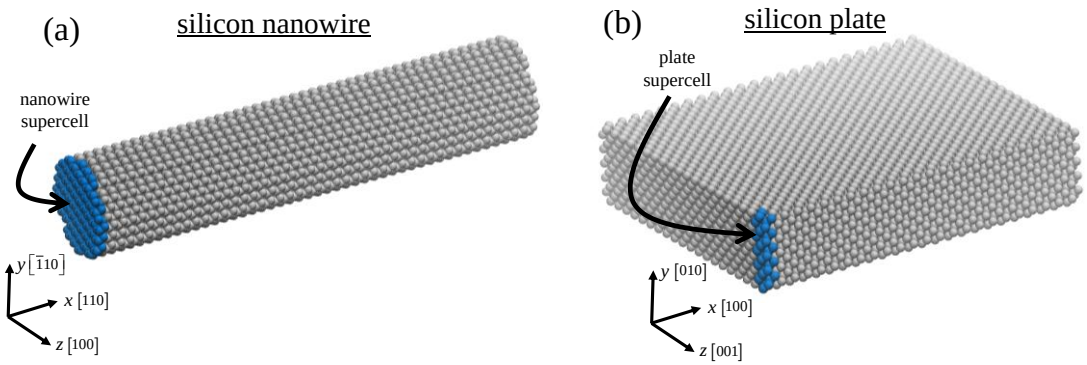

Figure 2.1(a): decompostion of silicon nanowire into supercells; (b): decomposition of silicon plate into supercells.

For the systems studied in this work nanowires are always oriented so that the nanowire extends along the [110] crystal axis and the supercell lattice parameter, $a_{sc} = \frac{1}{\sqrt{2}} a$, where a=0.543 nm is the conventional lattice parameter. The supercell lattice parameter is the distance along the x-direction between equivalent atoms in neighboring supercells. For the plate geometries studied in this dissertation the x-axis of the plate is always aligned with the [100] crystal axis so that $a_{sc} = a$.

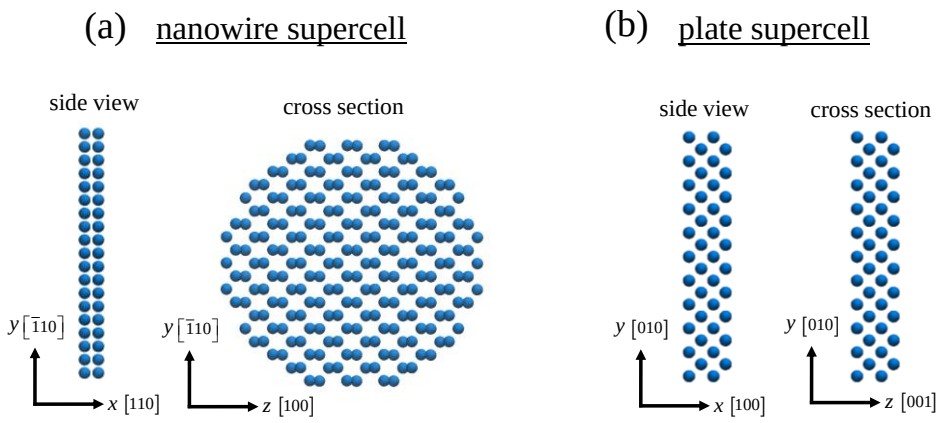

Figure 2.2(a): side view and cross section of nanowire supercell; (b) side view and cross section of plate supercell.

2.2.2 *Theory*

In a nanowire system phonons only propagate along the axis of the nanowire (x-direction). In a plate system, phonons propagate in any direction in the x-z plane, but not in the y-direction. However, for purposes of this dissertation, only phonon propagation along the x-direction is considered. Thus, for both the plate and the nanowire geometries, only one component of wavevector, **k**, is considered. This component, which is also

known as the wavenumber, is denoted *k*, and the lattice dynamics analysis of both the nanowire and the plate geometric are developed in tandem. Instead of referring to each geometry specifically, the term nanostructure supercell is used to collectively refer to either the nanowire supercell or the plate supercell. The only functional difference between the two geometry types are the differing construction of supercells and the fact that periodic boundary conditions are employed in the z-direction for the evaluation of interatomic interactions in the plate geometry.

In harmonic lattice dynamics theory the displacement from equilibrium of any atom in the nanostructure supercell, indexed, *jl*, is expressed as a summation over all normal modes of nanostructure vibration:

$$\mathbf{u}(jl,t) = \sum_{k,\nu} A_{k,\nu} \mathbf{U}(j,k,\nu) \exp\left(i\left(kx(jl) - \omega t\right)\right) \tag{10}$$

In this analysis the notation of Dove [44] is followed such that *j* is the index of an atom in a reference supercell and *l* is the index of each supercell. ω is the phonon angular frequency, *x* is the equilibrium *x*-coordinate of the atom, and ν denotes a mode type. Note that in the plotting of results, the ordinary frequency, f is also used $\left(\omega = 2\pi f\right)$. However, most of the mathematical analysis in this dissertation uses ω which is simply referred to as the frequency. Each phonon mode is uniquely identified by its wavenumber *k* and its mode type *v*. Note that the terms mode type and dispersion branch are used interchangeably in this dissertation. The displacement of any atom *j* in any supercell *l* for a given *k* and *v* is found by multiplying $\mathbf{U}(j,k,\nu)$ by the mode amplitude,

$A_{k,\nu}$, and an exponential phase factor. Using standard methods of lattice dynamics [44], whereby Eq. (10) is substituted into Newton's second law, the equation of motion for an atom, *jl*, can be written as

$$m\ddot{\mathbf{u}}(jl,t) = -\sum_{j'l'} \Phi\begin{pmatrix} jj' \\ ll' \end{pmatrix} \cdot \mathbf{u}(j'l',t) \tag{11}$$

Here m is the mass of the atom and Φ is the force constant matrix. The force constant matrix is a $3N_{sc}$ x $3N_{sc}$ matrix (N_{sc} is the number of atoms in a nanostructure supercell) comprised of N_{sc} 3 x 3 submatrices with elements:

$$\Phi_{\alpha\beta}(jl, j'l') = \frac{\partial^2 W}{\partial u_\alpha(jl)\partial u_\beta(j'l')} \tag{12}$$

α and β denote the Cartesian vector components x, y, and z and W is the total lattice potential energy. Using the column vector

$$\mathbf{e}_{k,\nu} = m^{1/2}\left[U_x(1,k,\nu) \quad U_y(1,k,\nu) \quad U_z(1,k,\nu) \quad U_x(2,k,\nu) \quad \ldots \quad U_z(N_{sc},k,\nu)\right]^T \tag{13}$$

and substituting Eq. (10) into Eq. (11) results in the following eigenvalue problem:

$$\omega^2(k,\upsilon)\mathbf{e}(k,\upsilon) = \mathbf{D}(k)\cdot\mathbf{e}(k,\upsilon) \tag{14}$$

With the dynamical matrix, **D** defined by:

$$\mathbf{D}(jj',\mathbf{k}) = \frac{1}{m}\sum_{l'} \mathbf{\Phi}(j0, j'l')\exp\left(ik\left(x(j'l') - x(j0)\right)\right) \tag{15}$$

Here l=0 denotes the index of the reference supercell and the summation over l' spans all supercells in the system including the reference supercell. For practical implementation,

only supercells containing atoms that have non-zero force interactions with atoms in the reference supercell need to be included in the summation. The phonon dispersion relation which is the relationship between k and ω can be found by computing the eigenvalues of the dynamical matrix **D** as the wavenumber is changed. Each wavenumber and mode type is also associated with the eigenvector, **e**. This vector is denoted the mode shape vector and contains the complex polarization vectors corresponding to each atom within the supercell. The mode shape vector characterizes the spatial variation of atomic motion within a supercell and is analogous to mode shapes used in the analysis of elastic waves in continuum systems except that it is defined for each atom within a supercell as opposed to being a continuous function of nanostructure lateral position**.**

2.2.3 *Stillinger-Weber Potential Function*

In order to evaluate the lattice potential energy, W, an empirical interatomic potential is required. Numerous empirical interatomic potential functions are available for modeling interatomic interactions in silicon. These include the Tersoff potential [45], EDIP [46], MEAM [47], and the Stillinger-Weber (SW) potential [48]. These potential functions have been thoroughly discussed and compared elsewhere [49]. No single potential function gives a perfect match for all relevant thermo-mechanical properties and they vary in complexity and computational efficiency. Because of its widespread use, relative computational efficiency, and ability to produce reasonable agreement with

experimental values for silicon elastic constants, phonon frequencies, and thermal conductivities, the Stillinger-Weber potential function parameterized for silicon was chosen for this dissertation. The total system potential energy when approximated using Stillinger-Weber potential includes pair interactions between two atoms, indexed *i* and *j* (denoted the two-body term, $v_2(i,j)$), potential energy associated with the bond triangle formed by 3 atoms indexed, *i*, *j*, and *k* (denoted the three-body term, $v_3(i,j,k)$) so that the system energy can be evaluated as a sum over all interactions via:

$$\Phi = \sum_i \sum_{j>i} v_2(i,j) + \sum_i \sum_j \sum_{k>j} v_3(i,j,k) \tag{16}$$

The two body interactions are modeled using:

$$v_2(i,j) = \left\{ \varepsilon_{SW} A \left(\frac{B}{\left(\frac{r_j^i}{\sigma_{SW}} \right)^4} - \frac{1}{\frac{r_j^i}{\sigma_{SW}}} \right) \exp\left[\frac{1}{\frac{r_j^i}{\sigma_{SW}} - c} \right] \right. \tag{17}$$

and the three-body interactions are modeled using:

$$v_3(i,j,k) = \varepsilon\lambda \exp\left[\frac{\gamma}{\frac{r_j^i}{\sigma_{SW}} - c} + \frac{\gamma}{\frac{r_k^i}{\sigma_{SW}} - c} \right] \left(\cos\left(\theta_{jik}\right) + \frac{1}{3} \right)^2 \tag{18}$$

Here, r_j^i is the distance between two atoms *i* and *j*, and θ_{jik} is the angle between atoms *j*, *i*, and *k* with the atom *i* at the vertex. For both two-body and three-body interactions, the

interaction energy is zero if either $\frac{r_j^i}{\sigma_{SW}}$ or $\frac{r_k^i}{\sigma_{SW}}$ is greater than c (denoted the cutoff radius). The values for the other parameters are as follows: $\varepsilon = 2.14\ \text{eV}$, $\sigma = 0.20950\ \text{nm}$, $\lambda = 21$, $B = 0.6022245584$, $A = 7.049556277$, $c = 1.8$, and $\gamma = 1.2$.

2.3 Verification of Harmonic Lattice Dynamics

To verify the computational implementation of the harmonic lattice dynamics technique described in Section 2.2, the results from the lattice dynamics calculation are compared with an alternative approaches to calculating phonon spectra. First, the lattice dynamics approach is compared with an alternative atomistic method based on molecular dynamics simulation. Second, the lattice dynamics method is compared with an approach based on continuum elastic wave theory.

2.3.1 *Comparison with Molecular Dynamics*

An alternative atomistic method by which phonon spectra can be calculated is based on molecular dynamics (MD) simulation [27]. The MD approach models a nanostructure as a collection of classically behaving point particles. Similar to lattice dynamics, empirical potential functions are used to model interatomic forces. However, instead of directly decomposing atomic motions into summations over harmonic normal modes as is done in harmonic lattice dynamics, MD simulation directly computes and tracks particle trajectories by integrating classical equations of motion using explicit numerical methods.

In order to determine phonon spectra from an MD simulation, an entire nanostructure domain is constructed with particle locations initialized on their equilibrium lattice sites with initial particle velocities distributed according to the Maxwell Boltzmann distribution corresponding to a desired simulation temperature as to activate incoherent particle vibrations with arbitrary spatial variation. The system is equilibrated for several thousand time steps so that particle motion is no longer affected by the randomness of the initial velocity distribution and is instead governed by the normal vibrational modes of the structure.

After equilibration, the system progresses for an additional period over which particle velocities are recorded at regular intervals. After the full time history of particle velocities has been recorded, the spectral energy density method [50] is used to calculate the structure's dispersion relation. The spectral energy density is found by projecting the velocities of the particles in the structure onto a generic form of a traveling wave characterized by a wavenumber and angular frequency. The spectral energy density of a mode corresponding to a unique wavenumber and frequency is calculated using:

$$\Psi(k,\omega) = C\sum_{\alpha}\left|\int \sum_{p}^{N_a} \dot{u}_{p,\alpha}(t)\exp\left[ikx_0(p) - i\omega t\right]dt\right|^2 \tag{19}$$

Here, $\dot{u}_{p,\alpha}(t)$ is the p^{th} particle's velocity component in the α direction. N_a is the total number of atoms in the system and $x_0(p)$ is the equilibrium x-coordinate of the particle p. The quantity *C* is a normalization constant that is not important for the calculation

since only the location of spectral energy density peaks is required, not the magnitude. The peaks in the spectral energy density calculated at each wave number constitute each wavenumber's possible frequencies of vibration. The amplitude of the peaks can then be plotted as a function of frequency and wavenumber and connected to form each branch of the nanostructure's dispersion relation.

Unlike in harmonic lattice dynamics, it is not straight forward to use molecular dynamics to calculate the mode shapes associated with each normal mode. Because of this, a new computational method was developed to do this that was based upon arbitrarily exciting a small region in the MD simulated domain at a desired frequency. In this way all possible phonon modes at that frequency are excited. The atomic displacements at different snap shots in time are then analyzed using Fourier analysis to extract the mode shape associated with a specific wavenumber. It was found that this method was computationally expensive and prone to numerical error and was therefore discarded in favor of harmonic lattice dynamics. Because of this, the details of the method are not presented in this dissertation, but can be found in reference [51]. As an alternative to the spectral energy density approach, it should be noted that another method has recently been developed [52] in which the dynamical matrix can be determined through analysis and post-processing of MD particle velocity data.

To verify that the lattice dynamics calculations are implemented correctly, a comparison with the MD calculated spectral energy density was performed for a silicon plate bounded by rigid walls. The rigid wall boundary condition was employed to prevent

structural relaxation in the MD system. Structural relaxation can complicate the MD analysis since obtaining relaxed configurations requires additional computational expense. Since this comparison was done only to confirm the proper computational implementation of the lattice dynamics calculation, the added complication and computational expense associated with structural relaxation was avoided by using the rigid boundary condition. In order to include the effect of the rigid boundary condition in the lattice dynamics calculation, four layers of atoms were added on both sides of the plate for the determination of the harmonic stiffness matrices. Though these atoms exert forces on atoms in the plate supercell, they are not included in the supercell itself since the rigid condition prohibits their motion.

The LD and MD calculated dispersion relations are compared in Figure 2.3 by overlaying the LD calculated dispersion relation on top of the MD calculated spectral energy density. The spectral energy density is represented by mapping its intensity to a color as indicated in the color bar of Figure 2.3. The peaks in the spectral energy density indicate the existence of a normal mode and appear in darker red. Some of the peaks are difficult to discern since the MD simulation occurs at finite temperature (T=1K for results presented herein) which enables energy to change modes and causes noise in the frequency spectrum surrounding each peak. The resolution of the MD produced dispersion relations can be improved by increasing simulation time and through filtration of the image produced by the spectral energy density. Since the MD-spectral energy density technique was found to be, in general, inferior to harmonic lattice dynamics, a

thorough investigation of how to improve the clarity of the MD produced dispersion relations was not performed. However, the peaks in the spectral energy density that are clearly discernible are well aligned with the dispersion curves calculated with lattice dynamics. This confirms that the LD calculations are implemented correctly.

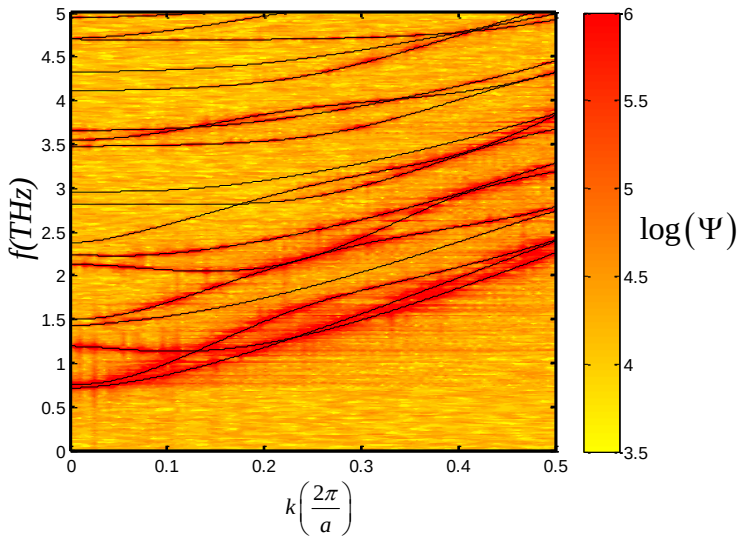

Figure 2.3: Dispersion relation comparison for rigid wall plate waveguide. Width of plate is 3.4 nm. The MD calculated dispersion relation is presented by mapping the magnitude of the spectral energy density to the colors indicated in the color bar. Darker red corresponds to peaks in the spectral energy density. The peaks that are clearly discernible are well aligned with the dispersion relation curves calculated using lattice dynamics.

2.3.2 *Comparison with Continuum Theory*

Phonon dispersion relations are also commonly calculated using methods based on continuum elastic wave theory. This treatment is appropriate for long-wavelength/low-frequency phonons in nanostructures with characteristic widths much greater than the interatomic spacing. To further verify the implementation of the lattice dynamics calculation, a comparison with continuum theory was also made. In contrast

with the comparison that was done with molecular dynamics, where the rigid boundary condition was largely chosen out of computational convenience, a free boundary condition was used in the comparison with continuum theory.

The continuum dispersion relations were calculated using the superposition of partial waves (SPW) method presented by Solie and Auld [53]. In their work, the problem of the elastic plate with stress-free boundary conditions was solved for elastic wave propagation in cubic crystal systems where the axes of the plate are aligned with the material's crystal axes. In the method, the Christoffel matrix equation is used to find the generic forms of the partial traveling elastic waves that are possible for the given crystal structure and orientation. For elastic wave propagation aligned with direction of high crystal symmetry, the theoretical displacement field separates into two distinct mode families: shear horizontal modes (SH modes), and Lamb modes. SH modes consist only of uncoupled shear partial waves that are polarized perpendicular to the plane established by the plate thickness and the direction of propagation. Because of their uncoupled nature, the SH mode dispersion relation can be calculated from a simple analytical expression found in most elementary elastic wave theory textbooks [54]. Lamb modes consist of coupled P (quasi-longitudinal) and SV (quasi-shear vertical) partial wave components and have non-zero displacements in the plane established by the plate thickness and the direction of propagation. Because of their more complicated nature, the dispersion relations associated with the Lamb modes must be calculated numerically.

The results of the comparison are shown in Figure 2.4. The elastic stiffness constants used in the calculations, c_{11}=151.4GPa, c_{12}=76.4GPa, and c_{44}=56.4GPa, are taken from a computational study of crystalline silicon approximated by the Stillinger-Weber potential [55]. In the comparison of methods, results for three different sizes are presented. In all three cases the continuum and atomistic curves are virtually indistinguishable from one another for the zeroth order modes (modes that propagate down to zero frequency) at low wavenumbers. There are deviations between the models at higher wavenumbers and for higher order modes. Higher order modes are modes with non-zero cutoff frequencies. The cutoff frequency is the minimum frequency that a mode can propagate. In general, the comparison with continuum becomes more favorable with increasing plate width, but there is always a gradual worsening of model agreement at higher frequencies and wavenumbers. While an exhaustive comparison was not performed, these results suggest that a continuum approach to modeling phonon spectra is appropriate for silicon nanostructures with lateral width greater than 10 nm, wavenumbers less than 1 (1/nm) (corresponds to wavelengths greater than about 6 nm), and phonon frequencies less than 2 THz. Depending on the level of accuracy desired and the size of nanostructure considered, these limits of continuum model applicability may perhaps be extended. However, because of the discrete nature of the atomistic system, the continuum model should be expected to fail for higher wavenumber, higher frequency phonons. More discussion on the limits of continuum models on modeling phonon transport in nanoscale systems is given in Chapter 4. Though a thorough conclusion has

not been drawn regarding the general applicability of continuum models to modeling phonon spectra, this comparison further verifies the computational implementation of the lattice dynamics calculation and demonstrates that atomistic dispersion relations match continuum dispersion relations in long wavelength, low frequency limit.

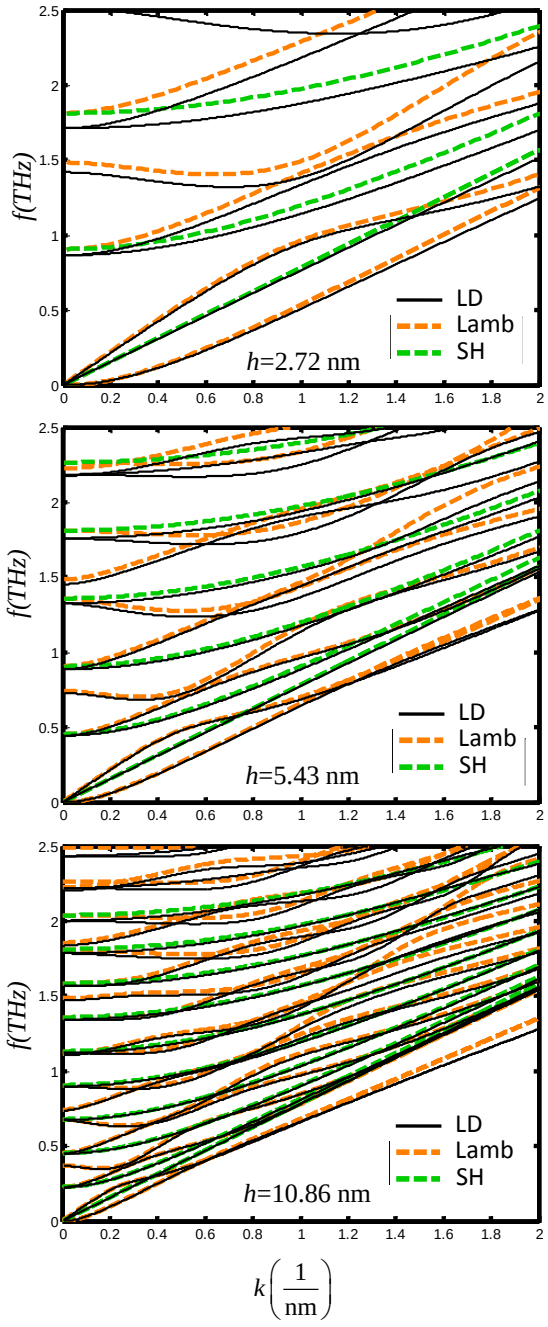

Figure 2.4: Dispersion relation comparison for plate waveguide with free boundaries. Results of continuum calculation (using the method of Solie and Auld [53]) are given in dashed colored lines. Atomistic results from harmonic lattice dynamics are given in solid black lines. *h* is the width of the plate.

2.4 Summary

This chapter described the mathematical background and computational implementation of a harmonic lattice dynamics approach to calculating phonon spectra of a nanostructure. The harmonic lattice dynamics formulation was described for both nanowire and nanoplate geometries. The implementation of the lattice dynamics calculation was verified via comparison with a plot of the phonon spectral energy density obtained from a molecular dynamics simulation of a silicon plate with rigid walls. The lattice dynamics calculation was further verified via comparison with the superposition of partial waves method based continuum elastic wave theory for the case of a silicon plate with free boundaries. The comparison with continuum theory, while limited in scope, suggested conservative regime boundaries for the applicability of continuum elastic wave theory to modeling phonon spectra in nanoscale systems.

3 Determination of Modal Phonon Transmission

3.1 Chapter Overview

The next task in modeling geometry dependent phonon transport in nanostructures is developing a suitable computational tool that can be used to calculate modal phonon transmission coefficients. This chapter discusses several computational approaches that can be used to calculate phonon transmission coefficients in geometrically irregular nanostructures. Section 3.2 surveys two previously used approaches and highlights some of their disadvantages. An alternative lattice dynamics based computational technique called the scattering boundary method improves on some of the shortcomings of the previous approaches and was selected as the primary computational tool to be used for the completion of this dissertation. The method was adapted from previous studies on phonon transmission across bulk material interfaces and is described in detail in Section 3.3. A comparable computational technique called the molecular dynamics wavepacket method was also considered as a means to calculate modal phonon transmission coefficients. This method is described in Section 3.4 and is used to verify the computational implementation of the scattering boundary method calculations. The verification of the scattering boundary calculations is done for the simple case of shear-horizontal phonon transmission through a rigid-walled silicon plate with T-stub. Section 3.5 presents the results of this comparison and demonstrates that the scattering boundary calculations have been implemented correctly.

3.2 Survey of Previous Approaches

3.2.1 *Continuum Acoustics Approach*

To date, modal phonon transmission coefficients are most popularly calculated through the use of continuum acoustics analogy. Researchers have used continuum acoustics methods to calculate phonon transmission in a wide variety of geometries [56-70]. Despite their widespread use, continuum acoustics methods suffer from a number of shortcomings. First, as was the case with CAA methods used to calculate phonon spectra, CAA transmission methods cannot include nanoscale effects associated with atomic discreteness nor are they capable of calculating phonon transmission of optical modes. Additionally, most works utilizing CAA methods have typically employed dispersion and mode shape models that are greatly simplified when compared to systems of real practical interest such as semiconductor nanowires. For instance, the models used are generally two-dimensional and employ scalar models for wave transport. In doing so, the problem is formulated in a way that is tractable using simple eigenmode expansion methods such as the scattering matrix method [72]. Though this approach is rigorous and exact for the case of shear horizontal (SH) wave propagation in infinite plates, it only approximates the complex dynamics of most elastic wave modes (e.g. Lamb modes in plates or general wire modes) since, for the example of wave propagation in an infinite plate, quasi-shear vertical (SV) and quasi-longitudinal (P) partial wave modes are coupled. Because of this, it is unlikely that the detailed findings of CA studies will

maintain validity when applied to three dimensional nanostructures with more complex and coupled phonon modes. More sophisticated continuum methods including hybrid finite element-eigenmode expansion methods [73] [74] could be used to study phonon transport in nanostructures in a more a rigorous way in that they will allow for mode coupling and three-dimensional geometry. These methods have been motivated by macroscale applications in non-destructive testing and have thus far not been implemented explicitly for the investigation of ballistic phonon transport in nanoscale systems. However, any continuum method is not able to model the atomistic effects such as atomic discreteness nor will they allow for optical modes.

3.2.2 *Atomistic Green's Functions Method:*

An alternative approach for calculating phonon transmission that does accurately model all phonon modes and accounts for atomistic effects is the atomistic Green's functions (AGF) method. The AGF couples the vibrational degrees of freedom of two "lead or contact" regions through a "device" region via the calculation of harmonic matrices for both the contact and device regions. Frequency dependent Green's functions that are formulated in terms of the harmonic matrices are then used to calculate total phonon transmission from one contact to another through the device as a function of incident phonon frequency. The AGF method has been used, for example, to calculate phonon transmission across silicon nanowire-bulk junctions [75], graphene and graphene nanoribbon interfaces [77,78] and silicon-germanium heterostructures [79].

AGF models are formulated so that phonon transmission is output as a function of frequency. AGF models account for all of the vibrational degrees of freedom, but atomic motions are not decomposed into nanostructure normal modes. As a result, phonon transmission dependence on mode type and wavenumber is not directly discerned. While it may be possible to deconstruct frequency dependent phonon transmission into each mode's contribution, this has not been done in the literature surveyed.

3.3 Scattering Boundary Method

The ability to design nanostructures for specific phonon transmission behavior would best be enabled by a model capable of calculating individual mode transmission since only this kind of model will be able to directly discern the dependence of phonon transmission on the properties of a particular mode. Relevant mode properties include the mode's wavelength and its associated made shape vectors. One computational approach capable of doing this is the scattering boundary method. The scattering boundary method (SBM) is an atomistic method that is based on harmonic lattice dynamics and is similar in spirit to the AGF method. Though they are fundamentally equivalent [79,80] the SBM is formulated so that mode dependent transmission is a direct output and that differences in phonon transmission between phonon modes at the same frequency can be easily discerned. Like the AGF method, the SBM approach calculates harmonic stiffness matrices for irregular geometric feature and nanostructure leads

regions, but the motions of the nanostructure lead region atoms are constrained so that they are linear combinations of the nanostructure lead regions' normal modes of vibration.

3.3.1 *Previous Use*

While the SBM is notable for its ability to obtain mode and geometry dependent detail while also accounting for nanoscale effects, it is a relatively new method and has only seen limited implementation in the investigation of nanoscale geometry and thermal properties. The SBM has most popularly been used to predict individual phonon transmission and characterize overall thermal resistance of bulk material interfaces [81-83]. It has also been used to calculate the cross-plane thermal resistance of superlattice layers [82,84]. In terms of its implementation for the study phonon transport in geometrically irregular nanostructures it has thus far only seen very limited use. It was used by Wang and Wang to calculate mode dependent phonon transmission across asymmetric nanotube junctions [85] and a very similar method, not described by the author as the scattering boundary method, but similar in implementation, was used by Khater et al. to study phonon transmission and thermal resistance though a constricted ultra-thin (2 atomic layers) gold thin film [86].

3.3.2 *Geometric Decomposition*

The scattering boundary method analysis of a nanostructure scattering problem is done by decomposing a nanostructure scattering domain into three regions: two

nanostructure leads (left and right) and the nanostructure scattering central region. The scattering central region is analogous to the "device" region in the AGF formulation. See Figure 3.1 for illustration of scattering boundary domain decomposition. The two nanostructure leads are constructed as the semi-infinite periodic arrangement of nanostructure supercells. The nanostructure supercells may be nanowire supercells (Figure 2.2(a)) or plate supercells (Figure 2.2(b)). This dissertation presents calculation results for both geometry types. The illustration presented here is of a constricted nanowire geometry, but the decomposition and computational technique is valid for an arbitrary geometry within the nanostructure scattering central region and the nanostructure leads may be wire or plate geometries.

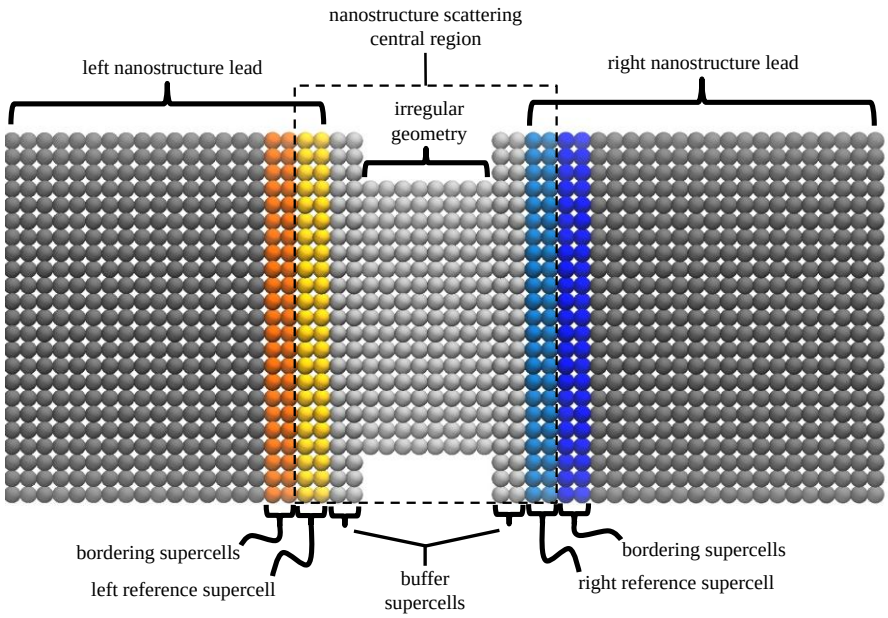

Figure 3.1: Geometric decomposition of atomistic nanostructure scattering system for scattering boundary method calculations.

The nanostructure scattering central region contains any irregular feature that breaks the periodicity of the semi-infinite nanostructure leads, one or more supercells that interact with atoms that comprise the irregular geometric feature (denoted buffer supercells), and one supercell of each nanostructure lead (denoted lead reference supercells). The minimum number of buffer supercells is determined by the longest interaction distance corresponding to the chosen potential. Because of the short-range nature of the Stillinger-Weber potential, only one buffer supercell is required. Additional supercells may be included, but it was found that these do not affect the transmission result. The effect of the semi-infinite nanostructure lead is manifest through consideration of bordering supercells (shown in Figure 3.1). Because of the semi-infinite, periodic nature of the nanostructure leads, only the atoms within the nanostructure scattering central region and the bordering supercells and are explicitly included in the numerical analysis.

3.3.3 *Transmission Calculation*

Phonons incident from the left nanostructure lead, encounter the irregular geometric feature and scatter so that some of the energy is reflected backwards and some is transmitted to the right nanostructure lead. The interatomic interactions in the system are modeled using linearized potential functions so that the scattering process is elastic. As a result, reflected and transmitted phonon frequencies are equal to the incident phonon frequency. Since all motions occur at the same frequency, the time dependence can be

omitted and only the displacement phasor, $\tilde{\mathbf{u}}_{jl}^{L}$, of a given atom in the left nanostructure lead is considered. Note that the notation used in this presentation is the same as that used in Chapter 3. The displacement phasor, $\tilde{\mathbf{u}}_{jl}^{L}$, is expressed as the superposition of the incident phonon mode and the sum of all reflected phonon modes, ν_{re}^{L}, which are normal modes of the left nanostructure lead:

$$\tilde{\mathbf{u}}_{jl}^{L} = \mathbf{U}^{L}\left(j, k_{in}^{L}, \nu_{in}^{L}\right)\exp\left(ik_{in}^{L}x^{L}\left(jl\right)\right) + \sum_{\nu_{re}^{L}}^{N_{re}^{L}} A_{k_{re}^{L},\nu_{re}^{L}}\mathbf{U}^{L}\left(j, k_{re}^{L}, \nu_{re}^{L}\right)\exp\left(ik_{re}^{L}x^{L}\left(jl\right)\right) \quad (20)$$

The incident mode which is identified by its wavenumber, k_{in}^{L}, and mode index, ν_{in}^{L}, has a corresponding polarization vector unique to each atom with the reference nanostructure lead, $\mathbf{U}^{L}$. The amplitude of the incident mode is assumed to be one. Each reflected mode has a corresponding wavenumber, k_{re}^{L}, mode index, ν_{re}^{L}, and unknown amplitude, $A_{k_{re}^{L},\nu_{re}^{L}}$. As described in Chapter 2, j is an atom index corresponding to an atom within the reference supercell and l is a supercell index. For the calculations presented herein, l spans the reference supercell and one bordering supercell. This is because the Stillinger-Weber potential has a short interaction distance. For interatomic potentials with longer range interactions, additional bordering supercells would be required. Reflected modes of the left nanostructure lead either propagate to the left and have negative group velocity and wavenumbers that are purely real or have complex wavenumbers and decay away from the interface between the left nanostructure lead and the scattering central region. The summation over reflected modes includes both propagating modes and evanescent

modes so that the total number of reflected modes is N_{re}^{L} . Similar analysis is performed for the right nanostructure lead so that the displacement phasor, $\tilde{\mathbf{u}}_{jl}^{R}$, of a given atom in the right nanostructure lead is expressed as the sum of all possible transmitted phonon modes, ν_{tr}^{R}, which are normal modes of the right nanostructure lead:

$$\tilde{\mathbf{u}}_{jl}^{R} = \sum_{\nu_{tr}^{R}}^{N_{tr}^{R}} A_{k_{tr}^{R}\nu_{tr}^{R}}^{R} \mathbf{U}^{R}\left(j, k_{tr}^{R}, \nu_{tr}^{R}\right) \exp\left(ik_{tr}^{R} x^{R}\left(jl\right)\right) \tag{21}$$

The possible transmitted phonon modes of the right nanostructure lead are those that either propagate to the right and have positive group velocity and purely real components of wavenumber or have complex wavenumbers and decay away from the interface between the right nanostructure lead and the scattering central region. The total number of transmitted modes is N_{tr}^{R}. Each transmitted mode has a corresponding wavenumber, k_{tr}^{R}, mode index, ν_{tr}^{R}, and unknown amplitude, $A_{k_{tr}^{R},\nu_{tr}^{R}}$.

The displacement phasor of any atom, *p*, within the nanostructure scattering central region must satisfy the harmonic equations of motion defined as a summation over interactions with each atom, *q*, within the entire system:

$$m_p \omega^2 \tilde{\mathbf{u}}_p = \sum_q \mathbf{\Phi}\left(p, q\right) \tilde{\mathbf{u}}_q \tag{22}$$

The sum over *q* includes all atoms within the nanostructure scattering central region, atoms in the reference supercells, and atoms in the bordering supercells.

Equations (20), (21), and (22) are solved simultaneously for the amplitudes of the transmitted and reflected modes, $A^R_{k_{tr},\nu_{tr}}$, and $A_{k^L_{re},\nu^L_{re}}$, respectively, as well as the displacement phasor, $\tilde{\mathbf{u}}_p$, of each atom in nanostructure scattering central region. The amplitudes are used to compute the modal phonon transmission coefficient, $\alpha_{k_{in},\nu_{in}}$, and reflection coefficient, $\eta_{k_{in},\nu_{in}}$, of the incident mode using [82]:

$$\alpha_{k_{in},\nu_{in}} = \sum_{\nu^R_{k_{tr},\nu_{tr}}}^{N^R_{prop}} \left| A^R_{k_{tr},\nu_{tr}} \right|^2 \frac{v^R_{k_{tr},\nu_{tr}}}{v^L_{k_{in},\nu_{in}}} \tag{23}$$

$$\eta_{k_{in},\nu_{in}} = \sum_{k_{re},\nu_{re}}^{N^L_{prop}} \left| A^L_{k_{re},\nu_{re}} \right|^2 \frac{v^L_{k_{re},\nu_{re}}}{v^L_{k_{in},\nu_{in}}} \tag{24}$$

The summations in Eqs. (23) and (24) include only propagating modes. The propagating modes are those with purely real wavenumbers. Modes with non-zero imaginary components of wavenumber are evanescent modes that decay away from the interfaces between the nanostructure leads and the nanostructure scattering central region. Therefore, they do not carry energy and are not required to calculate the modal transmission and reflection coefficients. Their amplitudes are required to properly solve the equations of motion in the scattering central region and must be included in equations (20) and (21). The group velocity, v, corresponding to any mode may either be calculated by numerically differentiating the dispersion curves or from [82]:

$$v_{k,\nu} = \frac{1}{2\omega}\left[\mathbf{e}^*(k,\upsilon) \frac{\partial \mathbf{D}}{\partial k} \mathbf{e}(k,\upsilon) \right] \tag{25}$$

Here, $\mathbf{e}^{*}(k,\upsilon)$ is the complex conjugate of $\mathbf{e}\ (k,\upsilon)$. Comparison of the two calculation approaches for group velocity showed that for most system sizes it is more computationally efficient to calculate the group velocity from equation (25). For each transmission calculation, in order to ensure that energy is conserved and as a simple computational check, it is verified that the total transmission and reflection coefficients add to one.

3.3.4 *Determination of Normal Modes*

In order to solve the aforementioned system, the wavenumbers and complex displacement vectors associated with each mode must be known. In the lattice dynamics formulation described in Chapter 2, a wavenumber is chosen and the frequencies and polarization vectors are calculated by finding the eigenvalues and eigenvectors of the dynamical matrix, **D**. In order to perform the transmission calculation, a frequency is chosen and all of the possible wavenumbers and their corresponding polarization vectors must be calculated. To accomplish this task, the approach of Zhao and Freund [81] was used and an alternative formulation of the eigenvalue problem (equation (14)) is constructed:

$$\omega^2\hat{\mathbf{e}}(k,\upsilon)=\hat{\mathbf{D}}(k)\cdot\hat{\mathbf{e}}(k,\upsilon) \tag{26}$$

Where the alternative dynamical matrix is defined by

$$\hat{\mathbf{D}}(jj',k)=\frac{1}{m}\sum_{l'}\mathbf{\Phi}(j0,j'l')\exp\left(ik\left(x(0l')-x(00)\right)\right) \tag{27}$$

The only difference in Eq. (27) versus Eq. (15) is that the phase factor in Eq. (27) uses the *x*-position of a reference atom, denoted *j*=0, in the given supercell, l', relative to a reference atom in the reference supercell that is unchanged in the summation. This relative position is always either $\pm a_{sc}$ or zero. As noted in [81,82], this reformulation of the eigenvalue problem arises from the short-range nature of the Stillinger-Weber potential enables one to decompose the dynamical matrix into three parts associated with interactions with only the nearest neighboring supercells following:

$$\hat{\mathbf{D}} = \varsigma^{-1}\hat{\mathbf{D}}_{-} + \hat{\mathbf{D}}_{0} + \varsigma\hat{\mathbf{D}}_{+} \tag{28}$$

Here, the phase factor, ς, is defined as

$$\varsigma = \exp\left(ika_{sc}\right) \tag{29}$$

so that $\hat{\mathbf{D}}_{-}$ contains only the elements of $\hat{\mathbf{D}}$ that multiply the phase factor $\exp\left(-ika_{sc}\right)$, $\hat{\mathbf{D}}_{+}$ contains only the elements of $\hat{\mathbf{D}}$ that multiply the phase factor $\exp\left(ika_{sc}\right)$, and $\hat{\mathbf{D}}_{0}$ contains only the elements of $\hat{\mathbf{D}}$ corresponding to interactions within the reference supercell such that the phase factor is one. a_{sc} is the supercell lattice parameter and is defined in Chapter 2. Combining (26) and (28) results in the non-linear eigensystem:

$$\omega^2\hat{\mathbf{e}}\left(k,\upsilon\right) = \left[\varsigma^{-1}\hat{\mathbf{D}}_{-} + \hat{\mathbf{D}}_{0} + \varsigma\hat{\mathbf{D}}_{+}\right]\cdot\hat{\mathbf{e}}\left(k,\upsilon\right) \tag{30}$$

For a chosen phonon frequency, Eq. (30) is used to solve for the eigenvalues ς which, by using Eq. (29), yields all of the wavenumbers at the incident phonon frequency. The

wavenumbers can be used with equation (14) to find the mode shape vector, **e**, associated with each normal mode which are used to obtain the complex polarization vectors, **U**, for each atom in the nanostructure leads for each nanostructure lead normal mode.

In summary, in order to calculate the atomistic modal phonon transmission coefficients, first a desired incident mode is selected and its frequency at a chosen wavenumber is calculated using (14). Next, the wavenumbers of all of the possible excited modes of both the left and right nanostructure leads at the incident mode frequency are calculated by finding the eigenvalues of Eq. (30). Next, all of the mode shape vectors associated with the possible excited modes are calculated using equation (14) evaluated at each possible excited wavenumber. Eqs. (20), (21), and (22) are solved simultaneously for each possible excited mode's amplitude. The amplitudes are then used to calculate the modal transmission coefficients using Eqs. (23) and (24).

3.4 Molecular Dynamics Wavepacket Method

The molecular dynamics wavepacket method (MDWPM) is another atomistic method that can be used to calculate modal phonon transmission coefficients. The method was originally introduced for the study of bulk longitudinal and transverse phonon transmission at semiconductor interfaces [87]. Subsequent to its original application, it was used to study scattering of phonon wavepackets at material interfaces in semiconductor nanowires [87,88] and to study scattering of longitudinal and twisting

phonon modes in defective carbon nanotubes [89]. Similar techniques have been used to study bulk acoustic phonon scattering from isolated nanoparticle inclusions [90] and phonon scattering in nanostructured thin films [91]. The MDWPM approach was initially explored as a primary means of calculating modal phonon transmission coefficients for the purposes of this dissertation. Experience with the method revealed it to be inferior to the scattering boundary method and was abandoned as a primary computational tool. However, the reason it was abandoned was practical (too computationally expensive and unwieldy) rather than scientific since it was found to yield accurate results that agree with other methods. The method is presented here primarily as a means to verify the correct computational implementation of the scattering boundary method, but also to highlight its viability and shortcomings as a computational method.

3.4.1 *Description of Method*

The MDWPM approach operates by simulating a molecular dynamics nanostructure system such as that shown in Figure 3.2. Note that the method is generally applicable to any irregular geometric feature that joins two nearly semi-infinite nanostructure lead regions that can be constructed through the periodic repetition of supercells such as those used to calculate phonon spectra using harmonic lattice dynamics. However, the method is specifically described here for the rigid-walled plate T-stub geometry shown in Figure 3.2 which is the system that is used to verify the

computational implementation of the scattering boundary method. On the left hand side of the domain is a very long region that is denoted the incident region For a given wavenumber and dispersion branch of interest, a phonon wavepacket of narrowly defined frequency and wavenumber is excited in the incident region by initializing the atomic displacements, **u**, and velocities, **v**, according to their normal modes as calculated using the harmonic lattice dynamics techniques described in Chapter 2. The atomic displacements and velocities are initialized as follows:

$$\begin{aligned}\mathbf{u}_{k,\nu}(jl,t=0) &= A_{ex}\mathbf{U}(j,\mathbf{k},\nu)\exp\left(i\left(k_{in}x(jl)\right)\right)\exp\left(-\eta^2\left(x(jl)-x_0\right)^2\right)\\ \mathbf{v}_{k,\nu}(jl,t=0) &= -i\omega(k,\nu)A_{ex}\mathbf{U}(j,\mathbf{k},\nu)\exp\left(i\left(k_{in}x(jl)\right)\right)\exp\left(-\eta^2\left(x(jl)-x_0\right)^2\right)\end{aligned} \quad (31)$$

x_0 is set equal to 1/4 of the total nanostructure length so that the wavepacket is centered in incident region and the parameter η is varied to control the wavepacket width noting that the extent of the wavepacket is approximately proportional to 1/η. For results presented in herein, the wavepacket width is defined such that $L_{wp}=4/\eta$ (see illustration of wavepacket width in Figure 3.4(a)). Accurate determination of phonon transmission requires that thermalization, or distribution of the wavepacket energy across all frequencies, be avoided. For this reason, the molecular dynamics simulations use low energy wavepackets superposed on a zero temperature background. The excitation amplitude, A_{ex}, must be chosen to be low enough to avoid phonon decay associated with anharmonicity of the interatomic potential, but high enough such that the signal strength is significantly greater than background numerical noise. For the results presented

herein, A_{ex}=0.0005σ was used (σ is the Stillinger-Weber length parameter). The length of the nanostructure (x-direction) is variable depending on the width of the wavepacket excited and, in general application, may be aligned with any direction that could be decomposed into periodic supercells. For the verification results presented in section 3.4 it is aligned with the [1 0 0] crystal axis. The thickness of the plate in the z-direction is one conventional unit cell (i.e. one lattice parameter). Larger widths in the z-direction were tested and the changes in results were negligible. Periodic boundary conditions are employed in the z-direction. The T-stub is located in the middle of the domain and the rigid wall boundary condition is enforced by fixing the displacement of the first several outer atomic layers to zero for the duration of the simulation. The simulation is executed according to standard techniques of molecular dynamics [48] using a time step of one femtosecond. The total duration of the simulation is chosen such that the phonon wavepacket has time to propagate across the entire domain and is variable depending on the group velocity of the excited mode and the domain length. The total energy of the system on each side of the T-stub is monitored and the transmission coefficient is calculated from the final distribution of system energy via

$$\alpha_{k_{in},\nu_{in}} = \frac{E_{transmitted}}{E_{incident}} \tag{32}$$

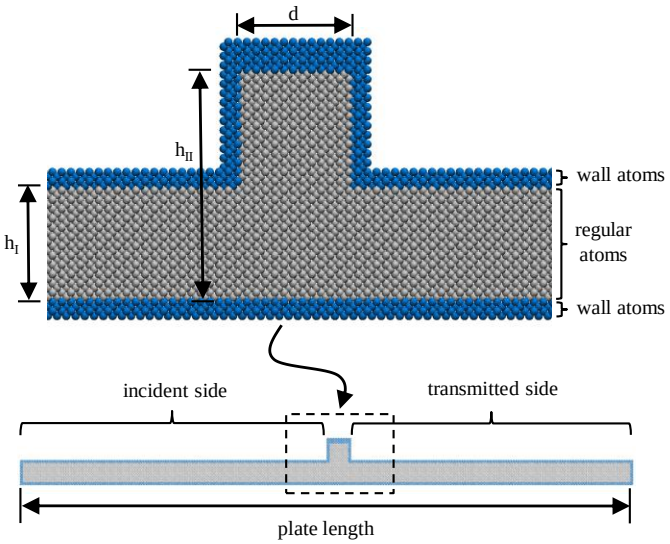

Figure 3.2: Molecular dynamics computational geometry used for MDWPM comparison with SBM.

3.4.2 *Disadvantages of MDWPM*

Experience with the method demonstrated that it can reliably obtain mode dependent transmission results, but it does have significant shortcomings. First, since this method uses wavepackets, it cannot precisely isolate phonon modes comprised of only one wavenumber or frequency. Rather, the wavepacket is comprised of modes spanning a range of wavenumber and frequency that is centered about a desired mode. While longer wavepackets can be used to better isolate the desired mode, this requires the simulation of large domains that can be computationally expensive. In order to ensure accuracy of transmission results, a convergence study of transmission versus wavepacket size should be performed to estimate the minimum wavepacket size required to obtain a desired level of accuracy. Second, since this technique occurs within the framework of an MD simulation it can be susceptible to background noise

associated with signal spreading to unwanted frequencies from anharmonic interactions or due to the relaxation of the base structure to a new lower potential energy equilibrium state. Wavepackets with extremely small amplitude can be used to minimize anharmonic interactions, but these can then be susceptible to other noise problems associated with numerical error. If care is taken to select a proper excitation amplitude this problem can usually be avoided. Rigid wall boundary conditions can be implemented to avoid problems associated with structural relaxation and make the method computationally easier to implement. Though the rigid wall boundary condition has been used by others for computations of thermal transport in silicon [92], it is most valid only for the case of silicon confined by very stiff layers. Such a situation would occur, for example, in silicon-on-diamond electronics. Most cases of real technological interest are better modeled using a free boundary condition. In these cases, relaxed structures can be attained through an MD annealing process or other means, but this requires additional computational burden. In contrast, the scattering boundary method avoids all of these problems and is much more computationally efficient. As such, the MD-wavepacket method is used only as a means to verify the proper implementation of the scattering boundary method.

3.5 Verification of SBM Implementation

The correct implementation of the scattering boundary method transmission calculation was verified via comparison with MDWPM simulations for the T-stub

geometry. Since the purpose of this comparison is only for SBM model verification, the results presented herein are for only one geometry size and for the first shear horizontal mode (SH1). For more discussion on the transmission of shear horizontal modes in rigid wall systems, see reference [92] which also presents MDWPM transmission results for a wider range of systems sizes. Figure 3.3 plots SH1 phonon transmission through the T-stub as a function of incident wavenumber using both the MDWPM and SBM approaches. The SBM result agrees very well with the MDWPM results across the entire range of wavenumber computed. Results for other system sizes and mode types showed similar model agreement. Minor differences between the two approaches can be accounted for by the fact that the accuracy of the MDWPM approach is limited by the length of wavepacket that can be simulated. The length of the wavepacket that can be simulated is limited by computational resources. To investigate this effect, a wavepacket sensitivity study was performed at one wavenumber. This result presented in Figure Figure 3.4(b). The figure shows that as the wavepacket width is made larger, the transmission results obtained from MDWPM gradually converges to the SBM result which, in essence, represents the infinite wavepacket limit. This gradual convergence with wavenumber was confirmed for other mode types and wavenumbers. The total domain length used to obtain the MDWPM results presented in Figure 3.4(b) was variable and was sized to be large enough to contain the wavepacket and not confuse incident and reflected signals. It was also found that changing the domain length while holding the wavepacket width constant did not affect the transmission result. The

favorable comparison between the MDWPM results, for wavepackets of sufficient width, and the SBM results confirms that the SBM transmission calculation is implemented correctly and can be used with confidence.

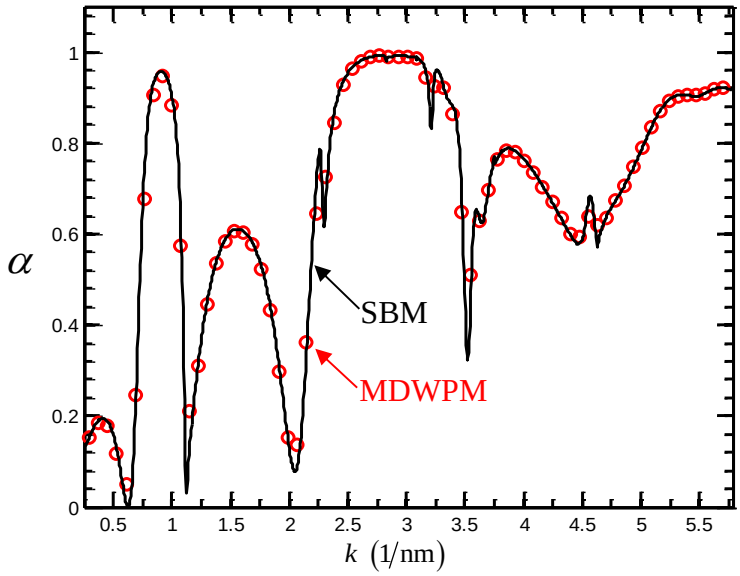

Figure 3.3: Comparison of scattering boundary transmission calculation with MD wavepacket transmission calculation for SH1 propagation through silicon plate with T-stub and rigid walls. Lateral dimension of plate, h_I, is 1.22 nm, width if T-stub region, h_{II}, is 2.44 nm, and length of T-stub, d, is 1.22 nm. The wavepacket width is held constant at 97 nm and the total domain length is 434 nm.

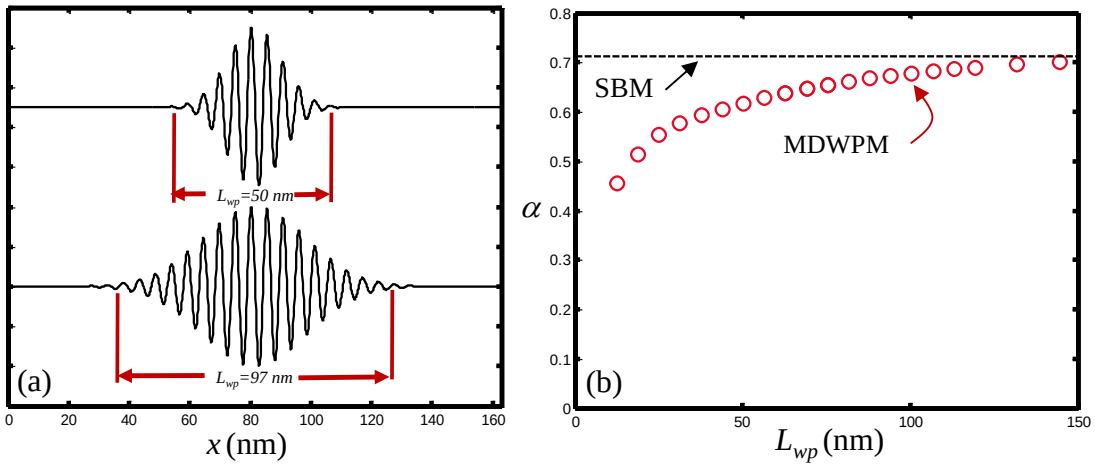

Figure 3.4: (a) illustration of wavepacket width for k_x=1.19 (1/nm). (b) Convergence of MDWPM transmission result with increased wavepacket width. Wider wavepackets better approximate phonons of single wavenumber. Transmission is calculated for SH1 propagation at k_x= 0.759 (1/nm). Red circles correspond to MDWPM results for different wavepacket widths. Black dashed line corresponds to SBM calculation of same mode.

3.6 Chapter Summary

This chapter described the adaptation of the scattering boundary method for the calculation of modal phonon transmission coefficients in geometrically irregular nanostructures. An alternative atomistic computational approach for calculating phonon transmission in comparable systems, the MD wavepacket method, was also presented and its disadvantages which are associated with wavepacket width and computational convenience were highlighted. Using a silicon plate with a T-stub and rigid boundary condition as a case study geometry, the MD wavepacket method was used to verify that the SBM computational model was implemented correctly.

4 Comparison of Atomistic and Continuum Methods for Calculation of Phonon Transmission

4.1 Overview

In this chapter, two methods for calculating shear-horizontal phonon transmission across stepped silicon plate junctions are presented. The first approach, which has been commonly used in previous studies on phonon transport in nanostructures, is based on continuum elastic wave theory and uses eigenmode expansion to solve for the fraction of energy transmitted across the stepped interface. Comparison with results obtained using the scattering boundary approach developed in Chapter 3 applied to the same geometry demonstrates that the continuum approach is only appropriate for modeling the transmission of long wavelength phonons in larger nanostructures. The origin of the disagreement between the two models is discussed and a simple model for estimating an upper bound on the deviation between the two models in the long wavelength, low frequency limit is presented.

4.2 Background

The mode dependent ballistic phonon transmission coefficient, $\alpha_{k,\nu}$, is an important quantity used to characterize phonon transport and predict thermal properties of geometrically irregular nanostructures. $\alpha_{k,\nu}$ is defined as the fraction of energy in a mode type/dispersion branch, ν, and wavenumber, k, that is transmitted across a

geometric feature (see Figure 1.1 for an example geometry). When used with Landauer theory [40], knowledge of $\alpha_{k,\nu}$ for all phonon modes provides a "bottom-up" way of predicting the thermal conductance across a particular geometric element. Most commonly, $\alpha_{k,\nu}$ has been calculated by applying the continuum acoustic analogy and modeling phonons as elastic waves propagating through continuous media. Researchers have used continuum acoustics methods to calculate phonon transmission across "T-stub" resonators [56,57], waveguide constrictions [58], asymmetric waveguide junctions [61], combinations of resonators and cavities [63-65], nanoscale waveguide bends [67], and a number of other nanoscale geometries [69-71]. These studies have uncovered fundamental mechanisms underlying phonon scattering behavior including the role of evanescent phonon modes [58] and the appearance of strongly oscillating transmission curves that result from phonon interference and resonance [56]. It has also been found that resonator and cavity combinations can lead to selective phonon transmission as well as wide frequency gaps in phonon transmission [64] which suggest that specifically designed nanostructure geometry may be useful for obtaining targeted phonon behavior and tuned thermal properties. However, because continuum methods neglect the discrete nature of an atomic lattice, they do not include atomistic effects that can arise when the nanostructure size or the phonon wavelength approaches the interatomic spacing. For long wavelength phonon modes, in nanostructures of sufficient size, continuum models should accurately model phonon interactions with geometrical irregularities.

Alternatively, $\alpha_{k,\nu}$ may be calculated using an atomistic method such as the scattering boundary method (SBM) [82,85] or the molecular dynamics wave packet method (MDWPM) [87,88]. These methods directly include atomic discreteness and as such model phonon interactions with geometry more accurately than continuum models and are applicable for all ranges of phonon wavelengths and frequency. To date there has been very little research published that compares the atomistic and continuum approaches and assesses the limits of applicability of continuum models to atomistic systems. In a recent work, a comparison was made for the case of shear-horizontal modes propagating through a silicon rigid-walled plate waveguide with a T-stub geometric feature and a rigid boundary [92]. However, the scope of that study was limited by the atomistic computational method that was used in the comparison (MDWPM) since that method is extremely computationally demanding due to the large domain sizes required for accurate transmission calculations. In addition, the MDWPM is limited in its ability to tightly define the excited wave number spectrum in the molecular dynamics simulation due to the requirement that the simulated wave packets be finite in size. The limitations of the MDWPM are discussed in greater detail in section 3.4.2 and in the previous work [92].

In this chapter, the lattice dynamics-scattering boundary method (LD-SBM) computational approach which was described in Chapters 2 and 3 is used to perform a more detailed comparison between atomistic and continuum computational approaches to model phonon interactions with geometry. In contrast to MDWPM, LD-SBM is capable of calculating phonon transmission at a precisely defined wavenumber and is much more

computationally efficient since it requires the computational analysis of a much smaller number of atoms. This increases confidence in the atomistic result and facilitates a more comprehensive comparison with continuum theory. Rather than repeating the investigation of the T-stub system, a simpler phonon scattering problem is used to compare the two computational approaches: the transmission of shear-horizontal (SH) modes through a stepped junction between two silicon plate waveguides with free boundaries. This geometry is shown in Figure 4.1. Performing the comparison for this specific system was done for three reasons. First, SH modes in plates are the most easily studied elastic mode family from a continuum analysis standpoint since they consist only of uncoupled shear waves. Other modes, for example Lamb modes in plates and dilatational, flexural, and torsional modes in beams are substantially more complicated and cannot generally be decomposed into uncoupled components. Restricting the study to SH plate modes allows for the use of simple eigenmode expansion computational methods which are not easily applicable to general elastic modes. Moreover, because of the simplicity of the treatment, uncoupled SH modes have been the most commonly investigated class of modes in previously reported geometry induced phonon scattering studies [57,58,64,65]. Second, for the geometry chosen, the transmission of a specific phonon branch depends only on the incident mode's wavenumber and the relative size of the two plates. The small number of parameters involved allows for focus to be placed on atomistic effects dependent on system size and wavenumber without having to exhaustively characterize the effect of other geometric parameters inherent in more

complicated geometries. Third, the free boundary condition is believed to be a more realistic approximation to the actual silicon boundary condition than the rigid boundary condition which was previously employed. The remainder of this chapter is organized as follows: in Section 4.3 the continuum analysis of the problem is presented. In Section 4.4 the atomistic computational approach and geometry used in the comparison are summarized. In Section 4.5, transmission results corresponding to the two approaches are presented. In Section 4.6, the origins for the differences between the two models are discussed. In Section 4.7 the conclusions are summarized.

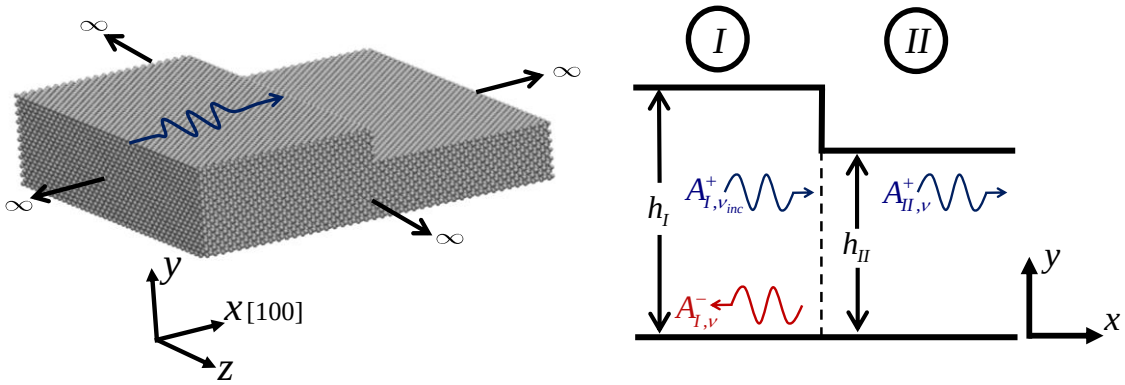

Figure 4.1: Schematic of silicon stepped plate waveguide junction. Direction of phonon propagation is in the x direction which is aligned with the [100] crystal axis. The plate is considered to extend infinitely in y and z directions. Shear-horizontal phonon modes are polarized in the z-direction. The scattering system is deconstructed into two regions, the incident side, labeled I, and the transmitted side, labeled II.

4.3 Continuum Analysis

For the geometry illustrated in Figure 4.1, phonons are incident from plate I and are transmitted to plate II. The wave fields do not vary in the z-direction so that phonon propagation occurs only in the x-direction. In this way, the model system is "quasi-2D" and the continuum analysis can be performed using methods applicable to elastic wave

propagation in anisotropic plates. If the x-axis is aligned with a high symmetry direction of the plate and energy is only incident from plate I, one family of solutions for the displacement field in the two plate sections are given by [53]:

$$\mathbf{u}_{I,SH} = \begin{Bmatrix} 0 \\ 0 \\ \sum_{\nu=1}^{M} F_{I,\nu}(y)\left(A_{I,\nu}^{+}\exp\left[i\left(\omega t - k_{I,\nu}x\right)\right] + A_{I,\nu}^{-}\exp\left[i\left(\omega t + k_{I,\nu}x\right)\right]\right) \end{Bmatrix} \tag{33}$$

$$\mathbf{u}_{II,SH} = \begin{Bmatrix} 0 \\ 0 \\ \sum_{\nu=1}^{M} F_{II,\nu}(y) A_{II,\nu}^{+}\exp\left[i\left(\omega t - k_{II,\nu}x\right)\right] \end{Bmatrix} \tag{34}$$

Here M is the number of phonon modes at the frequency of interest, ν is the mode index, and $A_{\xi,\nu}^{+}\left(A_{\xi,\nu}^{-}\right)$ is the amplitude of a forward (backward) traveling wave of mode type ν in region ξ, which may be I or II. This family of solutions is known as the shear horizontal (SH) set of solutions and has nonzero displacement only in the z-direction. This set of solutions is characterized by a simple dispersion relation [53],

$$k_{\xi,\nu} = \left[\left(\frac{\omega}{V_S}\right)^2 - \left(\frac{\nu\pi}{h_\xi}\right)^2\right]^{\frac{1}{2}} \tag{35}$$

where V_S is the shear wave velocity. The mode shapes for each region are given by:

$$F_{I,\nu}(y)=\begin{cases}1 & \text{for } \nu=0\\ \sqrt{2}\cos\left(\dfrac{\nu\pi y}{h_I}\right) & \text{for } \nu=1,2,3...\end{cases} \tag{36}$$

$$F_{II,\nu}(y)=\begin{cases}\sqrt{\dfrac{h_I}{h_{II}}} & \text{for } \nu=0\\ \sqrt{\dfrac{2h_I}{h_{II}}}\cos\left(\dfrac{\nu\pi y}{h_{II}}\right) & \text{for } \nu=1,2,3...\end{cases} \tag{37}$$

The mode shape represents the variation in z-displacement at a particular y coordinate and satisfies a stress free boundary condition at y=*0* and *y*=h_ξ. To solve for the transmission across the junction the conditions, $\mathbf{u}_I=\mathbf{u}_{II}$, and $\mathbf{T}_I\cdot\mathbf{n}=\mathbf{T}_{II}\cdot\mathbf{n}$, must first be satisfied at the interface between regions I and II. Here, **n** is the normal vector to the interface and **T** is the stress tensor. Since for SH modes there is only one nonzero component of displacement these interface conditions simplify to $u_{z,I}=u_{z,II}$ and $T_{zx,I}=T_{zx,II}$ where $T_{zx,\xi}=c_{44}\dfrac{\partial u_{z,\xi}}{\partial x}$. Eliminating the time dependence, setting the interface location to *x=0*, and dividing by the stiffness constant, c_{44}, which is the same in every region, the interface conditions reduce to:

$$\sum_{\nu}^{M}F_{I,\nu}(y)\left(A_{I,\nu}^{+}+A_{I,\nu}^{-}\right)=\sum_{\nu}^{M}F_{II,\nu}(y)A_{II,\nu}^{+} \tag{38}$$

$$\sum_{\nu}^{M}F_{I,\nu}(y)\left(-k_{I,\nu}A_{I,\nu}^{+}+k_{I,\nu}A_{I,\nu}^{-}\right)=\sum_{\nu}^{M}-F_{II,\nu}(y)k_{II,\nu}A_{II,\nu}^{+} \tag{39}$$

The next step in obtaining the transmission coefficient is to determine the unknown excited mode amplitudes $A_{I,\nu}^{-}$, $A_{II,\nu}^{+}$. This is done by multiplying both sides of the displacement interface condition (Eq. (38)) by $F_{II,\nu'}(y)$ and integrating across the width of plate II. Both sides of the stress interface condition (Eq. (39)) are multiplied by $F_{II,\nu'}(y)$ and integrated across the width of plate I. Here, ν' is a dummy index that spans all modes. Noting that $F_{II,\nu}(y)=0$ for $y>h_{II}$ and using the fact that $\int_0^{h_\xi} F_{\xi,\nu}(y)F_{\xi,\nu'}(y)\,dy=\delta_{\nu\nu'}$, where $\delta_{\nu\nu'}$ is equal to one for $\nu=\nu'$ and zero otherwise, the following linear system is obtained.

$$\begin{bmatrix} \mathbf{\Phi^T} & \mathbf{-I} \\ \mathbf{K_I} & \mathbf{\Phi K_{II}} \end{bmatrix} \begin{Bmatrix} \mathbf{A_I^-} \\ \mathbf{A_{II}^+} \end{Bmatrix} = \begin{Bmatrix} \mathbf{-\Phi^T A_I^+} \\ \mathbf{K_I A_I^+} \end{Bmatrix} \tag{40}$$

Here, the elements of the *M* by *M* expansion coefficient matrix $\mathbf{\Phi}$ are $\Phi_{\nu\nu'}=\int_0^{h_{II}} F_{I,\nu}(y)F_{II,\nu'}(y)dy$. The elements of the *M* by *M* wavenumber matrices $\mathbf{K_\xi}$ are diagonal with elements $\left(K_\xi\right)_{\nu,\nu}=k_{\xi,\nu}$. The vectors $\mathbf{A_\xi^\pm}$ contain the amplitudes of the excited modes, $A_{\xi,\nu}^{\pm}$, in each region and are of length *M*. $A_{I,\nu}^{+}$ is assumed to be one for the incident mode and zero for all other modes. Equation (40) is solved for the unknown mode amplitudes and the transmission coefficient, $\alpha_{k,\nu_{inc}}$, and reflection coefficient, $\eta_{k,\nu_{inc}}$, of the incident mode, ν_{inc}, can be calculated using [57]:

$$\alpha_{k,\nu_{inc}} = \sum_{\nu=1}^{M_{prop}} \frac{A^{+}_{II,\nu}\bar{A}^{+}_{II,\nu}k_{II,\nu}}{k_{I,\nu_{inc}}} \tag{41}$$

$$\eta_{k,\nu_{inc}} = \sum_{\nu=1}^{M_{prop}} \frac{A^{-}_{I,\nu}\ \bar{A}^{-}_{I,\nu}k_{I,\nu}}{k_{I,\nu_{inc}}}\ . \tag{42}$$

Here, $\bar{A}^{\pm}_{\xi,\nu}$ indicates the complex conjugate of $A^{\pm}_{\xi,\nu}$. Note that complex amplitudes are required to account for phase differences in the displacement fields associated with different modes. For simplicity, equations (38)-(40) are calculated using the same finite number of modes in regions I and II. In principle, the calculation would include an infinite number of modes. However, in practice, all of the propagating modes (those with real wavenumbers), and the first several non-propagating modes (those with imaginary wavenumbers) are included in the construction of the expansion coefficient matrices. The actual number of non-propagating modes that are necessary varies depending on the frequency. The total number of modes used in each calculation was increased until the transmission calculation converged to a constant value that was independent of number of modes included. Five non-propagating modes is typically a large enough number for an accurate transmission calculation. The summation over modes in the calculation of transmission and reflection coefficients for a given incident mode (Eqs. (41) and (42)) includes only the M_{prop} propagating modes with purely real wavenumber since only these modes carry energy. While evanescent modes are not included in the transmission calculation, they are required to properly resolve the displacement field near the plate junction and accurately determine the excited mode amplitudes. To ensure energy

conservation, it has been verified for all cases presented herein that the sum of the transmission and reflection coefficients is equal to one.

4.4 Atomistic Analysis

The atomistic model used follows the LD-SBM computational method as described earlier in this dissertation. The plate junction is decomposed as illustrated in Figure 4.2. The phonon spectrum of each plate lead is analyzed using the harmonic lattice dynamics techniques described in Chapter 2. The transmission calculation follows the scattering boundary method described in Chapter 3.

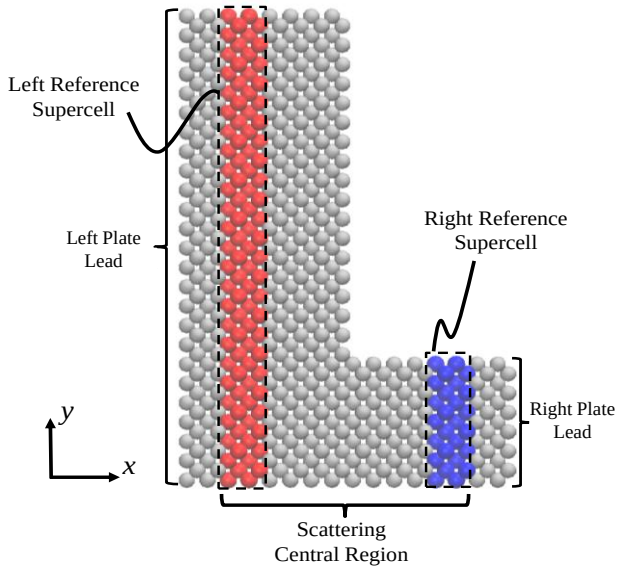

Figure 4.2: Illustration of geometry used in atomistic analysis. Computational domain decomposed into left and right plate leads and the scattering central region. These regions and their roles in the transmission calculation are defined in Chapter 3. Periodic boundary conditions are employed in the z-direction.

In order to calculate the modal transmission coefficients of the shear-horizontal modes, first the full dispersion relation of the incident side plate lead is calculated. The

phonon branches analogous to the continuum SH modes are identified through comparison of the atomistic and continuum dispersion relations and inspection of each mode's mode shape. The transmission along each SH phonon branch is systematically calculated across a range of desired wavenumber. The investigation is limited to the first four shear-horizontal modes, SH0, SH1, SH2, and SH3 (corresponding to ν=0,1,2,3). An example phonon spectrum along the [100] direction is presented in Figure 4.3. The full phonon dispersion is plotted in Figure 4.3(a). The low frequency, low wavenumber regime that is investigated in this study is plotted in a larger figure in Figure 4.3 (b). The branches corresponding to the first four SH modes are plotted in blue and labeled according to mode number. The other low frequency phonon branches, which are Lamb modes, are colored in orange, but are not investigated in this study.

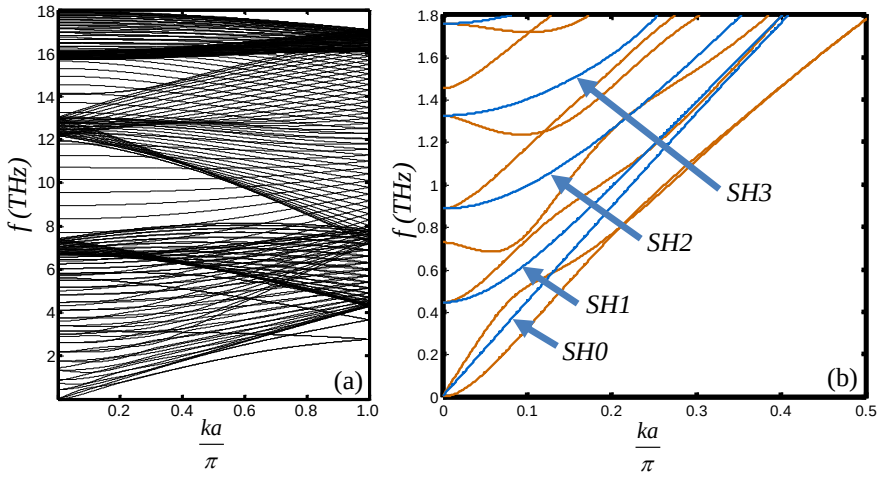

Figure 4.3: Phonon spectrum for silicon plate waveguide along for phonon propagation aligned with the [100] crystal axis. The dimensionless plate width is h_l/a=12, (corresponds to h_l=6.52nm). The first four shear-horizontal modes that are of interest in this study are colored blue and labeled in the figure. Lamb modes, which are not investigated herein, are plotted in orange.

4.5 Model Comparison

4.5.1 *Transmission Results for SH0*

Transmission results associated with the atomistic and continuum modeling approaches corresponding to the SH0 mode are compared in Figure 4.4. The results are plotted against dimensionless wavenumber, *ka*, where *a* is the lattice parameter. Three different plate sizes are compared, but the ratio between the heights, $h_{II}^{*} = \frac{h_{II}}{h_{I}}$, of the two plates is held constant at $h_{II}^{*} = 0.25$. While the results associated with only one value of h_{II}^{*} are presented in detail herein, the qualitative shape of the continuum transmission curve remains the same independent of h_{II}^{*}. The transmission approaches a constant value at low wavenumbers. The long wavelength limit can be analytically derived following the same analysis presented in Section 4.3, but by assuming that only SH0 modes participate in the scattering process. This results in a long wavelength SH0 transmission given by:

$$\alpha_{\mathrm{SH0},k\to 0} = \frac{4h_{II}^{*}}{\left(1+h_{II}^{*}\right)^{2}} \tag{43}$$

Such a derivation is appropriate and expected since at low wavenumbers the displacement fields associated with all of the higher order modes decay immediately away from the stepped plate interface since they have large and imaginary components of wavenumber. As such, coupling with higher order modes is negligible and only the

interactions between the SH0 modes in each plate need to be considered. At higher wavenumbers, the transmission exhibits strong discontinuities at regular intervals of wavenumber (kh=1,2,3,…). Each of these discontinuities occur when the incident phonon frequency is equal to the cutoff frequency of a higher order SH mode (e.g. SH1, SH2,…). The magnitude of the discontinuities decreases with increasing wavenumber and eventually the transmission approaches a short wavelength limit. The transmission of the short wavelength SH0 modes was empirically found to approach a value of:

$$\alpha_{\mathrm{SH0},k\to\infty} = h_{II}^{*} \tag{44}$$

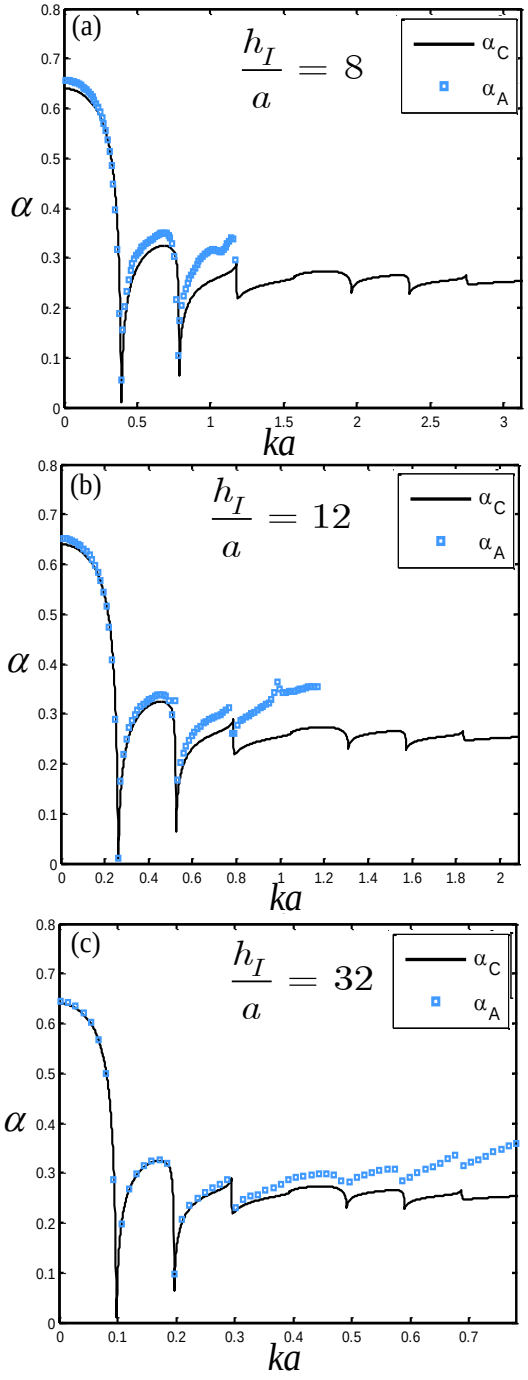

Figure 4.4: Atomistic transmission as compared to continuum transmission for SH0 mode as a function of incident mode dimensionless wavenumber, *ka*. h_{II}^{*} is held constant at 0.25. Increasing the plate size improves model agreement for low wavenumber modes. Atomistic "wavelength" effects are demonstrated higher wavenumbers as atomistic transmission result diverges from continuum.

The transmission coefficients calculated using the LD-SBM atomistic model, α_A, agree well with the continuum transmission, α_C, obtained from Eq. (41) at low wavenumbers, but significant deviation between the two models is observed at high wavenumbers. The origin of this disagreement is discussed in detail in Section 4.6.1. Slight deviation between the two models occurs at low wavenumber, but deviation lessens with larger plate sizes. This behavior is explained and further characterized in Section 4.6.2.

4.5.2 *Transmission Results for SH1, SH2, and SH3*

The comparison of transmission results for the SH1, SH2, and SH3 modes are presented in Figure 4.5. Two different plate sizes are presented and the plate size ratio, h_{II}^*, is held constant at 0.25. Similar to the results presented for SH0, the atomistic and continuum results for these modes tend to exhibit better agreement at low wavenumbers, but substantial disagreement between models is observed at higher wavenumbers. Deviation between the models that occurs at lower wavenumbers is more severe for the smaller plate size presented. In addition, model agreement worsens as mode order increases. That is, the agreement for SH3 is worse than for SH2 and SH2 is worse than SH1. All of these effects are discussed and explained in Section 4.6.

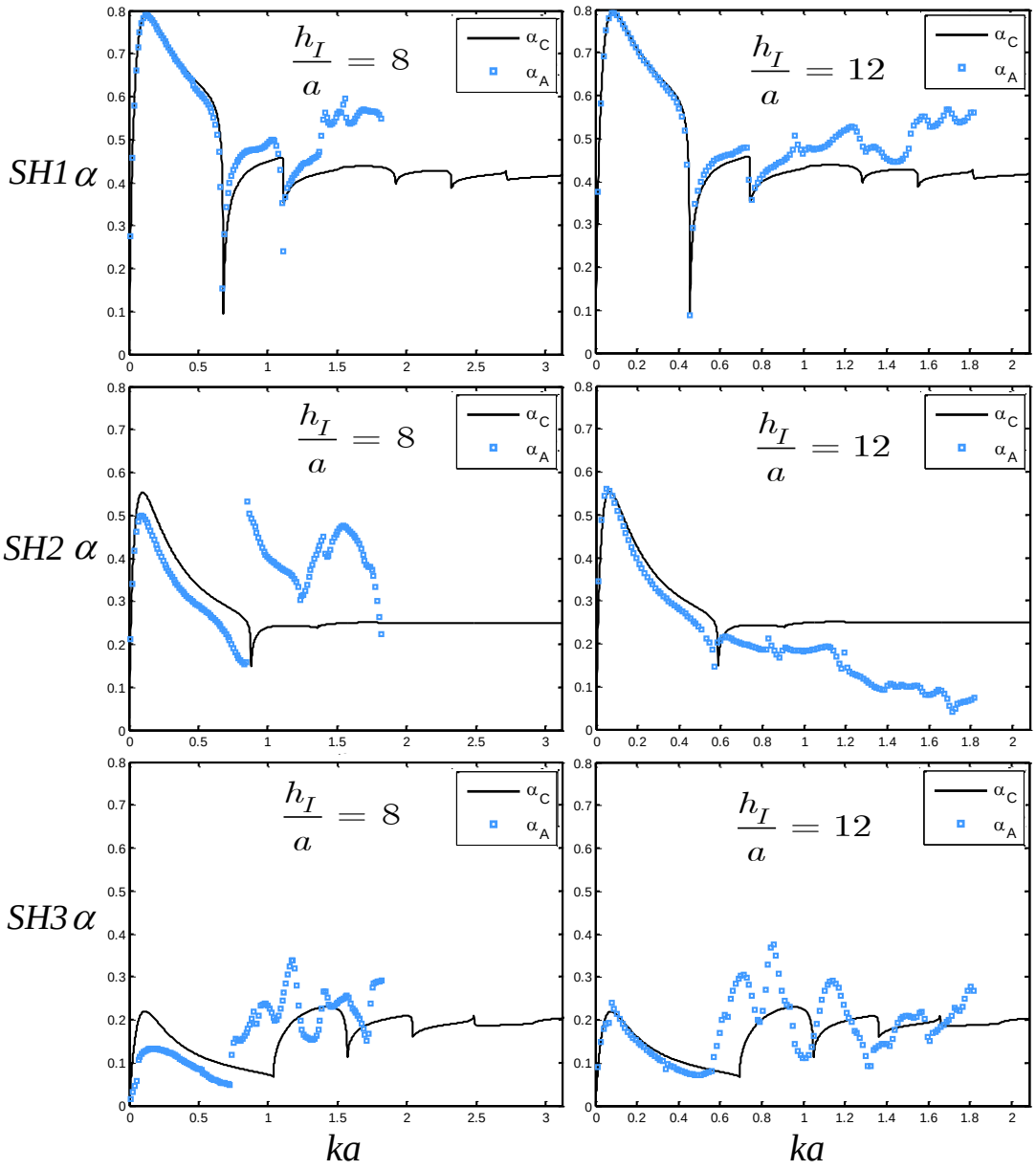

Figure 4.5: Atomistic transmission as compared to continuum transmission for SH1, SH2, and SH3 modes as a function of incident mode dimensionless wavenumber, *ka*. h_{II}^{*} is held constant at 0.25. Two different system sizes were investigated as annotated in the figure.

4.6 Origins of Differences Between Models

Differences between the continuum model and the atomistic model arise from atomistic effects that can be loosely categorized as being either nanostructure size effects or phonon wavelength effects.

4.6.1 *Atomistic Wavelength Effects*

For the results presented in Figure 4.4 and Figure 4.5, the deviation between the models that occurs at higher wavenumbers results from atomistic wavelength effects. Wavelength effects arise when the phonon wavelength, $\lambda = \frac{2\pi}{k}$, gets smaller and approaches the length scale of the atomic discreteness. For this reason, wavelength effects are characterized using the dimensionless parameter *ka*. At high values of *ka* the spatial variation of atomic displacements is too rapid, relative to the interatomic spacing, to be adequately modeled using continuous displacement fields. The divergence from continuum in an atomistic system at higher wavenumbers was confirmed for many different waveguide sizes and several values of h_{II}^{*}. It was found that no matter the system size the models always diverged from one another at higher wavenumbers. However, the wavenumber threshold at which this transition occurs as well as the rate of the transition depends on the specific geometry. There is appreciable variation in where the transition occurs which makes it difficult to define the transition wavenumber with precision. However, in the cases investigated, atomistic effects generally become non-

negligible between *ka* equal to 0.40 and 0.80. This corresponds to wavelengths less than between approximately 4 and 8 nm.

Additional wavelength effects occur for the higher order modes, SH1, SH2, and SH3. The *ka* parameter only characterizes the longitudinal variation of atomic displacements relative to the lattice spacing. Higher order modes exhibit additional variation in the displacement field that is transverse to the direction of propagation. This is why, for a fixed value of *ka*, model agreement worsens as mode order increases (see Figure 4.5).

It was found that the deviation observed at higher wavenumbers as well as for higher order modes is associated with deviations between the atomistically calculated mode shapes (from harmonic lattice dynamics) and the continuum model (from equation (37)). The atomistically calculated mode shapes of the first four SH modes are compared to continuum at small and larger wavenumbers in Figure 4.6. At low wavenumbers and the lowest order modes there is negligible disagreement between the two mode shape models. However, for the higher order modes (even at very low wavenumbers) and all modes at higher wavenumbers, there is appreciable disagreement between the two mode shape models. These differences in mode shape gradually become worse as the wavenumber is increased. The atomistically calculated mode shapes differ from the continuum in two ways. First, the lateral dependence on z component of displacement changes with wavenumber and the agreement with continuum tends to worsen at higher wavenumbers. Second, while continuum theory predicts that displacements in the x and

y directions are completely decoupled from motions in the z-direction and should not appear in SH modes, it is found that atomistically calculated mode shapes for SH modes do include x and y displacement that is non zero. The amount of x and y displacement increases with increasing wavenumber and the agreement between models at a given wavenumber worsens for higher order modes which have lower transverse wavelength. Since both the continuum and atomistic transmission calculation methodologies are intimately linked to their respective mode shapes, any deviation in mode shape calculations will cause the transmission results to differ.

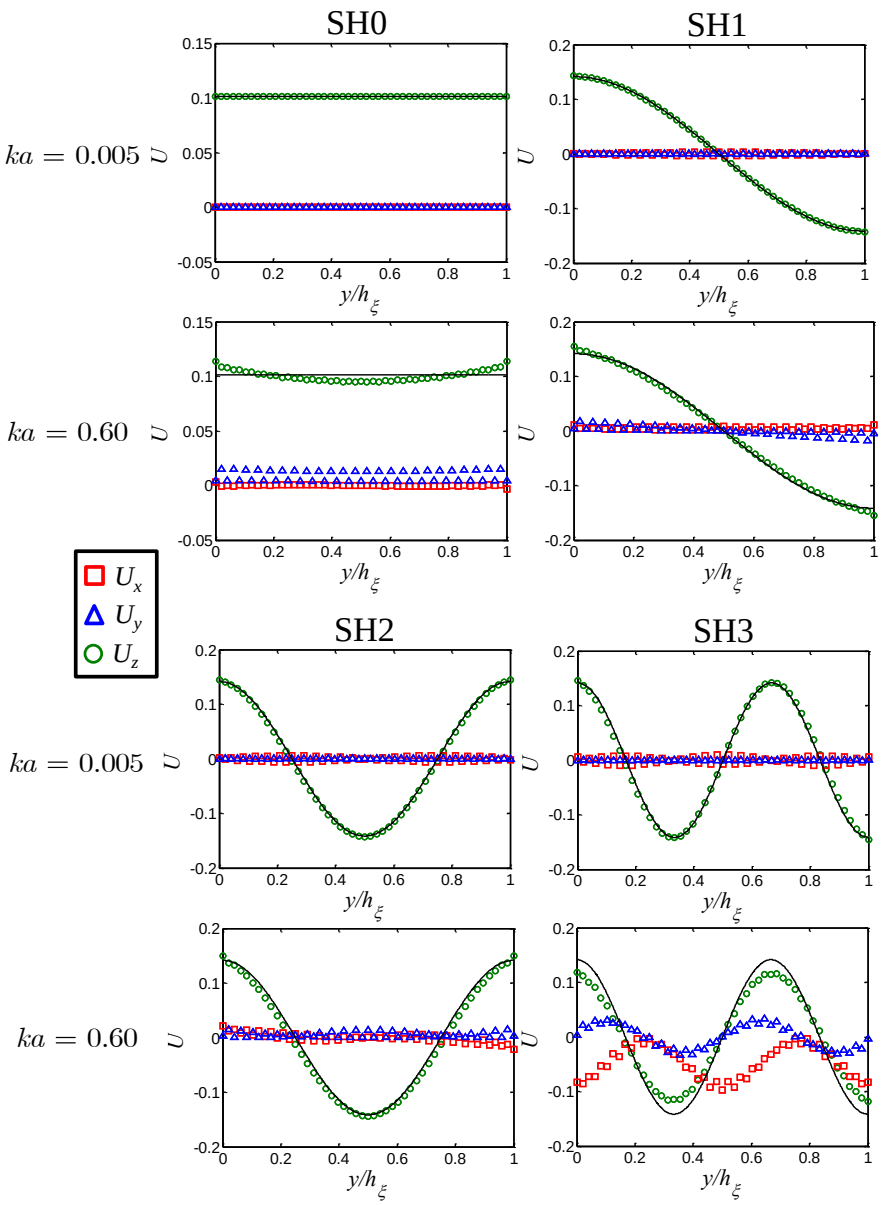

Figure 4.6: Comparison of normalized continuum and atomistic normal mode shapes of first four SH modes for $h_l/a = 12$. The colored markers indicate the atomistic result. Green circles correspond to displacement in the z-direction. Red squares and blue triangles correspond to x and y displacement, respectively. Note that the plotted y displacement mode shape is 90 degrees out of phase with the z and x displacement. The black lines indicate the continuum mode shape corresponding to each mode. In the continuum model, motions in the z-direction are completely decoupled from x and y motions, so that the only non-zero component of displacement for SH modes is in the z direction. Note that for atomistic results not all atoms in a supercell share the same equilibrium x or z positions.

4.6.2 *Atomistic Size Effects*

While the most noticeable difference between the two models occurs at high wavenumbers and results from atomistic wavelength effects, there is an additional source of deviation between the two models that can persist independent of the phonon wavelength. These effects are denoted size effects and occur when the width of either plate section, h_I *or* h_{II}, approaches the length scale of the atomic discreteness. Here, the lattice parameter (a=0.543nm) is chosen as the relevant length scale of the atomic discreteness and the dimensionless parameter h_I/a is used to characterize how the size of the system compares to the atomic discreteness.

Included among nanostructure size effects are atomistic roughness effects, dimensional uncertainty effects, and non-uniform stiffness effects. Due to the nature of the atomic lattice, the plate boundary as well as the topography of the stepped plate interface are inherently rough. For example, neighboring atoms at the plate boundaries may not have the same equilibrium y position. Similarly, neighboring atoms at the stepped plate-plate interface may not have the same equilibrium x position. Thus, both the plate interface and the plate boundaries will have a jagged topology that only appears smooth when h_I/a is large. This is the atomistic roughness effect and is illustrate in Figure 4.7. A related set of effects are denoted dimensional uncertainty effects. Since atoms at the plate boundary do not all have the same equilibrium y position, there is an inherent ambiguity in determining the dimension of both h_I and h_{II}. The continuum model includes sharp and precisely defined interfaces and boundaries. It is difficult to

define sharp interfaces/boundaries in the atomistic system since it is unclear if the interface or boundary should be defined between atomic layers or at layer centers. This uncertainty leads to uncertainty in the measurement of h_I and h_{II} both of which are required for the continuum transmission calculation. For the results presented herein, any plate height, h_ξ, is defined as the distance between the centers of the outermost boundary atomic layers.

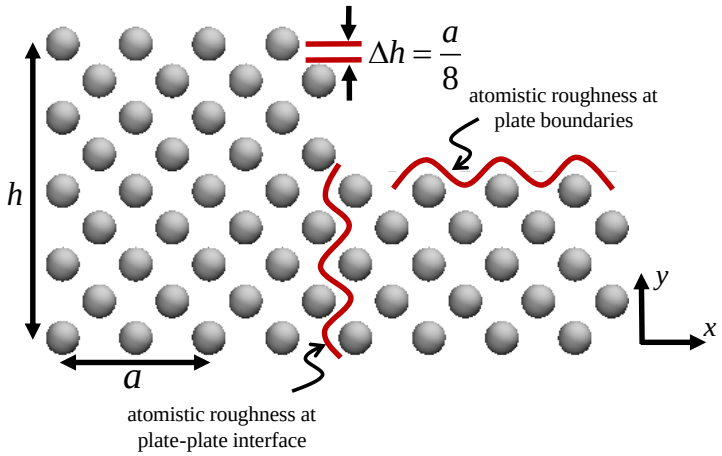

Figure 4.7: Illustration of atomistic size effects. Discrete atomic lattice causes inherent roughness at plate boundaries and at plate-plate interfaces. In addition, the discrete lattice results in ambiguity in defining the height, *h*, of the plates, resulting in an uncertainty in the height definition, Δh. For this study, *h*, is chosen to be measured from the centers of the atoms at the plate boundaries as shown in the figure.

Another size related atomistic effect, the non-uniform stiffness effect, arises from the fact that as h_ξ becomes smaller, a higher fraction of the atoms in each plate are near or at the plate boundary. Because the boundary is free, atoms near or at the boundary experience forces that are different than those closer to the plate center. As result, the elastic stiffness varies across the plate width and is less stiff near the plate boundaries. In addition, the overall effective material properties such as the relevant shear stiffness, c_{44},

and shear velocity, V_S differ between plates of different sizes. As the plate is made larger, the stiffness properties of the plate approach that of bulk, and this atomistic effect is minimized. To illustrate this effect, the group velocity was computed from numerical differentiation of the dispersion curve of the SH0 mode in the long wavelength limit as a function of plate size. This result is plotted in Figure 4.8. The group velocity of the SH0 mode is slightly reduced for smaller plate sizes. For larger plate sizes, the calculated group velocity converges to the expected continuum shear velocity ($V_S = \sqrt{c_{44}/\rho} = 4920$ m/s). The bulk shear stiffness, $c_{44} = 56.4$ GPa , was taken from a lattice dynamics study [55] of bulk Stillinger-Weber silicon. The height dependence of the SH0 mode velocity clearly demonstrates that atomistic boundary effects can alter overall elastic properties. This affects atomistic phonon transmission and its agreement with continuum theory since continuum theory relies upon the assumption of material properties that are both size and wavenumber independent.

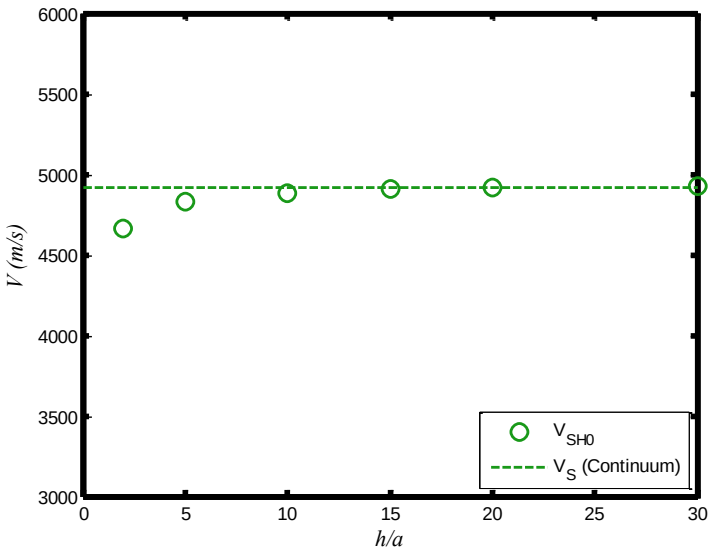

Figure 4.8: Atomistically calculated SH0 mode velocity in the long wavelength limit (markers) as a function of plate size. SH0 mode velocity is reduced for smaller plate sizes but converges to the continuum value when the size of the plate is much larger than the interatomic spacing.

In order to isolate nanostructure size effects from atomistic wavelength effects focus is placed on the deviation between the atomistic and the continuum models for the SH0 mode in the long wavelength limit (*ka* near zero). For an example of this deviation note the small difference between atomistic and continuum transmission results apparent near k=0 in Figure 4.4(a). Since the spatial variation of atomic displacements associated with these modes is small, atomistic wavelength effects are minimized and the only possible source of deviation arises from atomistic size effects. In the investigation of this regime, the atomistic transmission of the SH0 mode was calculated for k near zero and compared with the continuum value (Eq. (43)). The effect of nanostructure size was specifically investigated by varying the value of h_I. Four different values of h_{II}^* were investigation. The percent difference between the atomistic model and the long

wavelength continuum model is shown in Figure 4.9. For SH0 modes in the long wavelength limit, the deviation between the atomistic and the continuum model gets smaller as h_I is increased. This is because increasing plate width reduces dimensional uncertainty and the relative importance of atomistic roughness and non-uniform stiffness effects. For h_I/a greater than 20, the deviation between the atomistic model and the continuum model is less than 1% for all values of h_{II}^* investigated. For h_I/a greater than 5, the deviation between the atomistic model and the continuum model is less than 5% for all values of h_{II}^* investigated. The figure shows that only the smallest two values of h_{II}^* investigated resulted in appreciable disagreement between models and this was only for small values of h_I/a. The deviation between the atomistic model and the continuum model for long wavelengths is less for larger values of h_{II}^*.

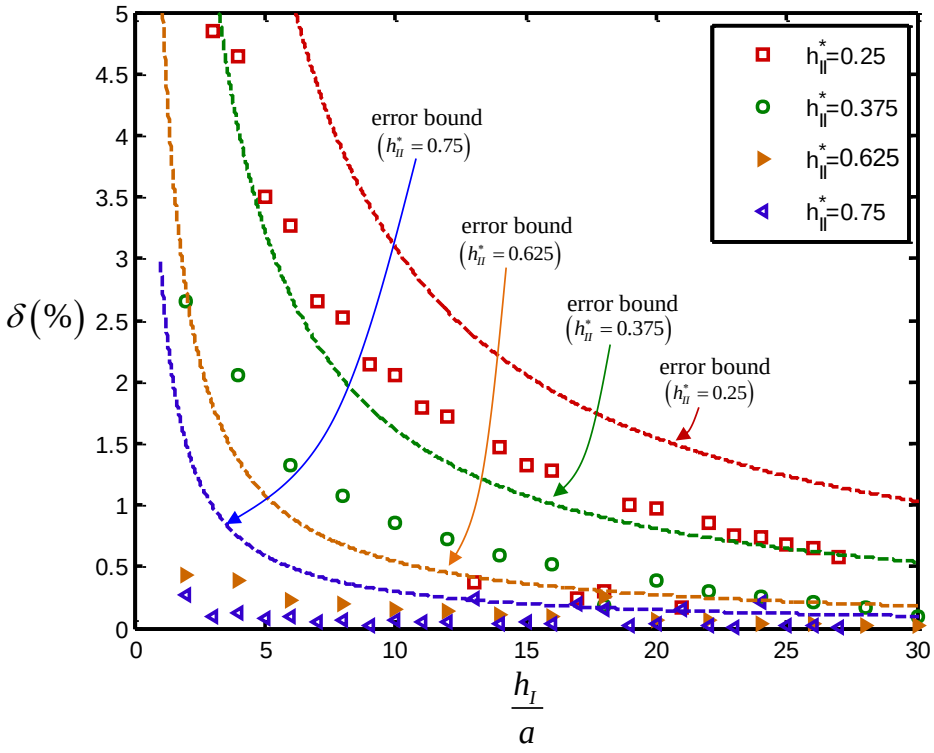

Figure 4.9: Percent difference between atomistic and continuum models for SH0 mode in the long wavelength limit. Calculated deviation between models for different values of h_{II}^{*} are plotted according to the markers shown in the legend. The dashed lines are the estimated upper bound for "dimensional uncertainty" as calculated using equation (46). The colors of the dashed lines correspond to the coloring of the markers for each value of h_{II}^{*} .

It is hypothesized that the greatest source of deviation between the models arises from what is described as dimensional uncertainty which in the long wavelength limit leads only to uncertainty in the parameter h_{II}^{*} which is used in the continuum long wavelength calculation. Using standard propagation of uncertainty techniques [94], an expression for the expected upper error bound, $\Delta\alpha_{du}$, arising only from the dimensional uncertainty, Δh, in h_{ξ} can be estimated from:

$$\Delta\alpha_{du} = \left[\left(\frac{\partial \alpha_{\mathrm{SH0},k\to 0}}{\partial h_I} \right)^2 (\Delta h)^2 + \left(\frac{\partial \alpha_{\mathrm{SH0},k\to 0}}{\partial h_{II}} \right)^2 (\Delta h)^2 \right]^{\frac{1}{2}} \tag{45}$$

Which, upon simplification and substitution of $h_{II}^* = \frac{h_{II}}{h_I}$ yields:

$$\Delta\alpha_{du} \approx \Delta h \frac{4\left(h_I - h_{II}^* h_I\right)}{\left(h_I + h_{II}^* h_I\right)^3} h_I \sqrt{\left(1 + h_{II}^*\right)} \tag{46}$$

The uncertainty in h_ξ is estimated to be $\Delta h = \frac{a}{8}$. This value corresponds to half the distance between atomic layers. The expected upper error bound, $\Delta\alpha_{du}$, is calculated using Eq. (46) and compared with the actual calculated deviation between the two models. This estimated upper bound on model deviation is plotted in dashed lines alongside the actual deviation between models in Fig. 3. It was found that equation (46) serves as a good estimator of the upper bound for expected deviation between the models in the long wavelength limit as all data points fall below the line and closely track the trend. Additionally, explaining the deviation in this manner demonstrates why larger values of h_{II}^* result in closer agreement between the atomistic and the continuum model. Comparison with this model, which is based solely on deviations associated with dimensional uncertainty, indicates that atomistic roughness and non-uniform stiffness affect transmission much less than dimensional uncertainty. It is also noted that the

maximum deviation resulting from dimensional uncertainty occurs as h_{II}^{*} approaches zero and gives a limiting value of $\Delta\alpha_{du} \approx \frac{4\Delta h}{h_I}$.

4.7 Conclusions

Two different computational approaches were used to calculate shear-horizontal phonon transmission across stepped silicon plate junctions. The first approach, which is based on continuum elastic wave theory, follows the same procedures used in previous studies of phonon transmission in geometrically irregular nanostructures. The second approach directly models the vibrations of individual atoms and therefore includes effects related to the discrete nature of an atomic lattice. The two models were compared for the first four SH phonon branches over a range of wavenumber. The most significant deviation between the two models was observed for short wavelength modes and was shown to be related to disagreement between each approach's mode shape models. In addition, the results indicate that rapid variations in atomic displacement in the direction transverse to the propagation direction (characteristic of higher order modes) leads to further disagreement between the continuum and atomistic approaches that is evident in both the mode shape and transmission results. Another source of deviation, denoted atomistic size effects, was found to be an additional contributor to differences between the two models. Atomistic size effects were isolated by analyzing the differences in transmission of long wavelength SH0 modes. A simple analytical model based upon

dimensional uncertainty in the atomistic system was developed that estimates an upper bound on the deviation between the models for these modes. Consistent with the results from the model comparison, the simple model predicts less deviation for larger sizes and size ratios. Although the specific continuum method presented herein is only valid for uncoupled shear horizontal mode propagation in quasi-2D (plate-like) nanostructures, similar deviations between atomistic and continuum models can be expected for any phonon mode type and in other types of nanoscale geometries such as nanowires and nanoribbons.

5 Simple Model for Phonon Transmission Across Abrupt Nanowire Discontinuities

5.1 Introduction

5.1.1 *Chapter Overview*

In this chapter, a simple analytical model for estimating the ballistic transmission coefficient of guided phonons in nanowires with abrupt geometric and material discontinuities is presented. The model includes separate consideration of each of the four lowest frequency nanowire phonon modes-one extensional, one torsional, and two flexural modes-and is based upon the long wavelength behavior of these modes as analyzed using continuum elastic wave theory of prismatic beams. The model is presented using a transfer matrix approach that can be applied to a nanowire with any number of discontinuities and arbitrary but piecewise constant cross-section. Simplified analytical expressions for a step junction of two coaxial nanowires with different diameters and for a nanowire with a central coaxial constriction or expansion are also presented. For the test case of a cylindrical silicon nanowire system, the analytical model is compared with modal transmission coefficients calculated using the lattice dynamics - scattering boundary method (LD–SBM) approach described in Chapters 2 and 3. Despite the simplicity of the analytical model, good agreement is found between the simple model and the LD-SBM model for small wavenumbers.

5.1.2 *Background and Motivation for Simple Model*

Geometry induced phonon scattering events are complicated processes that depend on many different variables including, at a minimum, nanostructure size, shape, constituent atom type, crystal orientation, and the properties of the incident phonon mode (i.e. its wavenumber and dispersion branch). In a more detailed case, the phonon-geometry scattering problem may also include dependence on material impurities, crystal defects, lattice strain, and relaxation of the crystal lattice near nanostructure boundaries. However, given a suitable empirical interatomic potential (or more complicated and computationally expensive ab initio interatomic force calculations) and a known or calculated atomic configuration, many of these complications can be accounted for and transmission coefficients can be computed using an atomistic computational method such as those described in Chapter 3. Unfortunately, these calculations require considerable effort in both problem set-up (e.g. specifying atomic positions and interatomic forces) and computation (e.g. solving systems of equations with thousands of unknowns or executing MD simulations with hundreds of thousands of particles). For instance, a typical scattering boundary transmission calculation for an Si nanowire of diameter less than 5 nm requires solving a system of equations with more than 6000 unknowns. The substantial computational effort associated with the aforementioned detailed transmission calculation methodologies limits their ease of use. Furthermore, for an arbitrary geometry, the scattering process may involve conversion from a single incident mode to many different reflected and transmitted modes, the excitation of higher order modes as

well as evanescent modes localized to an irregular geometry, and complicated overlapping of resonant phenomena associated with each excited mode. These factors can give rise to mode dependent transmission curves that are very complicated functions of incident phonon wavenumber (or, alternatively, frequency) that may exhibit strong peaks and valleys in transmission with no easily discerned relation to the nanostructure geometry or the properties of the incident phonon. The complicated, and sometimes non-intuitive, transmission behavior predicted by these methods give little clarity to the problem of designing nanostructures for "tuned" phonon transmission behavior.

One approach that has been used that avoids the some of the difficulties associated with the more complicated and computationally expensive atomistic approaches is to use continuum acoustic theory to model phonon transport. As discussed in Chapter 4 and in another work [93], this approach has been shown to accurately match more complicated atomistic calculations for low frequency modes in the long wavelength limit. However, as discussed in Chapter 3, many recent studies using this approach have employed continuum scalar wave models that are greatly simplified when compared to systems of real practical interest, for example geometrically modified semiconductor nanowires. More complicated continuum elastic theories applicable to anisotropic nanowires (see, for example, the method formulated in [41]), or finite element numerical approaches [73,74] could provide more accurate representations of phonon dynamics in nanowires, but these approaches are still considerably complicated because finding the dispersion relation alone requires the numerical solution to transcendental equations of

varying complexity. Application to scattering problems would further compound their complexity and undermine the advantages continuum models have over atomistic models.

Since the currently available computational approaches to calculating phonon transmission in geometrically irregular nanoscale systems are either too simple for accurate application to nanowire geometries or too computationally expensive and complicated for easy use, it is desirable to develop simpler geometric phonon transmission models that can be more easily used within the nanoscale thermal transport community. One means of attaining such a model is by focusing only on phonon scattering behavior in the low-frequency, long wavelength limit. Since these long wavelength-low-frequency modes are the most important modes for thermal transport in the low temperature ballistic regime, a model for these modes provides a first step toward designing nanostructures for tuned phonon transport performance and establishes a baseline to which more generally applicable models can be compared. In this chapter a model for phonon transmission in nanowires with irregular geometry is presented. The model is derived from elementary elastic beam theory and is valid for the four lowest frequency phonon branches in the long wavelength limit. The model offers a way of understanding geometry induced phonon scattering in nanowires that is both more intuitive and less computationally demanding than that offered by more complicated computational models. The analytical model and the nanowire geometry to which it is applicable are described in section 5.2. In order to assess the accuracy of the model and

delineate its regime of applicability, the simple analytical model is compared with atomistic calculations of modal phonon transmission in simple cylindrical silicon nanowire systems. The atomistic calculations are performed using the lattice dynamics-scattering boundary method approach described in Chapters 2 and 3 of this dissertation. In section 5.3, the results of the comparison are presented. The origin of the deviation between the two models is discussed and a regime of applicability for the simple model is recommended.

5.2 Analytical Model for Phonon Transmission Coefficient

5.2.1 *Overview of Nanowire Geometry and Low Frequency Modes*

This study is concerned with the analysis of an irregular nanowire with an arbitrary number of abrupt geometric and material discontinuities (Figure 5.1). The nanowire is decomposed into $N+1$ nanowire sections joined together at N abrupt interfaces. Each nanowire section is identified with the index ξ. Each nanowire section is coaxial with the others, has constant material properties and piecewise constant cross-section. The model requires that each cross-section has similar shape and orientation but is formulated to allow for each section to have different size and/or material properties. The last and first nanowire sections extend semi-infinitely along the nanowire axis (x-axis).

Figure 5.1: Illustration of nanowire scattering system comprised of *N+1* nanowire sections adjoined at *N* abrupt interfaces. The first and last nanowire sections extend semi-infinitely.

Each nanowire section will have many phonon modes but all except the four lowest frequency mode types have non-zero cutoff frequencies. These four mode types, which include one extensional branch, one torsional branch and two flexural branches propagate down to zero frequency and are known as the "zeroth order" modes. Due to their relatively high velocities and phonon populations, these four mode types are the most important modes for thermal transport at low temperatures. The foundation of the phonon scattering model presented herein is that the atomic motions associated with the four lowest modes are governed by one-dimensional differential equations that result from the approximate long wavelength analysis of these modes.

5.2.2 *One-Dimensional Beam Model*

In general, the atomic motions associated with these modes will have components in the direction of the nanowire axis (*x*-direction) as well as is in the plane of the nanowire cross-section (y-z plane). However, continuum elastic wave theory shows that for the long wavelength case, $kD<<1$, these motions decouple into motions that are either primarily in the axial direction (the extensional mode), tangential to the nanowire axis (torsional mode), or consist of pure bending in the y or z directions (two flexural modes)

[94]. The simplified uncoupled nature of these modes at long wavelengths allows for the approximate treatment of these modes with one-dimensional beam models.

The model for extensional motions is based upon the assumption that the cross-sectional area of the nanowire remains in plane such that the only non-zero component of displacement is along the nanowire axis. Consideration of the forces acting on a differential element results in a harmonic 1-D wave equation for axial component of displacement, u_x, with an associated phase velocity equal to $\sqrt{E/\rho}$ where E is the Young's modulus and ρ is the mass density. The model for torsional motions is based upon St. Venant's theory of torsion for a prismatic beam [96], and results in a 1-D wave equation for the angle of twist, θ, with associated torsional phase velocity equal to $\sqrt{J/I_P\rho}$, where J is the torsional rigidity of the nanowire cross-section and I_P is the polar moment of inertia. For flexural modes the Bernoulli-Euler mode is used under which it is assumed that the dominant component of displacement is parallel with the plane of the beam cross-section [94]. It is also assumed that the displacement is uniform along the beam cross-section and that cross-sectional areas remain in plane and perpendicular to the neutral axis. In contrast to the simple models used for extensional and torsional motions, the Bernoulli-Euler model for flexural motions includes evanescent motions that decay away from each nanowire interface. Further, the Bernoulli-Euler model results in a dispersion model whereby the frequency is

proportional to the wavenumber squared. More in depth discussion of these long wavelength models and their derivation can be found in Ref. [94].

The governing equations, general solutions for each region, and dispersion relations associated with these simple 1-D models are presented in Table 5.1.

5.2.3 *Determination of Transmission Coefficient*

The phonon transmission associated with a single mode incident from the left can be determined by relating the modal amplitudes in each region across the interfaces that adjoin them. Following the approach of Cross and Lifshitz in their investigation of elastic wave transport across abrupt junctions in mesoscopic thin plates [97], the amplitudes across each nanowire section are related by imposing conditions of continuity that are unique to each mode type. Extensional motions satisfy conditions of continuity on axial displacement and axial force, $F = SE\frac{\partial u_x}{\partial x}$, at each interface. Here, S is the area of the nanowire cross section. Torsional motions satisfy conditions of continuity on angle of twist, θ, and total torque, $J\frac{\partial \theta}{\partial x}$, at each interface. Flexural motions satisfy conditions of continuity on displacement, u_y or u_z, bending angle, $\phi = \frac{\partial u_{y/z}}{\partial x}$, total bending moment, $L = -EI_{yy/zz}\frac{\partial^2 u_{y/z}}{\partial x^2}$,and total shear force, $V = EI_{yy/zz}\frac{\partial^3 u_{y/z}}{\partial x^3}$, at each interface. The y and z subscripts associated with the interface conditions for the flexural modes are associated with the two orthogonal bending directions, y or z. Using these

conditions of continuity yields linear relations for the amplitudes of forward, A_ξ^+, and negative, A_ξ^-, traveling modes in each nanowire section adjacent to a given interface:

$$\left[M_\xi\right]\left\{A_\xi\right\}=\left[M_{\xi+1}\right]\left\{A_{\xi+1}\right\} \tag{47}$$

For the extensional and torsional modes, the amplitude vector is defined by $\left\{A_{\xi,ex/tor}\right\}=\left\{A_\xi^+ \quad A_\xi^-\right\}^T$. For the flexural modes, the amplitude vector is defined by $\left\{A_\xi\right\}=\left\{A_\xi^+ \quad A_\xi^- \quad A_\xi^{+,e} \quad A_\xi^{-,e}\right\}^T$. $A_\xi^{+,e}$ and $A_\xi^{-,e}$ refer to the amplitudes of the forward and backward traveling evanescent flexural waves associated with wavenumbers that are purely complex. In Eq. (47) the amplitudes are evaluated at the $\xi,\xi+1$ interface.

The modal amplitudes for the first and last nanowire sections may be related by:

$$\left[M^{tot}\right]\left\{A_1\right\}=\left\{A_{N+1}\right\} \tag{48}$$

where the total transmission matrix, $\left[M^{tot}\right]$, can be computed through a cascading multiplication of the matrices that correspond to each section,

$$M^{tot}=\prod_{\xi=1}^{N}\left[M_{\xi+1}\right]^{-1}\left[M_\xi\right]\left[\Omega_\xi\right] \tag{49}$$

The interface matrices, $\left[M_\xi\right]$, associated with each mode type are listed in Table 5.2. The interface matrices are obtained by substituting the solutions (Table 5.1) into the interface conditions (Table 5.2) and assuming x=0 at the interface. Note that this cascading matrix approach is similar in spirit to the cascaded "T-parameter" approach

that is applicable in the analysis of 2-port cascaded electrical networks [98]. This can be done since the displacements at the left side of a given nanowire section are related to the displacements at the right side of the same section by multiplying the amplitude by a phase factor matrix, $\left[\Omega_{\xi}\right]$, defined as follows for extensional or torsional modes, and flexural modes, respectively.

$$\left[\Omega_{\xi,ext/tor}\right]=\begin{bmatrix}\exp\left(-ik_{\xi}d_{\xi}\right) & 0\\ 0 & \exp\left(ik_{\xi}d_{\xi}\right)\end{bmatrix} \tag{50}$$

$$\left[\Omega_{\xi,flex}\right]=\begin{bmatrix}\exp\left(-ik_{\xi}d_{\xi}\right) & 0 & 0 & 0\\ 0 & \exp\left(ik_{\xi}d_{\xi}\right) & 0 & 0\\ 0 & 0 & \exp\left(-k_{\xi}d_{\xi}\right) & 0\\ 0 & 0 & 0 & \exp\left(k_{\xi}d_{\xi}\right)\end{bmatrix} \tag{51}$$

Noting that $A_{N+1}^{-}=0$ and assuming that $A_{1}^{+}=1$, the amplitudes of the transmitted mode for the *N+1* region may be found for the extensional or torsional case from the elements of the total transmission matrix and the simple relation:

$$A_{N+1}^{+,ext/tor}=M_{11}^{tot}-\frac{M_{12}^{tot}M_{21}^{tot}}{M_{22}^{tot}} \tag{52}$$

For the flexural case, the unknown amplitudes, including the transmitted amplitude may be found by solving the linear system that relates the reflected amplitudes in section 1 and transmitted amplitudes in section *N+1* with the elements of the total transmission matrix:

$$\begin{bmatrix} M_{12}^{tot} & M_{14}^{tot} & -1 & 0 \\ M_{22}^{tot} & M_{24}^{tot} & 0 & 0 \\ M_{32}^{tot} & M_{34}^{tot} & 0 & -1 \\ M_{42}^{tot} & M_{44}^{tot} & 0 & 0 \end{bmatrix} \begin{Bmatrix} A_1^- \\ A_1^{-,e} \\ A_{N+1}^+ \\ A_{N+1}^{+,e} \end{Bmatrix} = \begin{Bmatrix} -M_{11}^{tot} \\ -M_{21}^{tot} \\ -M_{31}^{tot} \\ -M_{41}^{tot} \end{Bmatrix} \tag{53}$$

In order to derive Eq. (53) it is noted that $A_{N+1}^{-,e} = A_1^{+,e} = 0$. Once the transmitted amplitudes, A_{N+1}^+, are computed, they may be used to calculate the transmission from the ratio of the transmitted to incident time-averaged acoustic power flow:

$$\alpha = \frac{P_{x,N+1}}{P_{x,1}} \tag{54}$$

The time-averaged acoustic power flow, $P_{x,\xi}$, for each nanowire region is unique for each mode type. For the extensional and torsion modes it may be easily derived via integration of the x-component of the acoustic Poynting vector over the nanowire region cross-section [99]:

$$P_{x,\xi} = -\frac{1}{2}\int_S \dot{\mathbf{u}}_\xi^* \cdot \boldsymbol{\sigma}_\xi \cdot \hat{\mathbf{x}} dS \tag{55}$$

Here, $\dot{\mathbf{u}}_\xi^*$ is the complex conjugate of the velocity field of a nanowire region, ξ, and $\boldsymbol{\sigma}_\xi$ is the stress tensor field of a nanowire region, ξ. For long wavelength extensional motions, there is only an axial component of velocity and a normal component of stress, $\sigma_{xx,\xi} = E\frac{\partial u_{x,\xi}}{\partial x}$, so that the power flow may be evaluated from:

$$P_{x,\xi}^{ext} = -\dot{u}_{x,\xi}^* \sigma_{xx,\xi} S \tag{56}$$

For the torsional mode, there are two non-zero components of shear stress so that the power flow may evaluated from:

$$P_{x,\xi}^{tor} = \int \dot{u}_{z,\xi}^{*}\sigma_{xz,\xi} + \dot{u}_{y,\xi}^{*}\sigma_{xy,\xi}\, dS \tag{57}$$

The components of shear stress, $\sigma_{xz,\xi}$ and $\sigma_{xy,\xi}$, associated with the torsional mode must be evaluated from the Prandtl stress function and related to the torsional rigidity and angle of twist following the torsion analysis presented, for example, in Ref. [96]. For the flexural modes, the power flow is more easily obtained from [100]:

$$P_{x,\xi}^{flex} = \frac{1}{2} V_{\xi} \dot{u}_{y/z,\xi}^{*} + \frac{1}{2} L_{\xi} \dot{\phi}_{\xi}^{*} \tag{58}$$

The appropriate harmonic fields can be substituted into Eqs. (56), (57), and (58) to obtain simplified expressions for the time averaged power flow in each region according to mode type. These simplified results are listed in the fourth column of Table 5.2.

Table 5.1: Governing equations, general solutions for each region, and dispersion relations associated with each zeroth-order mode type.

Mode Type	Governing Equation	Solution for each region	Dispersion Relation
Extensional	$\frac{E}{\rho}\frac{\partial^2 u_x}{\partial x^2} = \frac{\partial^2 u_x}{\partial t^2}$	$u_{x,\xi} = A_{\xi}^{+}\exp\left(i\left(\omega t - k_{\xi}x\right)\right) + A_{\xi}^{-}\exp\left(i\left(\omega t + k_{\xi}x\right)\right)$	$\omega_{ext} = \sqrt{\frac{E}{\rho}}k$
Torsional	$\frac{J}{\rho I_P}\frac{\partial^2 \theta}{\partial x^2} = \frac{\partial^2 \theta}{\partial t^2}$	$\theta_{\xi} = A_{\xi}^{+}\exp\left(i\left(\omega t - k_{\xi}x\right)\right) + A_{\xi}^{-}\exp\left(i\left(\omega t + k_{\xi}x\right)\right)$	$\omega_{tor} = \sqrt{\frac{J}{I_P\rho}}k$
Flexural	$\frac{EI}{\rho S}\frac{\partial^4 u_{y/z}}{\partial x^4} = \frac{\partial^2 u_{y/z}}{\partial t^2}$	$u_{y/z,\xi} = A_{\xi}^{+}\exp\left(i\left(\omega t - k_{\xi}x\right)\right) + A_{\xi}^{-}\exp\left(i\left(\omega t + k_{\xi}x\right)\right)$ $+A_{\xi}^{+,e}\exp\left(i\omega t - k_{\xi}x\right) + A_{\xi}^{-,e}\exp\left(i\omega t + k_{\xi}x\right)$	$\omega_{flex} = \sqrt{\frac{EI}{\rho S}}k^2$

Table 5.2: Interface conditions, interface matrices, and integrated power flow associated with each mode type. Prime indicates neighboring section.

Mode Type	Interface Conditions	$\left[M_\xi\right]$	$P_{x,\xi}$
Extensional	$u_{x,\xi} = u_{x,\xi'}$ $S_\xi E_\xi \frac{\partial u_{x,\xi}}{\partial x} = S_{\xi'} E_{\xi'} \frac{\partial u_{x,\xi'}}{\partial x}$	$\begin{bmatrix} 1 & 1 \\ -ik_\xi E_\xi S_\xi & ik_\xi E_\xi S_\xi \end{bmatrix}$	$\frac{1}{2}\omega k_\xi S_\xi E_\xi \left\|A_\xi^+\right\|^2$
Torsional	$\theta_\xi = \theta_{\xi'}$ $J_\xi \frac{\partial \theta_\xi}{\partial x} = J_{\xi'} \frac{\partial \theta_{\xi'}}{\partial x}$	$\begin{bmatrix} 1 & 1 \\ -ik_\xi J_\xi & ik_\xi J_\xi \end{bmatrix}$	$\frac{1}{2}\omega k_\xi J_\xi \left\|A_\xi^+\right\|^2$
Flexural	$u_{y/z,\xi} = u_{y/z,\xi'}$ $\frac{\partial u_{y/z,\xi}}{\partial x} = \frac{\partial u_{y/z,\xi'}}{\partial x}$ $E_\xi I_\xi \frac{\partial^2 u_{y/z,\xi}}{\partial x^2} = E_{\xi'} I_{\xi'} \frac{\partial^2 u_{y/z,\xi'}}{\partial x^2}$ $E_\xi I_\xi \frac{\partial^3 u_{y/z,\xi}}{\partial x^3} = E_{\xi'} I_{\xi'} \frac{\partial^3 u_{y/z,\xi'}}{\partial x^3}$	$\begin{bmatrix} 1 & 1 & 1 & 1 \\ -ik_\xi & ik_\xi & -k_\xi & k_\xi \\ -k_\xi^2 E_\xi I_\xi & -k_\xi^2 E_\xi I_\xi & k_\xi^2 E_\xi I_\xi & k_\xi^2 E_\xi I_\xi \\ ik_\xi^3 E_\xi I_\xi & -ik_\xi^3 E_\xi I_\xi & -k_\xi^3 E_\xi I_\xi & k_\xi^3 E_\xi I_\xi \end{bmatrix}$	$\omega k_\xi^3 E_\xi I_\xi \left\|A_\xi^+\right\|^2$

The analytical technique as described thus far is general. The nanowire may be comprised of many different regions each of which may have a different length, constituent material, or cross-section. For such nanowires, implementation of this technique requires some numerical effort. For nanowires of reduced geometrical and material complexity, it is expedient to apply simplified analytical expressions. Such expressions have been derived for a single nanowire interface and a symmetric double interface. These geometries represent, respectively, a coaxial nanowire stepped junction and a nanowire with a single coaxial constricted or expanded section (Figure 5.2). Analytical transmission coefficient expressions for these geometries are listed in Table 5.3. These cases allow for the cross-section size, shape, and material properties to differ between nanowire regions I and II. For the case of the single interface, the simple model

predicts a phonon transmission coefficient that is independent of incident wavenumber and depends only on the size, shape, and material properties of regions *I* and *II*. For the symmetric double interface, the analytical expression for extensional and torsional phonon transmission coefficient has additional dependence on the product of the incident phonon wavenumber, *k*, the region length, *d*, and a few geometrical and material property parameters and is similar in functional form to acoustic wave transmission through a simple, single element, low-pass filter [101].

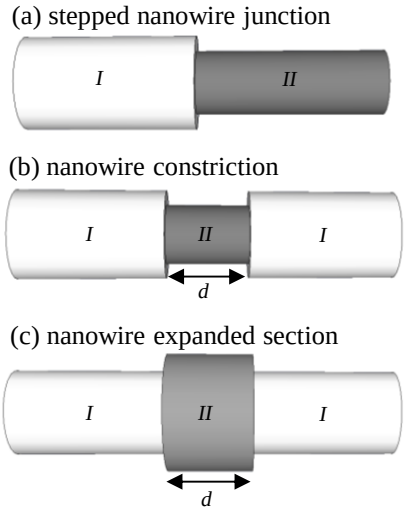

Figure 5.2: Simple nanowire geometries.

Table 5.3: Transmission results for single interface (nanowire step) or symmetric double interface

Mode Type	γ	Nanowire Stepped Junction	Nanowire Constriction or Expansion
Extensional	$\sqrt{\frac{E_I \rho_{II}}{E_{II} \rho_I}}$	$\frac{4\left(\gamma \frac{E_{II} S_{II}}{E_I S_I}\right)}{\left(\frac{\gamma E_{II} S_{II}}{E_I S_I} + 1\right)^2}$	$\frac{4}{4\cos^2(\gamma kd) + \left(\frac{\gamma_{ext} E_{II} S_{II}}{E_I S_I} + \frac{E_I S_I}{\gamma_{ext} E_{II} S_{II}}\right)^2 \sin^2(\gamma kd)}$
Torsional	$\sqrt{\frac{J_I I_{P,II} \rho_{II}}{J_{II} I_{P,I} \rho_I}}$	$\frac{4\gamma \frac{J_{II}}{J_I}}{\left(\gamma \frac{J_{II}}{J_I} + 1\right)^2}$	$\frac{4}{4\cos^2(\gamma\, kd) + \left(\frac{\gamma J_{II}}{J_I} + \frac{J_I}{\gamma J_{II}}\right)^2 \sin^2(\gamma kd)}$
Flexural	$\left(\frac{E_I I_I \rho_{II} S_{II}}{E_{II} I_{II} \rho_I S_I}\right)^{1/4}$	$\frac{4\left(\gamma^3 \frac{E_{II} I_{II}}{E_I I_I} + \gamma^2 \frac{E_{II} I_{II}}{E_I I_I} + \gamma + 1\right)^2 \gamma \frac{E_{II} I_{II}}{E_I I_I}}{\left(\gamma^4 \left(\frac{E_{II} I_{II}}{E_I I_I}\right)^2 + 2\gamma^3 \frac{E_{II} I_{II}}{E_I I_I} + 2\gamma^2 \frac{E_{II} I_{II}}{E_I I_I} + 2\gamma \frac{E_{II} I_{II}}{E_I I_I} + 1\right)^2}$	No reduced form found. Use general treatment from section 5.2.3.

If the model is restricted further such that each nanowire region has square or circular cross-section and differs only in size so that the cross-section shape and material remain constant, further simplified expressions can be obtained. In these cases, the phonon transmission depends only the size ratio and the product of the incident phonon wavenumber, k, and the region length, d. For nanowires with square cross section, $\beta = \frac{h_{II}}{h_I}$. For nanowires with circular cross section, $\beta = \frac{D_{II}}{D_I}$. For the cylindrical nanowire, D_I and D_{II} are the diameters of the first and second regions, respectively. For the nanowire with square cross section, h_I and h_{II}, are the side lengths of the first and

second regions, respectively. The analytical transmission results for these simple geometries are tabulated in Table 5.4.

Table 5.4: Analytical results for cases of constant material property nanowires with circular or square cross section.

Mode Type	Nanowire Stepped Junction	Nanowire Constriction or Expansion
Extensional	$\frac{4\beta^2}{\left(\beta^2+1\right)^2}$	$\frac{4}{4\cos^2(kd)+\left(\beta^2+\frac{1}{\beta^2}\right)^2\sin^2(kd)}$
Torsional	$\frac{4\beta^4}{\left(\beta^4+1\right)^2}$	$\frac{4}{4\cos^2(kd)+\left(\beta^4+\frac{1}{\beta^4}\right)^2\sin^2(kd)}$
Flexural	$\frac{4\left(\beta^{5/2}+\beta^3+\beta^{-1/2}+1\right)^2\beta^{7/2}}{\left(\beta^6+2\beta^{5/2}+2\beta^3+2\beta^{7/2}+1\right)^2}$	No reduced form found. Use general treatment from section 5.2.3.

5.3 Comparison of Simple and Atomistic Models

5.3.1 *Atomistic System Configuration*

In order to assess the range of applicability of the model, it is compared with an atomistic computational model that, in contrast to the simple analytical model, accounts for mode conversion, the existence of higher order evanescent modes, crystal orientation, and atomistic granularity associated with discretely distributed particles. The atomistic calculations are based on the lattice dynamics - scattering boundary method (LD-SBM)

approach that is described in Chapter 4. The goal of these comparisons is to illustrate sources of deviation between the two models and delineate the regime of validity for the simple analytical model. The comparison is performed for the test case of a stepped cylindrical nanowire and a cylindrical nanowire with a single constriction. Interatomic forces were modeled using the linearized Stillinger-Weber potential.

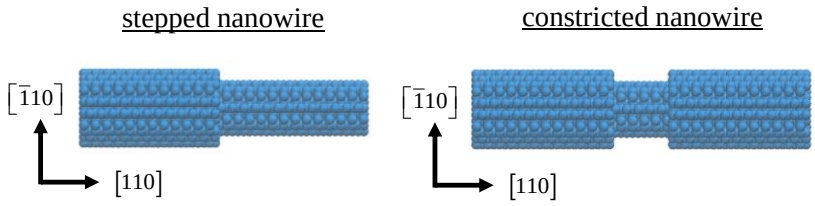

Figure 5.3: Configuration of atomistic systems used in comparison.

5.3.2 *Model Comparison for Stepped Nanowire*

In Figure 5.4 the SBM results are compared with the simple model for a stepped cylindrical nanowire. As predicted by the simple model, phonon transmission is constant at small wavenumbers and the two models agree very well in that regime. At higher wavenumbers, the agreement is not as good. At first, a gradual deviation is observed for all of the modes. At kD_I near 3 a sharp discontinuity is observed in the transmission for the extensional mode. As evidence by the two different sizes plotted in Figure 5.4(a) and (b), these trends are common for all system sizes and size ratios, and the deviations between the models occur at very similar values of kD_I independent of the size ratio β or the incident region diameter D_I. The atomistically calculated transmission curves of the y and z flexural modes match each other and agree with the simple model for small

wavenumbers. However, they diverge from each other and the simple model at higher wave numbers. This divergence is associated with the fact that the bending in the y-direction is aligned with the $[\bar{1}10]$ crystal axis, whereas bending in the z-direction is aligned with the $[001]$ crystal axis. This inherent asymmetry is not included in the simple model. The agreement between the atomistic model and the simple model is best for the torsional mode and deviations between models, in the wavenumber ranged sampled, are small and occur at higher wavenumbers.

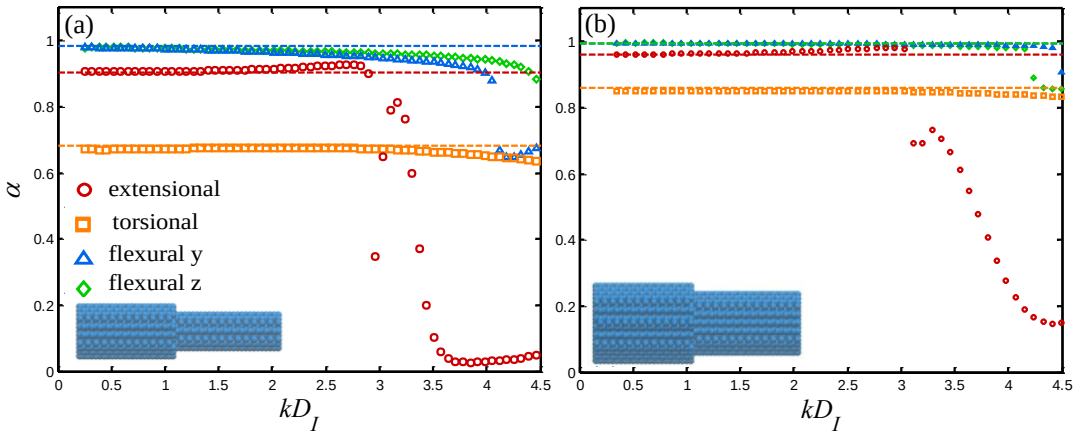

Figure 5.4: Comparison of atomistic and simple models for case of stepped nanowire system. Dashed lines correspond to simple model results and markers correspond to atomistic results. Color and mode types are indicated in the legend. D_I= 2.37 nm and β=0.73, (b) corresponds to D_I= 3.625 nm and β=0.82.

5.3.3 *Origin of Deviation Between Models*

The origin of the deviations between the models can be attributed to several assumptions in the simple model that fail to match the true mechanics of the nanowire scattering system, as calculated using the SBM.

5.3.3.1 Mode Shape Effects

The first assumption responsible for deviations between the two models is the assumption of simple, one-dimensional mode shapes. While the assumed mode shapes are valid at low wavenumbers, the actual mode shapes gradually diverge from the long wavelength model (Figure 5.5) as wavenumber increases. Note that both the real and imaginary components of the mode shapes are plotted since in-plane and out-of plane motions can sometimes be out of phase with other, but both are important characteristics of the modes. The most severe deviation from the assumed simple model is exhibited by the extensional mode. Rather than being constant across the cross-section, the atomic motions associated with the extensional mode begin to vary across the cross-section at wavenumbers around kD=1.5. This trend continues for higher wavenumbers and is accompanied by a significant amount of displacement in the plane of the cross-section: an appreciable amount of non-axial displacement arises at wavenumbers around kD=2.5. The characteristic motion of the extensional mode at higher wavenumber is a contraction of the nanowire along one direction that occurs simultaneously with an expansion in the direction perpendicular to the contraction. The directions of maximum contraction and

expansion are aligned with the crystal axes of the nanowire. Because the nanowire is anisotropic, this behavior is different than the behavior of the zeroth-order extensional mode of an isotropic cylindrical nanowire which exhibits axially symmetric expansion and contraction at higher wavenumbers [94]. The atomic motions associated with the flexural modes transition from being purely perpendicular to the neutral plane to having motions along the nanowire axis. The amount of axial displacement increases with wavenumber until the maximum is attained at wavenumbers around *kD=2.5.* At wavenumbers higher than *kD*=2.5, the calculations show that the mode shapes of the flexural modes change very little. For the torsional modes, little deviation from the assumed mode shape model is observed and the actual calculated atomic displacements in the range of wavenumber considered. This is consistent with 3-D elastic theory which predicts no warping of cylindrical beams under torsion [102].

A simple way to characterize the deviation of the atomistic mode shapes from those of the assumed long wavelength model is through the introduction of the deviation parameter, ψ, which is defined for the different mode types as:

$$\begin{aligned} \psi_{ext} &= \sum_i \left(\tilde{u}_{y,i}^2 + \tilde{u}_{z,i}^2 \right) \\ \psi_{tor,\,flex} &= 1 - \sum_i \left(\tilde{u}_{y,i}^2 + \tilde{u}_{z,i}^2 \right) \end{aligned} \tag{59}$$

In the case that the dominant direction of the atomic displacements matches the assumed model, ψ is equal to zero. ψ is plotted versus dimensionless wavenumber kD_I in Figure 5.6. This plot shows that ψ deviates away from zero most rapidly for the

extensional mode. The transition from having most of the displacement associated with the extensional mode along the axial direction to having the majority of the displacement in the plane of the nanowire cross-section occurs at dimensionless wavenumbers, kD_I, around 2.5. A similar, but less severe, trend is also calculated for the two flexural modes. As shown in Figure 5.6, the shape of ψ curve as a function of scaled wavenumber is not dependent on the size of the nanowire for nanowires greater than 3 nm in diameter. This suggests that the regime transition associated with mode shape effects can be predicted to occur at the same value of kD_I, independent of D_I. The increases calculated in ψ are well correlated with the deviation between transmission models for the extensional and flexural modes and it is believed that the deviations between mode shape models are a primary reason the simple model loses validity for the treatment of extensional and flexural modes at higher wavenumbers.

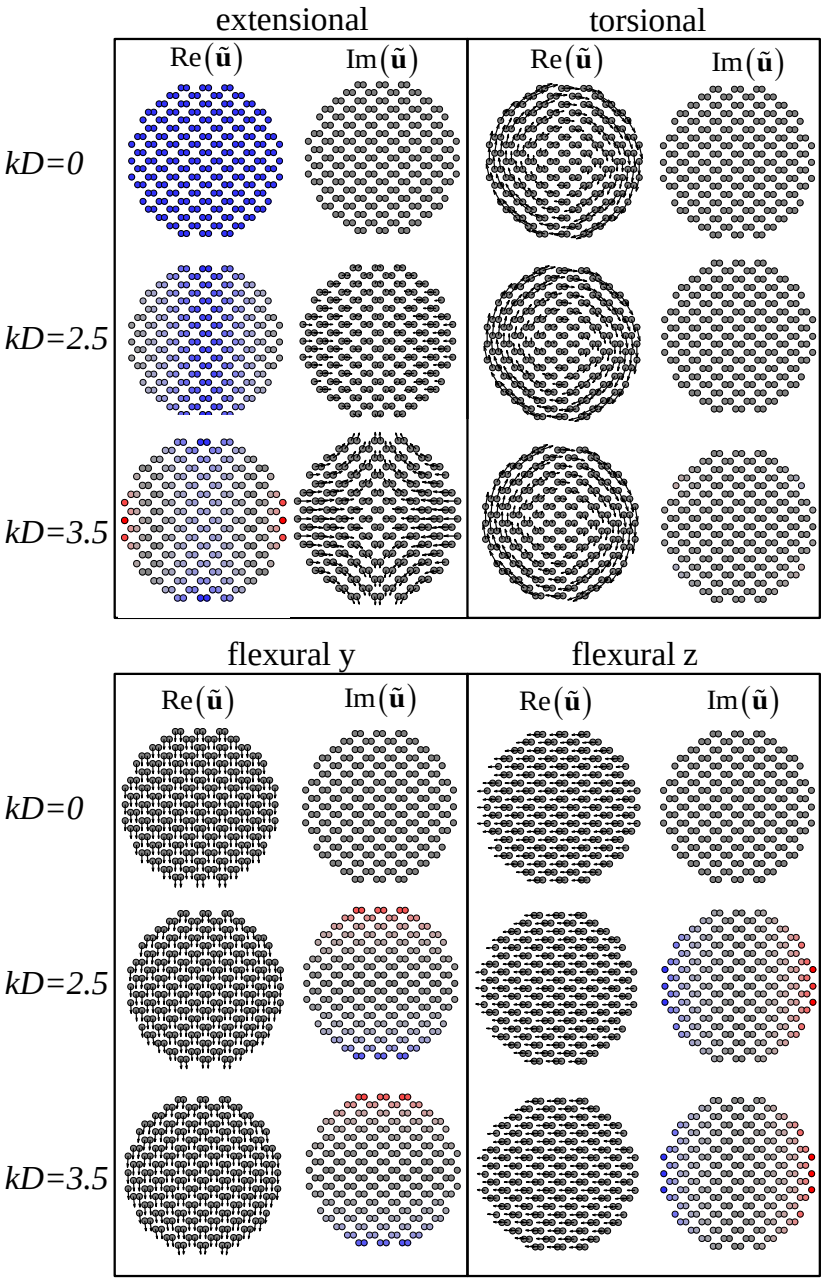

Figure 5.5: Dependence of mode shapes on wavenumber. Diameter of nanowire shown in figure is 3.71 nm. Color indicates amount of axial displacement (red is positive and blue is negative). Arrows indicate direction and relative magnitude of displacement in the plane of the nanowire cross-section. In the simple model, atomic displacements are uniform across the cross section for the extensional and flexural modes and vary linearly with radius for torsional modes in a cylinder.

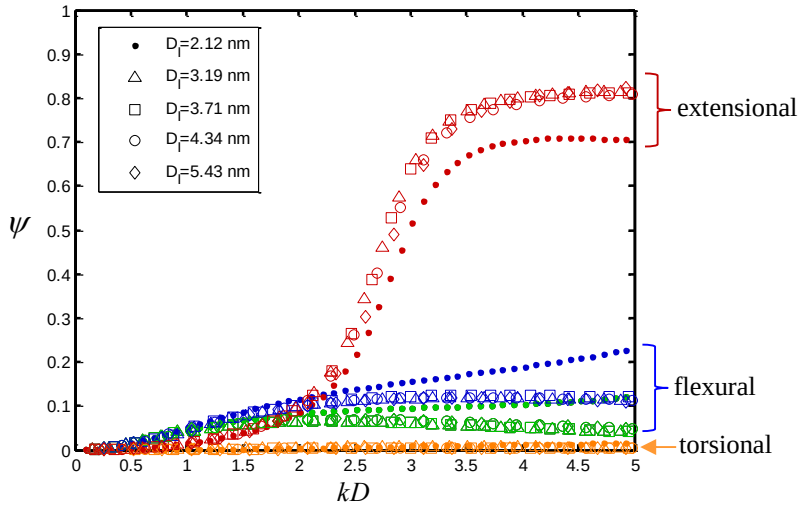

Figure 5.6: Plot of deviation parameter as a function of *kD* for different nanowire sizes. Marker shapes indicate the size of the nanowire as indicated in the legend. Marker colors indicate mode type: red corresponds to extensional, orange corresponds to torsional, and blue and green correspond to the two flexural modes.

5.3.3.2 Higher Order Modes and Mode Conversion

The next source of deviation between the two models is associated with the fact that the simple model does not include the role of higher order modes in determining phonon transmission. Higher order modes are modes with nonzero cutoff frequency. In addition, the simple model does not allow for mode conversion at the nanowire interfaces. This means that in the simple model, energy in an incident mode of one type will not be transferred into reflected or transmitted energy of another type. In contrast, the scattering boundary calculations include the possibility of mode conversion and the participation of higher order modes. Higher order modes can affect the transmission calculation in one of two ways. Above their cutoff frequency, they can propagate and

carry transmitted or reflected energy away from the interface. Or, if the frequency is below their cutoff frequency, higher order modes will have complex wavenumbers and their associated displacements decay exponentially away from the nanostructure interface. These are evanescent modes, and while they don't carry energy, they can have nonzero amplitudes and contribute to the solution of the scattering boundary equations and equations of motion in the nanowire scattering system. The scattering boundary calculations have shown that at low wavenumbers if the nanowire sections are coaxial with each other, interaction with higher order modes and mode conversion effects are negligible in the long wavelength limit. As the wavenumber is increased, interactions with modes other than the incident mode begin to influence the transmission calculation, and are partly responsible for the gradual deviation between the models at wavenumbers less than kD=2.5. Higher order modes affect transmission more strongly when the incident phonon frequency is above the cutoff frequency of a higher order mode. This effect is strongly associated with the sharp discontinuity in the transmission of the extensional mode at wavenumbers near kD_I=3. An example of mode conversion and interaction with higher order modes is given in Figure 5.7 which plots the percent transmitted amplitude of non-extensional modes versus kD_I for the extensional mode incident in stepped nanowire. At low wavenumbers, all of the transmitted amplitude is in the extensional mode. As the wavenumber is increased, the fraction of amplitude associated with other modes gradually increases. At $kD_I \approx 2.5$, there is a sharp increase in the amount of amplitude in other modes. This increase coincides with the activation of

propagating higher order modes in the incident side region. Higher order mode effects and differences in mode shapes between the two models occur simultaneously. As such, it is not possible to precisely attribute deviations in the transmission models to one effect or the other. In fact, participation of other modes may be required, in part, because of the wavenumber dependence of each region's mode shapes. As mode shapes deviate from their simple, 1-D, long wavelength forms, participation of other modes is required in order to match the more complicated displacement fields associated with incident phonons.

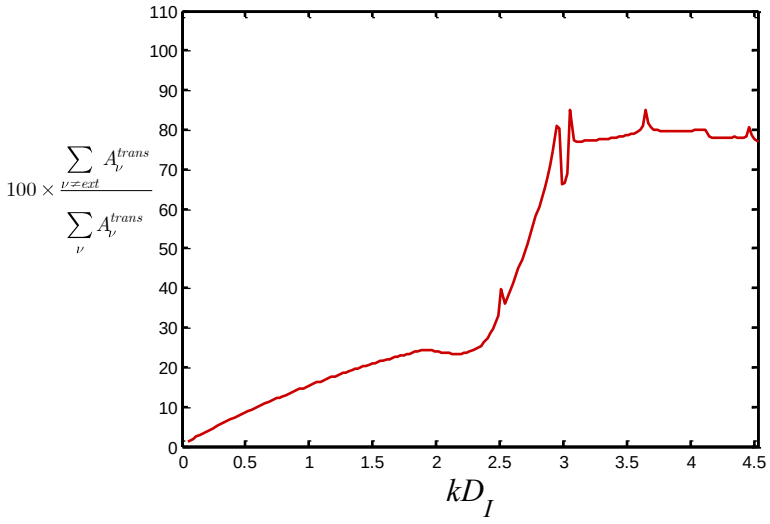

Figure 5.7: Percent transmitted amplitude in modes other than extensional mode. Incident mode is extensional. D_I=2.37 nm and β=0.73.

5.3.3.3 Atomistic Effects

The third source of deviations arises from the discrete nature of the scattering boundary calculations. These are denoted atomistic effects. Atomistic effects are

differentiated from the other sources of discrepancy in that the other sources could be overcome through the use of a more general continuum elastic model that is based upon analytic or computational solution of continuum elastic governing equations. For example, methods based upon finite element solution of governing equations, provide an avenue to explore the full 3-D elastic-anisotropic aspects of the problem and therefore model mode shapes more accurately. In addition, these methods allow for interaction with higher order modes and mode conversion. However, such an approach would not include effects associated with the discrete distribution of atoms in the nanowire. Atomistic effects may be understood as being dependent upon how the length scale of the discreteness (the lattice parameter) compares with the relevant length scales of the nanowire geometry (the nanowire diameter) and the phonon (the phonon wavelength, or, alternatively, the wavenumber). Atomistic effects associated with the phonon wavelength are considered first. If the phonon wavelength is comparable to the lattice parameter, one would expect the atomistic nature of the problem to affect the transmission results. This effect was investigated in Chapter 4 for the simpler case of shear-horizontal phonon propagation at stepped plate interfaces and it was found that at wavenumbers higher than $ka \approx 0.50$, wavelength dependent atomistic effects can be prominent. However, for the practically relevant case of nanowires with diameter greater than 5 nm, the transition to the wavelength dependent atomistic regime occurs at wavenumbers greater than those where the previously described mode shape and higher order mode effects are already prominent. As such, except in the smallest nanowire

cases, wavelength dependent atomistic effects should not be viewed as a primary cause for deviations between the SBM results and the simple long wavelength model. On the other hand, in the long wavelength limit, atomistic effects that are size dependent are observed. These atomistic effects are responsible for any disagreement between the models at low wavenumbers. For the cases shown in Fig. 5, the disagreement between models is less than 2%. For other cases tested (different nanowire sizes and different values of β) the degree of disagreement can sometimes be larger. The long wavelength discrepancy between the models arises from the fact that atoms are distributed on a discrete lattice. This causes the nanowire boundary in the atomistic model to be inherently rough and because of the rectilinear nature of the diamond lattice the cross-section shape will not be exactly circular. The discrete nature also leads to some ambiguity in measuring the diameters of regions I and II, which in turn leads to uncertainty in the β parameter. Though other definitions are possible, the nanowire radius is defined to be the average distance from the nanowire center to the centers of the two outermost boundary atoms. Another atomistic effect that also limits the applicability of the simple model is that as the nanowire is made smaller, a higher fraction of the atoms in the nanowire cross-section are near or at the nanowire boundary. Because the boundary is free, atoms near or at the boundary experience forces that are different than those closer to the nanowire center. As result, the elastic stiffness will vary across the nanowire cross-section and the overall effective material properties (e.g. Young's modulus and shear modulus) will differ between nanowires of different sizes.

As the nanowire is made larger, the stiffness properties of the nanowire approach that of bulk, and this atomistic effect is be minimized. All of these factors are minimized as the size of the nanowire system is made larger. In Figure 5.8 the percent difference in transmission between the atomistic and simple models for long wavelength modes is plotted versus system size while the size ratio was held within a prescribed range. The figure demonstrates that the deviation between models, in general, gets smaller for larger system sizes. Long wavelength atomistic effects on geometry induced phonon scattering have been explored in more detail in Chapter 4.

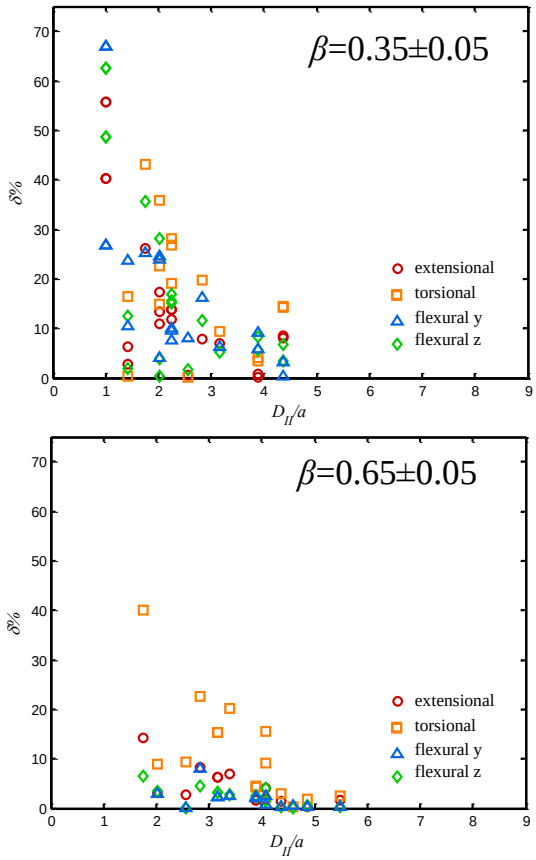

Figure 5.8: Percent difference in transmission between models as a function of size for stepped nanowire case. Since diameter cannot be continuously defined in the atomistic calculations, β is held within the ranges indicated in each plot so that comparable size ratios for nanowires of different sizes may be compared.

5.3.4 *Constricted Nanowire Results*

In Figure 5.9 the SBM results are compared with the simple model for a constricted nanowire case. For this case, unlike the stepped nanowire case, the simple model predicts wavenumber dependent transmission. In this comparison the nanowire size as well as the size ratio are held constant and three different values of the constriction length *d* were investigated. As was the case with the stepped nanowire case, the two

models agree very well for small wavenumbers. The regime of agreement is similar to the stepped nanowire case with the shapes of the transmission curves agreeing qualitatively to wavenumbers up to kD=2.5. However, the gradual disagreement that was observed for the stepped nanowire case is augmented for the constricted case since the transmission curves vary rapidly. This effect is more prominent as d is increased which in turn decreases the period of oscillation in the both the simple model and SBM transmission curves. The peaks and valleys in transmission are caused by reflection from the interfaces between the constricted and non-constricted sections. The oscillation period decreases for a longer d since there are more opportunities for constructive and destructive interference over the range of wavelengths sampled. This comparison demonstrates that while the simple model can be expected to agree qualitatively with the SBM model for wavenumbers up to kD_I=2.5, close numerical agreement can only be expected for kD_I<0.50.

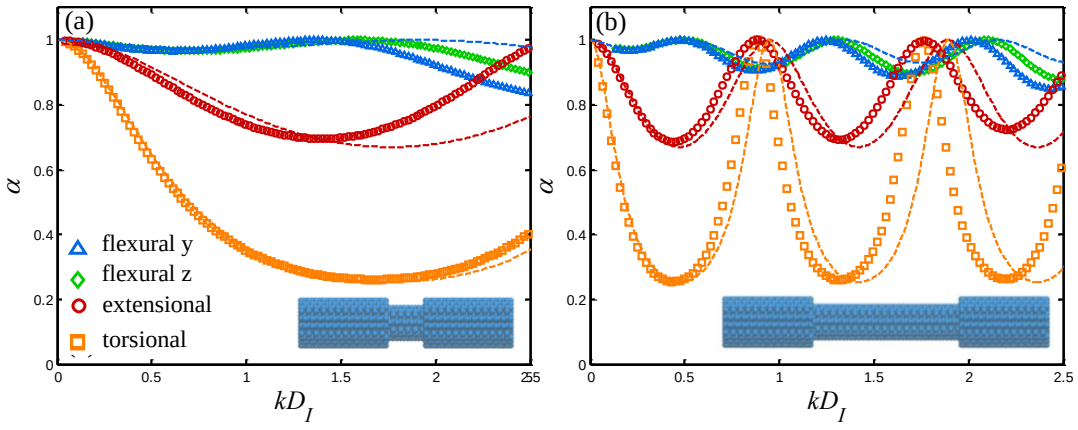

Figure 5.9: Comparison of atomistic and simple model transmission results for case of constricted nanowire system. Dashed lines correspond to simple model results and markers correspond to atomistic results. Color and mode types are indicated in the legend. DI= 2.37 nm and β=0.73 for (a)(b). (a) corresponds to d= 2.99 nm and (b) corresponds to d=11.13nm.

In addition to the case-study calculations presented herein, and in order to obtain generally applicable regime boundaries for the model, an expansive sampling of the parameter space was also performed (hundreds of calculations spanning a wide range of β, D_I, D_{II}, and k) for the stepped nanowire geometry. Through these calculations it was found that the deviation between the atomistic and simple models is no more than 10% for all four modes for kD<2.5 and D/a>4.5. These endpoints are recommended as conservative regime boundaries for accurate application of the simple model. Note that wavenumber regime (defined by kD) is limited by the *largest* diameter in the nanowire and the size limit (defined by D/a) is limited by the *smallest* diameter in the nanowire. Since the fundamental assumptions of the simple model are the same for the nanowire

step as they are for a nanowire comprised of an arbitrary number of nanowire regions, similar regime boundaries are recommended for the general geometric case if only qualitative agreement is required. For cases where the transmission varies rapidly with wavenumber (i.e. in the constricted nanowire case), close quantitative numerical agreement should only be expected up to kD=0.50.

5.4 Conclusions

This chapter described a simple analytical model for estimating ballistic transmission rates of guided phonons in nanowires with abrupt geometric and material discontinuities. The model includes separate consideration of the zeroth order extensional, torsional, and flexural modes and is based upon the long wavelength behavior of these modes as analyzed using continuum elastic wave theory of prismatic beams. The model is presented using a cascading approach that is similar to methods used in the analysis of electrical networks and may be applied to a nanowire system with any number of discontinuities and arbitrary but piecewise constant cross-section. In addition to the general cascading matrix approach, simplified analytical expressions were presented for the cases of the single nanowire stepped junction and nanowire with coaxial constriction or expansion. For the test case of a cylindrical silicon nanowire system, the results of the analytical analytical model are compared with modal transmission rates calculated using the lattice dynamics – scattering boundary method model (LD-SBM) which was described in Chapters 2 and 3. In contrast to the simple analytical model, the

LD-SBM model accounts for mode conversion, interactions with higher order evanescent modes, crystal orientation, and atomistic granularity associated with discretely distributed particles. For the cases studied, the comparison with the atomistic model illustrated that the analytical model can be applied with good quantitative agreement for scaled wavenumbers less than kD=0.50 and qualitative agreement for scaled wavenumbers less than kD=2.5. Since the simple model greatly simplifies the true mechanics of the nanowire scattering system, it does not agree with the atomistic model at higher wavenumbers. Boundary related atomistic effects also limit the accuracy of the simple model for very small nanowire systems. Nevertheless, the model provides a good first approximation in the analysis of geometry induced phonon scattering in nanowire systems.

6 Phonon Transmission and Ballistic Thermal Conductance in Diameter Modulated Silicon Nanowires

6.1 Chapter Overview and Scope:

The previous chapters of this dissertation described the theory, implementation, and verification of a harmonic lattice dynamics –scattering boundary method (LD-SBM) computational approach to modeling phonon spectra and calculating phonon transmission in geometrically irregular nanostructures. In Chapters 4 and 5 the model was used to calculate phonon transmission coefficients in some simple plate and nanowire geometries. In those chapters the LD-SBM model was only used to evaluate the accuracy and regimes of applicability of alternative modeling approaches. Additionally, the transmission coefficients of only a few select phonon modes were considered in those chapters. In this chapter, a more expansive use of the model is employed in order to address the overall goal of this dissertation: predicting and analyzing the effect of nanostructure geometry on thermal transport.

Inspired by the well-behaved transmission behavior predicted by the simple model developed in Chapter 5, this chapter is concerned with ballistic phonon transmission and thermal conductance between two semi-infinite straight cylindrical silicon nanowire sections (referred to as nanowire leads) through a silicon nanowire section with an

irregular geometry created by locally increasing or decreasing the diameter. This geometry is referred to as a diameter modulated silicon nanowire. This geometry type can be viewed as an abstraction or simplification of the notched nanowires [12], spheroid nanowires [16], or periodically dilated nanowires [17] that have been synthesized in the laboratory by previous researchers. The modulated nanowire geometry is characterized by four parameters: the diameter of the left and right straight nanowire leads, D_I, the diameter of the modulation, D_{II}, the length of the modulation, d, and the number of modulations, N. In this study, the parameter space for the multiple modulation case is restricted by holding the diameter of each successive modulation constant at the reference modulation diameter, D_{II}. The diameter of the sections between each modulation is held constant and equal to the diameter of the nanowire leads, D_I. Furthermore, the length of each modulation, d, is also held constant for successive modulations. The geometry is constructed and analyzed in a similar manner to that described for the nanowire case in Chapter 3 so that the nanowire axis is aligned with the [110] crystal direction and interatomic forces are approximated using the linearized Stillinger-Weber potential [48].

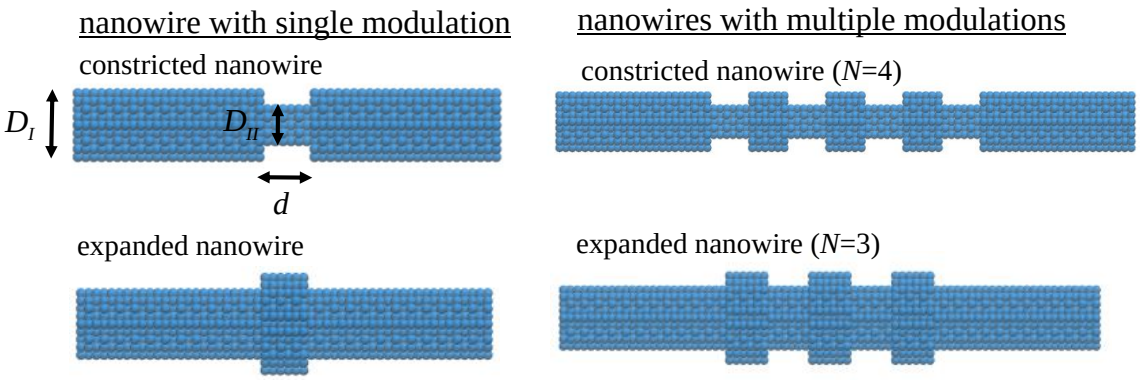

Figure 6.1: Example modulated nanowire geometries.

Further motivating the investigation of the diameter modulated nanowire is the fact that phonon transport has been investigated in similar geometries by previous researchers with alternative computational approaches. These previous studies are surveyed in section 6.2 of this chapter. The discussion of the prior work focuses on identifying shortcomings associated with the previously employed computational methods and how the LD-SBM approach represents an improvement on them. In section 6.3, the analysis of the ballistic thermal conductance through the system is developed. In section 6.4, detailed transmission and conductance results are presented for an example constricted nanowire that serves as a baseline case to which later results are compared. The effect of structural relaxation on phonon transmission and conductance through the constricted nanowire is also explored. Section 6.5 presents the results of a focused study on three key geometrical parameters: the size ratio of modulation, the length of modulation, and the number of modulations. Section 6.6 proposes a framework for a simplified model of phonon transmission that can be used to approximate the thermal conductance through the nanowire modulation at all temperatures. Section 6.7 summarizes the most important findings.

6.2 Survey of Previous Modeling Work:

6.2.1 *Molecular Dynamics Studies*

Molecular dynamics (MD) simulation is one popular way by which the effects of geometry on nanowire thermal properties have been modeled. Studies employing MD

have shown that modulation or rippling of nanowire boundaries can suppress phonon transport and reduce nanostructure thermal conductance by factors that range from 10 to 75% [37-39]. These MD investigations have highlighted the potential for nanostructure geometry to suppress phonon transport and obtain reduced thermal conductivity. However, they are unable to uncover many of the mechanisms by which phonon transport is suppressed as they are only able to predict aggregate phonon behavior and thermal properties, not the behavior of individual vibrational modes. Additionally, since MD simulations are based upon the numerical solution of classical equations of motion, they are only rigorously applicable to studying phonon transport at moderate to high temperatures for which the classical description is appropriate. Aggregate phonon transport at low temperatures, a regime which is important for the attainment of more efficient thermoelectric materials in cryogenic applications and where phonon transport is more geometrically tunable due to the reduced overall importance of anharmonic phonon processes, is not accurately modeled via conventional MD simulation. It should be noted that MD can be used to accurately model the scattering behavior of individual phonon modes through the use of MD wavepackets (described in Section 3.4). The inaccuracy of MD at low temperatures is related to its inability to properly account for non-classical phonon distributions in a thermalized system where many modes are activated. In contrast to conventional MD, the LD-SBM approach utilized herein isolates the behavior of individual phonon modes and is able to account for quantum occupation of low frequency modes which is the reason why the MD approach fails at low temperature.

6.2.2 *Lattice Dynamics – Relaxation Time Model*

An alternative computational approach to modeling phonon transport in diameter modulated nanowires was employed by Nika et. al [103]. Their study investigated phonon heat conduction in infinitely long modulated nanowires of square cross-section using an atomistic lattice dynamics based model. In contrast to the approach used in this dissertation where phonon spectra are calculated for semi-infinite, straight nanowire leads and the modal transmission through the irregular geometry is calculated, the model employed by Nika et. al utilized the translational symmetry of atomic displacement inherent to infinitely long systems to calculate phonon spectra of a modulated nanowire section. Each modulated nanowire section was treated in an analogous manner to that described for the supercells in Chapter 2, but each section contained the modulated geometry (i.e. two different side lengths). In this way, the effect of the modulation is accounted for within the phonon spectra calculation and the modal phonon transmission is not needed. Such an approach is only valid for an infinitely long modulated system. They used the modified phonon spectra to calculate the thermal conductivity of the nanowire using the relaxation time approximation by estimating the total relaxation time from the combined effects of phonon-phonon, phonon-impurity, and phonon-boundary scattering. Empirically fit analytical models were used to calculate relaxation times associated with phonon-phonon and impurity scattering and a simple, geometry dependent and specularity parameter based model was used to estimate the effect of boundary scattering. Their model predicted a three to sevenfold drop in the phonon heat

flux in the modulated nanowire over a temperature range of 50 to 400K relative to an unmodulated nanowire. The reduction in phonon heat flux was interpreted as being associated with a reduction in phonon group velocity of the confined phonon modes and "trapping" of phonon modes within the modulated nanowire segments. The nanowires investigated in their study had an unmodulated side length of about 2 nm. Their study gave a very complete theoretical investigation of phonon transport in size modulated Si nanowire systems since they were able to account for all of the relevant phonon processes over a wide range of temperatures. However, the analytical framework of their study only afforded the opportunity to investigate the infinitely long nanowire case. While the infinite nanowire is of technological and scientific interest, analyzing the transmission of individual modes through irregular sections of finite length, as the LD-SBM approach does, gives an alternative approach to understanding phonon transport that enables greater understanding of how the number of geometrical interfaces affect phonon transport and affords the opportunity to investigate non-periodic and isolated nanowire modulations.

6.2.3 *Continuum Scalar Wave Transmission Model*

Zianni [104] used an alternative approach focused only on geometry-induced phonon scattering processes and their effect on the phonon heat flux. In her study, the mode-dependent phonon transmission of phonons originating from semi-infinite straight GaAs nanowire sections incident upon sections of modulated width were calculated and

used with a Landauer [40] approach to estimate the ballistic thermal conductance. She found that the phonon heat conductance is reduced for a larger number of repeated modulations and eventually saturates after about 5 successive modulations to the infinite periodic case. She also found that modulating the nanowire width non-periodically is more effective at suppressing phonon transport than periodic modulations. Her results indicated the possibility to optimally tune phonon transport in order to reduce the parasitic heat flow and enhance thermoelectric efficiency. The accuracy of this study is limited by the fact that the model used for phonon spectra and transmission is greatly simplified. For instance, the study employed a continuum elastic wave model to calculate phonon normal modes and phonon transmission. As demonstrated in Chapter 4 of this dissertation, the use of continuum models is only appropriate for modeling very long wavelength, low-frequency phonon modes. In addition, the model employed by Zianni was an uncoupled scalar wave equation that is only rigorously appropriate for modeling one subset of modes, shear horizontal modes, in plate-like two-dimensional structures. In contrast, the LD-SBM model employed herein is atomistic, and as discussed in previous chapters, gives a more accurate representation of nanowire mechanics across the full phonon spectrum.

6.3 Analysis of Phonon Transport in Modulated Si Nanowires

6.3.1 *Analysis of Thermal Conductance*

The aggregate phonon transport through the irregular geometry is characterized by the thermal conductance, which is the ratio of the total heat flow through the geometry associated with a temperature drop ΔT across the geometry. The ballistic thermal conductance, σ, is estimated using the Landauer approach for ballistic energy carriers whereby the thermal conductance is evaluated in the limit of an infinitesimal temperature drop across the geometry and the phonon populations on either side of the geometry are assumed to be in quasi-equilibrium and may be evaluated from the Bose-Einstein distribution at an assumed average system temperature. Under these assumptions the ballistic thermal conductance can be evaluated by integrating the contribution of each mode over phonon wavenumber, *k*, and summing over phonon branches, ν:

$$\sigma = \frac{1}{2\pi} \sum_{\nu}^{3N_{sc}} \int \alpha_{k,\nu} \left| v_{k,\nu} \right| c_{k,\nu} dk \tag{60}$$

This equation is derived in Section 1.4 of this dissertation. The specific heat of each phonon mode, $c_{k,\nu}$, is given by:

$$c_{k,\nu} = \hbar \omega_{k,\nu} \frac{\partial f^{BE}_{\omega_{k,\nu}}}{\partial T} \tag{61}$$

Note that in this context ν signifies a phonon branch index that spans all phonon branches, the total number of which is equal to $3N_{sc}$ where N_{sc} is the total number of

atoms in the reference nanowire lead supercell. $\alpha_{k,\nu}$ is the modal phonon transmission coefficient which is the fraction of energy incident in a mode indexed by k and ν that is transmitted through the geometry and $v_{k,\nu}^{group}$ is the group velocity of each mode. Formulating the ballistic thermal conductance as an integration over wavenumber is convenient since it highlights the wavenumber/wavelength dependence of the modal transmission as well as each mode's individual contribution to ballistic thermal conductance. This contribution is analyzed by defining the modal contribution to thermal conductance:

$$\eta_{k,\nu} = \frac{\alpha_{k,\nu} \left| v_{k,\nu}^{group} \right| c_{k,\nu}}{2\pi} \tag{62}$$

It is also convenient to formulate the thermal conductance as an integration over frequency rather than wavenumber, utilizing the fact that $\left| v_{k,\nu} \right| = \frac{\partial \omega}{\partial k}$, so that it may be calculated from

$$\sigma = \frac{1}{2\pi} \int_0^{\omega_{\max}} \sum_{\nu}^{N_\omega} c_{\omega,\nu}^{ph} \alpha_{\omega,\nu} d\omega \tag{63}$$

In this context, ν signifies a mode index that spans the total number of propagating modes, N_ω, at a given frequency. The magnitude of the thermal conductance is very sensitive to the size of the nanowire lead cross-sections which determines N_{sc} and N_ω. In order to focus on geometry shape effects (manifest through the parameters d, N, and D_{II}/D_I) rather than focusing on nanostructure size effects on thermal conductance, it is

useful to consider the aggregate thermal transport of a given geometry relative to a straight nanowire. To do this, a dimensionless conductance ratio, σ^*, is defined to be the ratio of the ballistic thermal conductance of the modulated nanowire, σ_{mod}, relative to that of the unmodulated nanowire of the same D_I throughout, σ_{unmod}:

$$\sigma^* = \frac{\sigma_{\text{mod}}}{\sigma_{\text{unmod}}} \tag{64}$$

The conductance ratio is a temperature dependent quantity that allows for the modal specific heat to vary between modes of different frequency. In the high temperature limit, the phonon populations approach a classical distribution where each mode contributes an equal amount, k_B, to the modal specific heat and the temperature dependence can be removed entirely from the expression for the conductance ratio. Thus, the total transmission, $\alpha_{tot,\omega}$, and the total number of modes at each frequency, N_ω, become the chief parameters that characterize phonon transport in the modulated nanowire system. Integrating over each, and taking the ratio results in a simple expression for the "classical conductance ratio", σ_C^*, which is used as the primary measure of phonon suppression in the modulated nanowire system.

$$\sigma_C^* = \frac{\int_0^{\omega_{\max}} \alpha_{tot,\omega} d\omega}{\int_0^{\omega_{\max}} N_\omega d\omega} \tag{65}$$

Where,

$$\alpha_{tot,\omega} = \sum_{\nu}^{N_\omega} \alpha_{\omega,\nu} \tag{66}$$

Note that for the unmodulated nanowire, the modal transmission equals one for all modes since there is no irregular geometry to cause phonon scattering.

At higher temperatures, which is the situation under which the expression for σ_C^* is derived, anharmonic processes have significant impact on phonon transport and the purely harmonic approach used in LD-SBM model is only an approximate treatment of the phonon-geometry scattering process. At lower temperatures, anharmonic processes are not as prominent and the LD-SBM model is expected to more accurately predict phonon transmission. However, in the lower temperature regime, the value of σ_C^* may not be equal to σ^* due to lower relative occupation of higher frequency modes. Despite this limitation, σ_C^* is the most convenient single measure of aggregate phonon transmission for a given geometry even when it is not rigorously equal to σ^*. This is because σ_C^* is independent of the exact phonon distribution and system temperature whereas σ^* is not. Moreover, it was found that σ_C^* can serve as an input into a simple, approximate model which predicts σ^* at all temperatures (described in Section 6.6).

6.4 Baseline Case: Single Isolated Nanowire Constriction

6.4.1 *Atomic Configuration*

The analysis of phonon transport in the modulated silicon nanowire system begins by first considering, in detail, phonon transmission through a single isolated nanowire constriction. This serves as a baseline case to which later results are compared. Figure 6.2 shows the geometry of interest. The diameter of the incident side, D_I, is 1.72 nm. The length of the constriction, d, is 1.15 nm, and the diameter of the constricted section, D_{II}, is 0.95 nm.

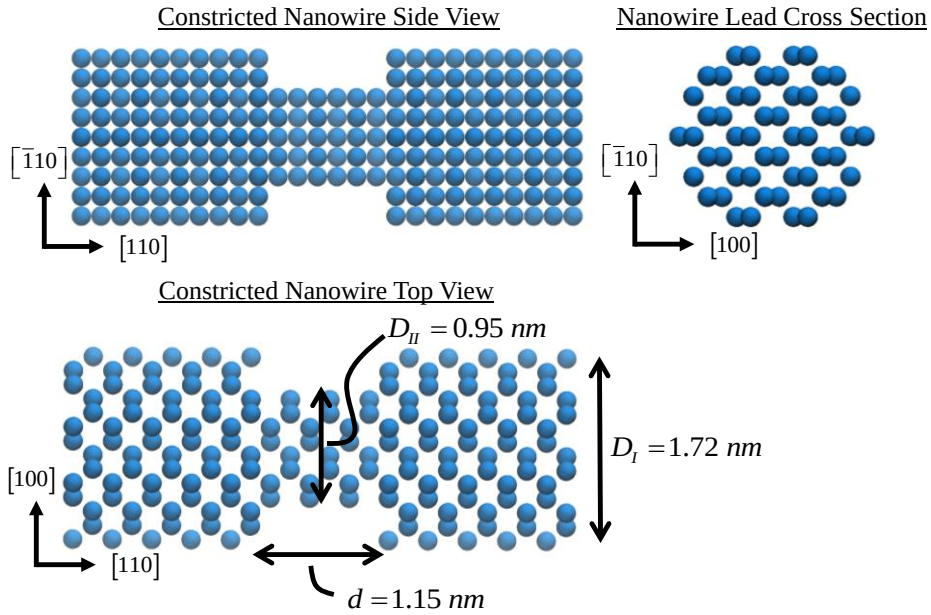

Figure 6.2: Geometric details of baseline constricted nanowire.

6.4.2 *Transmission Results*

Figure 6.3(b) presents the total phonon transmission across the nanowire constriction as a function of frequency. Note that these results, and others, are plotted against ordinary frequency, *f*, as opposed to angular frequency, ω, whereby $\omega = 2\pi f$. Comparison with the total number of phonon modes at those frequencies shows that phonon transport is greatly suppressed by the constriction. For reference, the full phonon dispersion relation of the nanowire leads is shown in Figure 6.3(a). The zeroth order extensional, torsional, and flexural modes are highlighted in color while the higher order modes are shown in black. The modal phonon transmission coefficients of all calculated modes are plotted in Figure 6.3(c) which indicates that the vast majority of modes exhibit relatively low phonon transmission with little obvious dependence on wavenumber. Despite the fact that many of the modes exhibit low modal transmission (e.g. between 2 and 5 THz), their aggregate behavior impacts the overall shape of the frequency dependent transmission curve due to the fact that there are a large number of modes at those frequencies. Because of this, the shape of the transmission curve as a function of frequency is dominated by the number of modes at a given frequency rather than being heavily influenced by the transmission behavior of any one mode or group of modes.

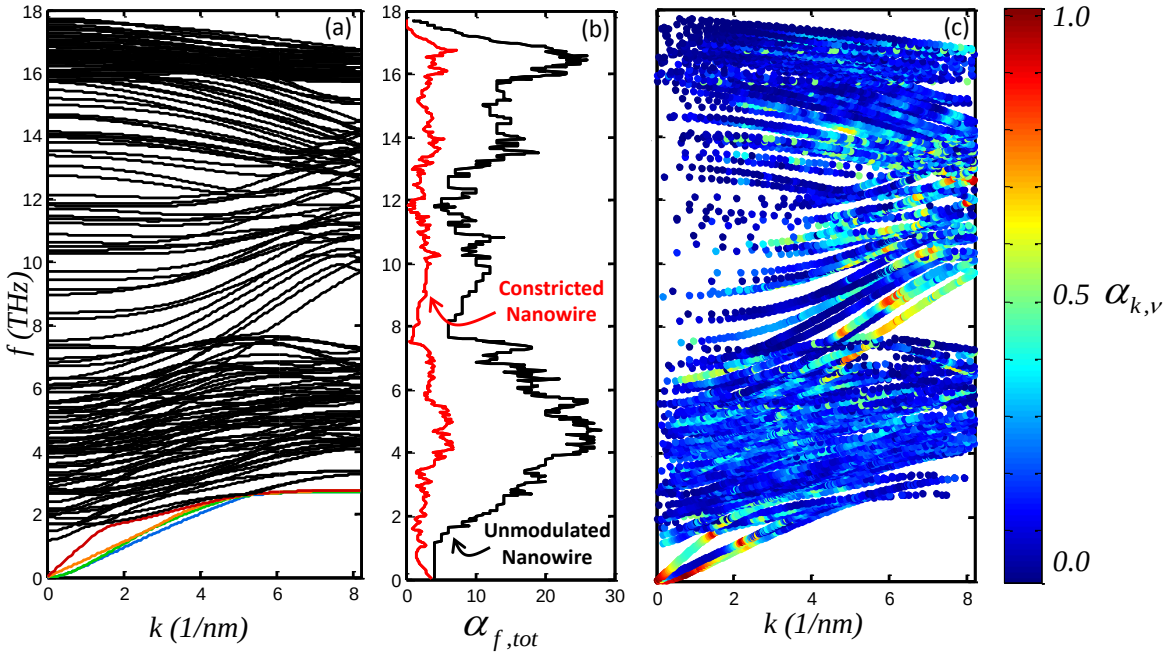

Figure 6.3: a) Full phonon dispersion relation of nanowire lead as shown in Figure 6.2. Zeroth order phonon branches are highlighted in color: extensional (red), torsional (orange), 2 flexural branches (blue and green). Higher order branches are colored in black. b) Frequency dependent phonon transmission through nanowire constriction shown in Figure 6.2 compared with phonon transmission through straight nanowire. c) transmission of individual modes through nanowire constriction.

In contrast, some phonon bands, for example the zeroth order phonon branches at frequencies less than about 1 THz, exhibit higher phonon transmission and greater variability in phonon transmission as a function of wavenumber. The modal transmission behavior of all phonon modes, zeroth order modes included, is quite complicated. As discussed in 5.1.2, this is due to the fact that each phonon scattering process involves interactions with many other phonon modes including evanescent vibrational disturbances localized near the modulation as well as overlapping constructive and destructive interference effects within the modulation that are unique to each mode type. Some of the complicated behavior is adequately understood through an uncoupled, one-

dimensional beam theory analysis that was shown in Chapter 5 to accurately model long wavelength zeroth order phonon transmission. On the other hand, at higher wavenumbers, more complicated, less easily explained transmission curves result from the fact that the mode shapes associated with each mode are more complicated (Figure 5.5) and there is greater possibility for interactions with propagating higher order modes. Some of the discontinuities observed in the transmission curves, for example, the discontinuity that appears in the transmission of the extensional mode (Figure 6.4) at around k=1.5 (1/nm), are correlated with the cutoff frequencies of some of the higher order modes. This behavior is similar to that exhibited by zeroth order shear-horizontal (SH) phonon branches incident upon stepped plate junctions where the discontinuities in transmission are easily attributable to the activation of higher order propagating SH branches (see, for example, Figure 4.8). Other features in the transmission curves have no easily identifiable relation to the properties of the mode, geometry, or the overall phonon band structure and are likely the product of many different competing phenomena. A detailed accounting of all the features of the phonon transmission curves and their causes is not attempted in this dissertation. Rather, the aim is to characterize general trends in the aggregate phonon transmission with an aim to better understand how geometry affects overall thermal transport.

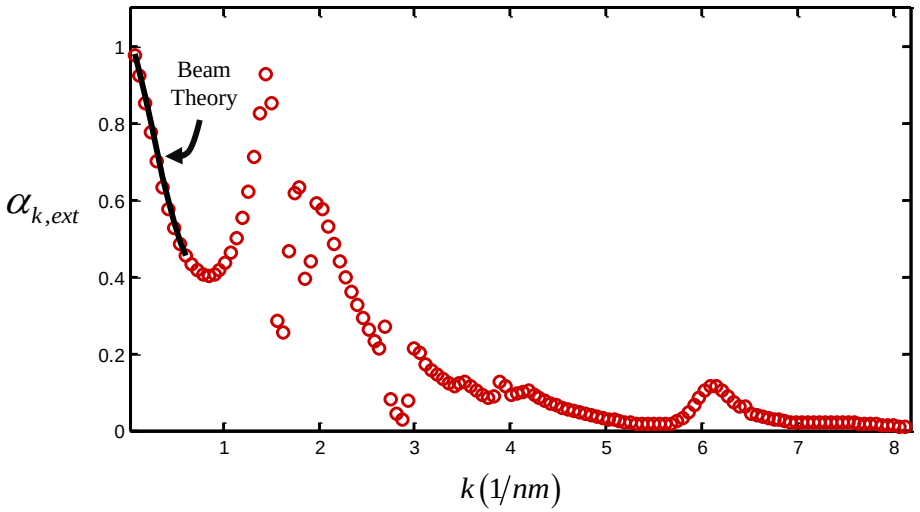

Figure 6.4: Wavenumber dependence of modal phonon transmission of extensional phonon branch through nanowire constriction (Figure 6.2). Long wavelength behavior is adequately approximated by the beam theory (dashed black lines) model developed in Chapter 5.

6.4.3 *Conductance Ratio Results*

The conductance ratio versus system temperature is plotted in Figure 6.5. Two distinct regimes are evident in the figure: a higher temperature regime in which the conductance ratio is independent of temperature and is equal to the classical conductance ratio and a low temperature regime, where the conductance ratio rapidly decreases with increasing temperature. Because higher frequency modes contribute very little to the modal specific heat at lower temperatures, the four zeroth order branches dominate thermal transport in this regime. As such, the low temperature behavior of the conductance ratio can be understood by considering the behavior of only these four branches. To illustrate this point, the conductance ratio as estimated by beam theory is plotted in Figure 6.5 alongside the result obtained from the full calculation. The beam

theory estimate is calculated from Eq. (54) by summing ν over the first four modes and calculating $\alpha_{\omega,\nu}$ from Table 5.4 (nanowire constriction or expansion case). As the figure shows, the simple beam theory model closely matches the full calculation result at low temperatures. In Chapter 5 it was found that this model is adequate for estimating the transmission of the zeroth order phonons with scaled wavenumbers, *kD*, less than 0.50, where *D* is the largest diameter in the system. For an approximate rule of thumb that is temperature dependent, the use of the beam theory model alone is recommended for temperatures less than $T_{beam} \approx \frac{1}{2}\frac{\hbar\omega_c}{k_B}$ which corresponds to the temperature at which the majority of the thermal energy is concentrated in modes with frequencies that are less than approximately half the cutoff frequency, ω_c, of the first higher order mode. Since simple beam theory enables an approximate analysis of phonon suppression at low temperatures, the focus of the remainder of this chapter is primarily on the aggregate phonon behavior as manifest through the classical conductance ratio whereby all modes, not just the few low frequency modes, contribute equally to the modal specific heat. However, the beam theory model and the classical conductance ratio can be used together form the basis for a composite simple model that can be used to estimate the thermal conductance ratio at any temperature. This model is proposed and explained in more detail in Section 6.6.

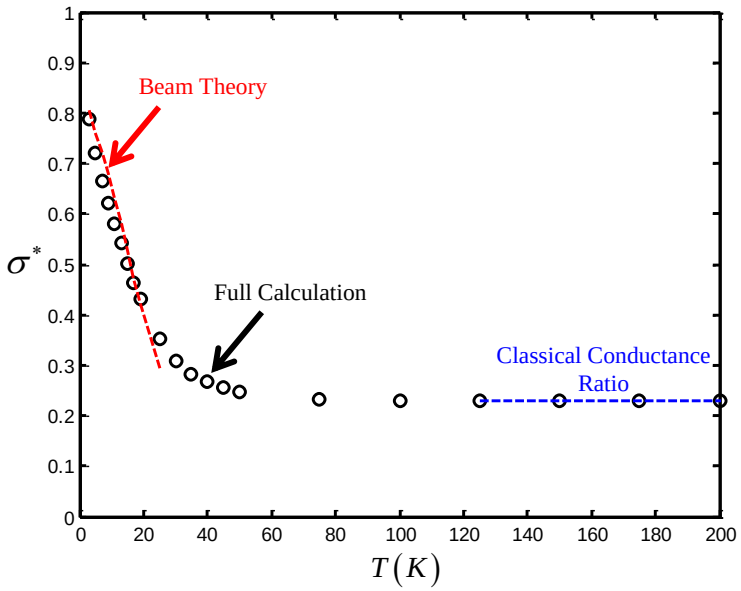

Figure 6.5: Calculated conductance ratio of constricted nanowire (Figure 6.2) as a function of system temperature. Low temperature behavior adequately approximated by simple beam theory model as developed in Chapter 5. Conductance ratio approaches constant value of σ_C^* at higher temperatures.

6.4.4 *Evaluation of Structural Relaxation*

The effect of structural relaxation near the geometric feature on phonon transport in the constricted nanowire is also investigated. Most of the results presented in this chapter and other chapters do not allow for structural relaxation in the system. As a result, the system is analyzed such that all atoms are in idealized, perfectly periodic equilibrium positions. While this configuration represents a local minimum in the potential energy landscape, it does not represent a global potential energy minimum. A more realistic/accurate treatment would allow for structural relaxation to lower potential energy equilibrium configurations. Because the relaxed equilibrium configuration

includes atomic placements that are not perfectly periodic or symmetric it will cause additional phonon scattering, the magnitude and nature of which is not known *a priori*.

In order to investigate the effect of structural relaxation near the irregular geometric feature, the phonon transmission through a relaxed atomic configuration was calculated. The relaxed configurations were obtained by extending the buffer region (defined in Chapter 3) to include 4 additional atomic planes on either side of the constriction. The atoms belonging to the buffer region and the irregular geometry were allowed to relax while the atoms in the nanowire leads remained fixed at their base configuration. Fixing the nanowire leads is necessary since the LD-SBM computational method requires that the nanowire leads be perfectly periodic. Relaxed configurations were found by performing MD simulations at a desired relaxation temperature and calculating the time averaged atomic positions over a period of 1 ns. The MD simulations were executed using the LAMMPS parallel molecular dynamics simulator [105,106] and, similar to the LD-SBM calculations, employed the Stillinger-Weber potential. The configuration associated with the time-averaged atomic positions was relaxed to a local minimum energy configuration by iteratively moving atoms in the direction of lower potential energy using the simple gradient method. The additional simple gradient energy minimization step is used to eliminate perturbations to the equilibrium configurations associated with small errors in time-average position. This effect could generally be ignored with negligible impact on phonon transmission, but was done to ensure the stiffness matrices required for the transmission calculation were calculated

precisely at the bottom of the local potential energy well. This method of structural relaxation operated on the principle that the addition of thermal energy allows the structures to overcome local potential energy barriers in a manner that is temperature dependent resulting in enhanced relaxation and greater perturbation to the base structure at higher relaxation temperatures. Relaxed structures corresponding to several MD simulation temperatures are presented in Figure 6.6. The amount of reduction in potential energy versus relaxation temperature is plotted in Figure 6.7. For the lowest relaxation temperature case, $T_{relax}=10K$, very little difference from the unperturbed base structure is observed and negligible reduction in potential energy is obtained. This indicates that the thermal energy associated with relaxation temperatures below 10K is not enough to overcome the potential energy barriers surrounding the base configuration. Higher relaxation temperatures allowed the system to escape the local potential energy minimum associated with the base configuration and resulted in larger reductions in potential energy relative to the base configuration. Correspondingly, increased relaxation temperature resulted in greater reorganization of equilibrium atomic positions and greater differences between the relaxed configuration and the base structure. The amount of reduction in potential energy that can be attained through this method plateaus for relaxation temperatures greater than 200K. Note that the structural relaxation that occurs is largely associated with a reorientation of bonds, rather than coarse reorganization of the structure. This means that its boundary dimensions remain very similar to those of the base configuration and the other relaxed configurations. Close inspection of the

relaxed configuration indicates that the change in D_I or D_{II} relative to the base configuration is at most half the distance between one atomic plane (≈0.09 nm).

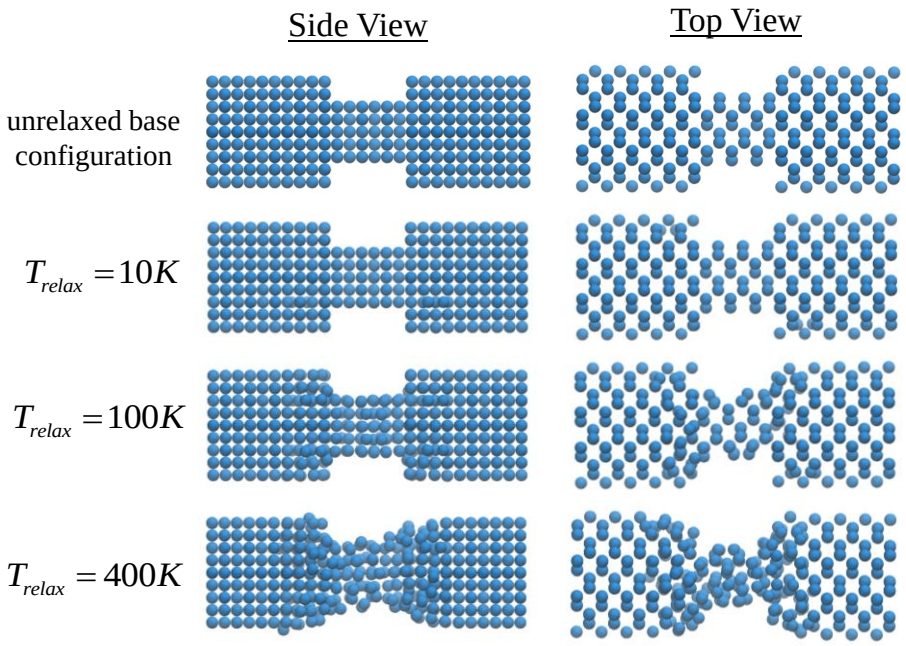

Figure 6.6: Relaxed equilibrium atomic configurations of nanowire notch. Dimensions of unrelaxed base configuration are the same as in Figure 6.2. D_I is 1.72 nm, D_{II}, is 0.95 nm, and d is 1.15 nm.

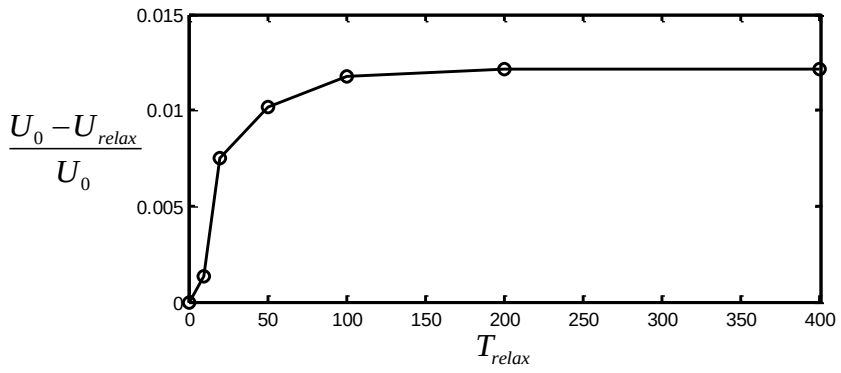

Figure 6.7: Reduction in potential energy of relaxed configurations. U_0 is the potential energy of the base unrelaxed equilibrium configuration. U_{relax} is the potential energy of the relaxed configuration.

The phonon transmission versus frequency for two different relaxed configurations and the base configuration is plotted in Figure 6.8. Negligible differences in phonon transmission associated with the various relaxed cases and the base configuration are observed for phonon frequencies less than 1THz. The reason why these phonons are unaffected by relaxation is because the length scale of the relaxation, the bond length (≈0.10 nm), is much less than the length scale associated with the variation in atomic displacement corresponding to these modes. This is because the wavelengths of these modes are greater than 5-10 nm (depending on mode) and, due to their simple mode shape vectors (see *kD*=0 in Figure 5.5), exhibit little to no transverse variation in displacement. Contrastingly, the transmission of higher frequency phonons are significantly affected by the relaxed configurations resulting in enhanced phonon scattering and an overall decrease in phonon transmission. While greater structural relaxation clearly causes enhanced suppression of higher frequency phonons, the effect of

structural relaxation on specific phonon modes, has not been explored, and perhaps merits future additional research.

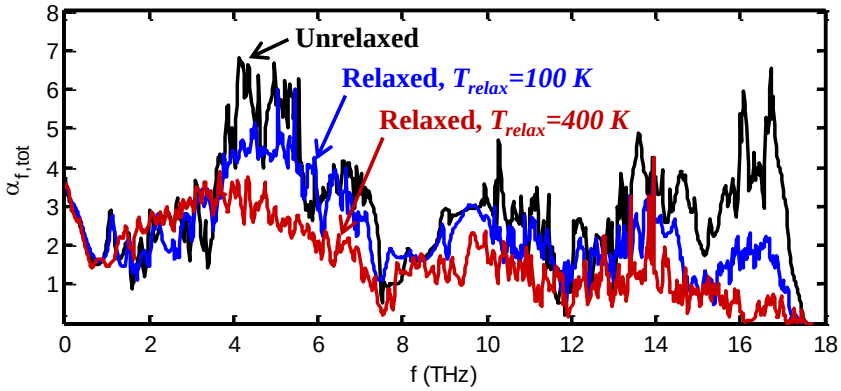

Figure 6.8: Effect of structural relaxation on phonon transmission through the nanowire constriction. The transmission results for T_{relax}=10 K are not plotted since they are negligibly different from the unrelaxed results.

The effects of structural relaxation on thermal conductance ratio were also observed (Figure 6.9). All three relaxation temperatures considered resulted in a reduction in the conductance ratio, σ^*, at higher temperatures. The reduction corresponding to the lowest relaxation temperature (T_{relax}=10K) is minimal since the corresponding relaxed structure and phonon transmission were nearly identical to those of the base unrelaxed configuration. Greater reduction in conductance was calculated for the more relaxed configurations obtained from the higher relaxation temperatures of T_{relax}=100K and T_{relax}=400K. The greatest reduction in σ^* relative to the unrelaxed case was about 21% for T_{relax}=100K and about 40% for T_{relax}=400K. However, for all three cases, the conductance ratio at lower temperatures (less than around 50K) shows little

sensitivity to relaxation due to the fact that the transmission of low frequency phonons is largely unaffected by structural relaxation.

The phonon transmission and conductance results presented in the remainder of this chapter are obtained from computations on unrelaxed configurations. This is done in order to reduce the computational time required for each calculation and in order to focus on coarse changes in nanostructure geometry as manifest through D_{II}, d, and N, rather than trying to deduce detailed dependence of phonon transport on different relaxed configurations. As indicated by the limited study on structural relaxation, the reader should note that the transmission results of low frequency phonons are likely independent of structural relaxation. In contrast, higher frequency phonons, and consequently conductance ratios evaluated at higher temperatures, are likely to be lower in relaxed modulated nanowires than unrelaxed modulated nanowires.

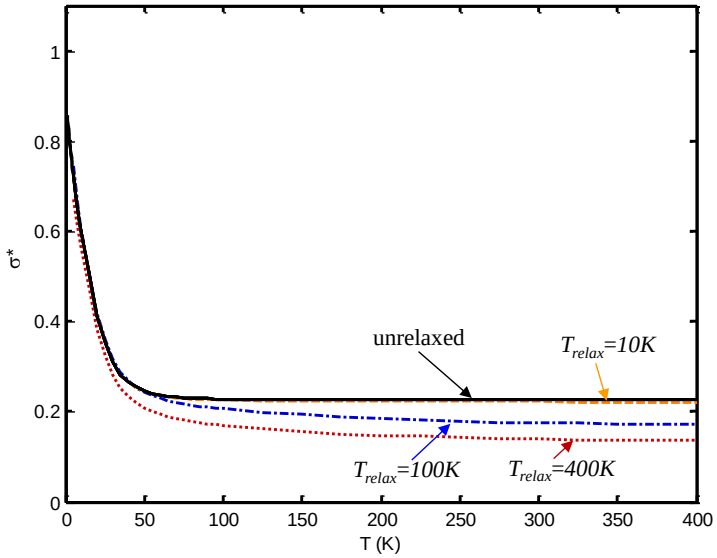

Figure 6.9: Effect of structural relaxation on conductance ratio.

6.5 Geometry Study: Results and Discussion

Having performed a thorough investigation of the baseline constricted nanowire geometry shown in Figure 6.2, D_{II}, N, and d were varied to gain an understanding of how each affects phonon transmission and thermal conductance.

6.5.1 *Investigation of Modulation Diameter*

In the investigation of D_{II}, the length of the modulated section, d, was held constant at the baseline value and the size ratio, $\frac{D_{II}}{D_I}$, of the modulation was varied. In Figure 6.10 σ_C^* is plotted versus the size ratio, which varies from values less than one (corresponding to the constricted nanowire case) to values greater than one (corresponding to the expanded nanowire case). Three different sizes of nanowire lead

are explored. For size ratios less than one, the results for the three nanowire lead sizes track fairly close together with size ratio. The behavior for $\frac{D_{II}}{D_I} < 1$ indicate that size ratio, not actual size, is the more important parameter concerning phonon scattering in these systems. This is consistent with the simple beam theory model that predicts monotonic increases in transmission as a function of size ratio.

For size ratios greater than one, somewhat different behavior is observed. All nanowire lead sizes exhibit a reduction in the conductance ratio as the size ratio increases. It is also observed that σ_C^* saturates with increasing size ratio, the saturation value decreases with decreasing lead sizes, and the onset of saturation occurs at smaller size ratios with increasing lead size. The σ_C^* saturation effect is consistent with the finding by Yang, et. al [57] who analyzed phonon transport in T-stub waveguides which are analogous to the nanowire expansion geometries investigated here. They found that for temperatures greater than 1K, T-stub heights greater than three times the waveguide height exhibited no changes in conductance when the T-stub height was increased. They attribute this behavior to the fact that the "wide energy range involved in the conductance calculation smears out all oscillations in the transmission coefficient." This explanation is plausible and is similar to what is observed in the investigation of modulation length, *d*, which is discussed in Section 6.5.2.

It should also be noted that the simple beam theory model developed in Chapter 5 is expected to model phonon transmission for the expanded nanowire case less well when the size ratio is large. This is because the role of higher order modes in the expanded section plays a greater role as the diameter of the expanded section increases. As such, it's not surprising that the limiting behavior for large size ratios predicted by the simple model (average transmission goes to zero) does not match the observed behavior for the expanded nanowire (average transmission saturates to a finite value). In addition, while it was not noted by Yang, et. al [57], close inspection of the behavior of the T-stub waveguide indicates that the formation of standing waves transverse to the waveguide length results in a saturation of the average transmission of the SH0 mode at larger size ratios. This limiting behavior is much different than that predicted by a 1-D analysis of the T-stub system analogous to that presented for the nanowire geometry in Chapter 5. A more sophisticated simple model that accounts for higher order mode effects and/or standing waves transverse to the nanowire axis may be required to better explain both size and size ratio dependence of the saturation of σ_C^* at higher $\frac{D_{II}}{D_I}$. Nevertheless, these results indicate that, at least for small nanowire systems, increasing the nanowire size can increase the aggregate phonon transmission even if the size ratio is held constant.

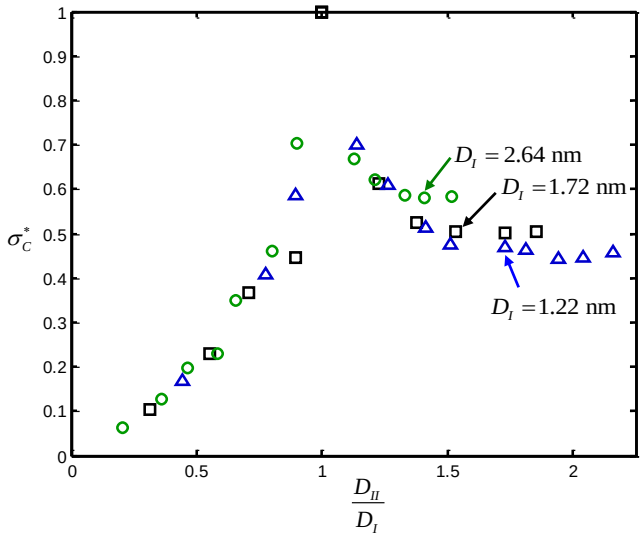

Figure 6.10: Effect of aggregate phonon transmission on modulation size. The length of modulation, *d*, is held constant at 1.15 nm. Three different sizes of nanowire leads were investigated.

6.5.2 *Investigation of Modulation Length: Classical Limit*

The effect of the modulation length, *d*, on phonon transmission was also explored. The phonon transmission is plotted versus frequency for three different values of *d* in Figure 6.11. The modal transmission coefficients of individual modes are clearly sensitive to the length of the modulation and exhibit resonance and interference phenomena that are strongly dependent on modulation length. This is best shown in the inset of Figure 6.11 which plots the low frequency portion of the phonon transmission for three different modulation lengths and demonstrates how *d* affects the frequencies where transmission peaks and valleys occur. This effect was also evident in Figure 5.9 which plots the transmission of individual phonon branches versus wavenumber for a comparable geometry. While changing *d* modifies the periodicity at which peaks and

valleys occur in the transmission at low frequencies, this has little overall effect on the conductance ratio when all modes are considered. Figure 6.12 plots σ_C^* versus modulation length for two different size ratios and demonstrates that σ_C^* exhibits little sensitivity to changes in the length of the modulated section. The conductance ratio varies by at most 5% from the mean value.

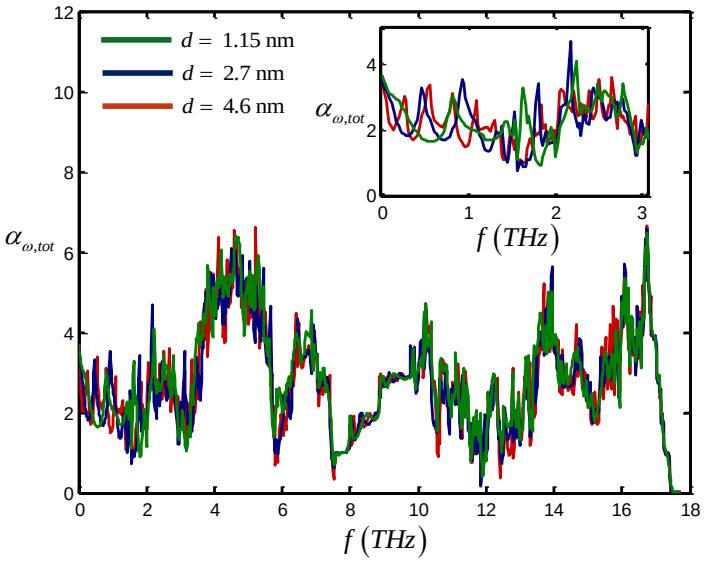

Figure 6.11: Effect of modulation length, d, on phonon transmission through single modulation. D_I=1.72 nm, D_{II}=0.95 nm. While some of the peaks in transmission are misaligned due to interference effects that are dependent on d, the overall shapes of the transmission curves are similar. The effect of d on the location of specific peaks is best observed when looking only at the low frequency transmission which is shown in the inset figure.

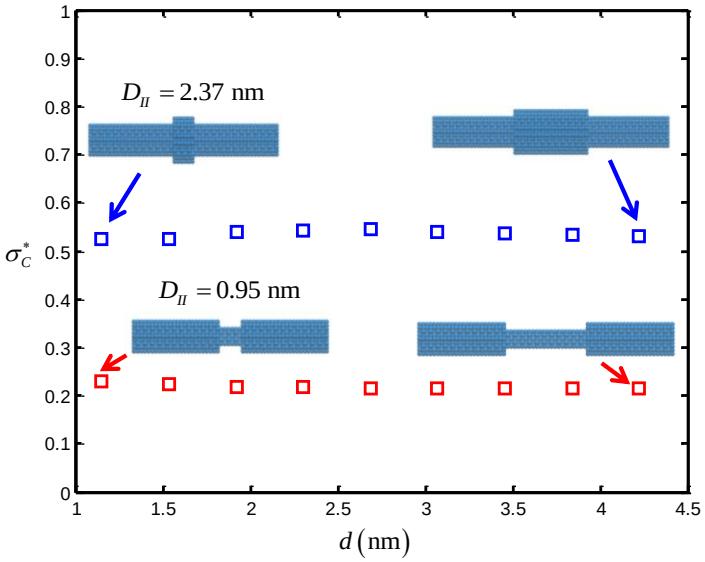

Figure 6.12: Effect of modulation length on aggregate phonon transport through single modulation. Diameter of nanowire lead is 1.72 nm. Two different modulation diameters are presented.

The small sensitivity of thermal conductance on modulation length arises from the fact that many modes contribute to thermal transport across the irregular geometry. For the small nanowire lead size investigated in this study, there can be more than 20 different modes contributing to heat transfer at some frequencies. These modes belong to different dispersion curves and have different wavenumbers. As a result, their transmission dependence on modulation length will be different such that a peak in transmission for one phonon branch may align with a valley in transmission for another branch. When summed over many different modes and averaged over frequency, any dependence one particular mode has on *d* is blurred by the behavior of all of the other modes and the thermal conductance is largely independent of *d*. Increasing the diameter of the nanowire leads will in general increase the number of modes at a given frequency

and further obscure any modal dependence on *d* in the evaluation of overall thermal conductance. Thus, for all but the lowest temperatures it is unlikely that *d* could be used to tune thermal conduction.

It should be noted that in the study on modulation number (Section 6.5.3) it will be shown that increasing the number of interfaces decreases aggregate thermal transport. Thus, for a given fixed overall length, reducing the length, *d*, of an individual modulation allows for an increase in interface/modulation number density which would in turn decrease the thermal conductance. This effect is consistent with the findings of Liu and Chen [34] in their MD study on periodically rippled nanowires in which they found that short wavelength ripples, which correspond to shorter *d* and higher *N* within a set length, resulted in lower calculated thermal conductivity than nanowires with longer wavelength ripples.

6.5.3 *Investigation of Modulation Number*

The effect of the number of modulations, *N*, on the phonon transmission and thermal conductance was also explored. Figure 6.13 plots the total phonon transmission as a function of frequency for different numbers of nanowire modulations for an example expanded nanowire case. Additional modulations consistently reduce phonon transmission for almost all frequencies. The effect of additional modulations on aggregate phonon transport as manifested through σ_C^* is plotted in Figure 6.14. Increasing *N*, while holding all other parameters constant, reduces the aggregate phonon

transmission for all values of size ratio considered. However, the amount of reduction that can be achieved by adding modulated sections lessens for higher values of *N*, and appears to converge to a minimum value of σ_C^* for large *N*. These effects are consistent with a simple beam theory analysis of the zeroth order branches. The transmission result of the zeroth order modes calculated using the simple beam model is shown in Figure 6.15. The simple model predicts deeper valleys in transmission as the number of modulations is increased and a convergence effect at higher N. The average phonon transmission of these branches (Figure 6.16), as modeled using the simple beam theory model, also approaches a minimum value at higher *N* due to the fact that the valley width saturates with a larger numbers of modulations. The phonon dynamics as modeled using the LD-SBM computational approach are more complicated/realistic than that predicted by the simple model, but the saturation effect at higher N is qualitatively consistent between both approaches. The convergence of σ_C^* for large *N* is also consistent with the observation made by Zianni [104] that the reduction in conductance due to the addition of modulations saturates for larger values of *N*.

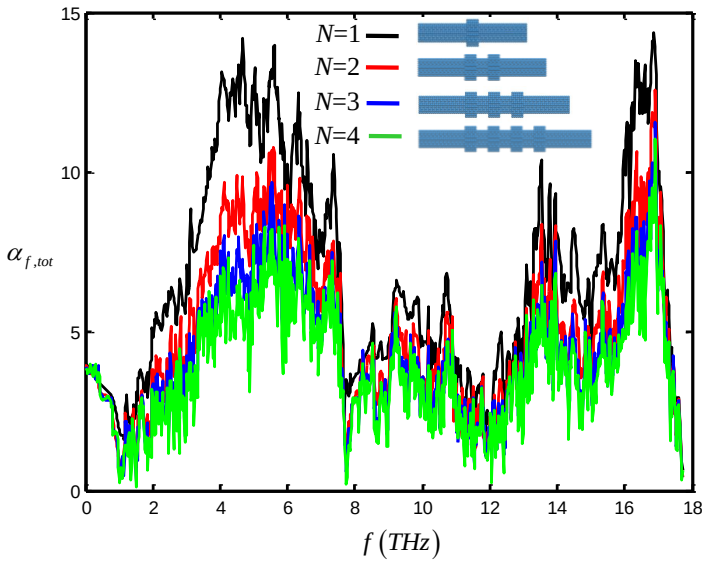

Figure 6.13: Total phonon transmission as a function of frequency for different numbers of nanowire modulations. Case plotted corresponds to D_I=1.72 nm and D_{II}=2.37 nm. The length of all modulated sections was held constant at *d*=1.15 nm. Adding modulations reduces the transmission for nearly all frequencies.

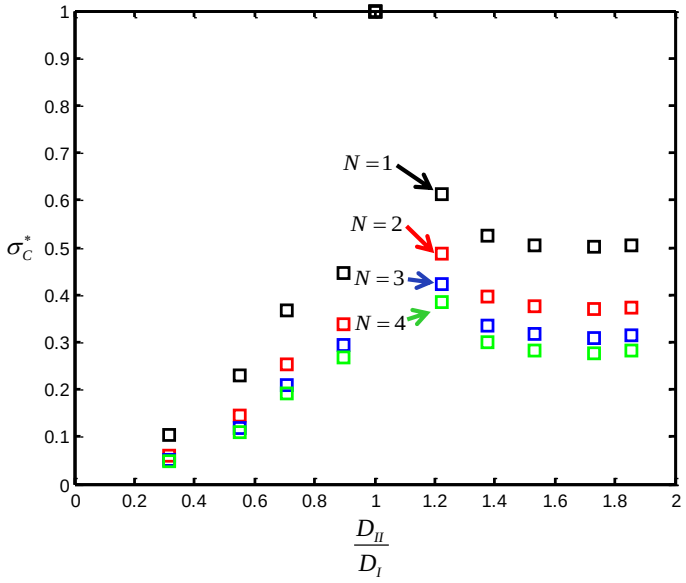

Figure 6.14: Effect of adding multiple modulations on aggregate phonon transport. Length of modulation, *d*, is held constant at 1.15 nm and the diameter, D_I, of the nanowire lead is 1.72 nm.

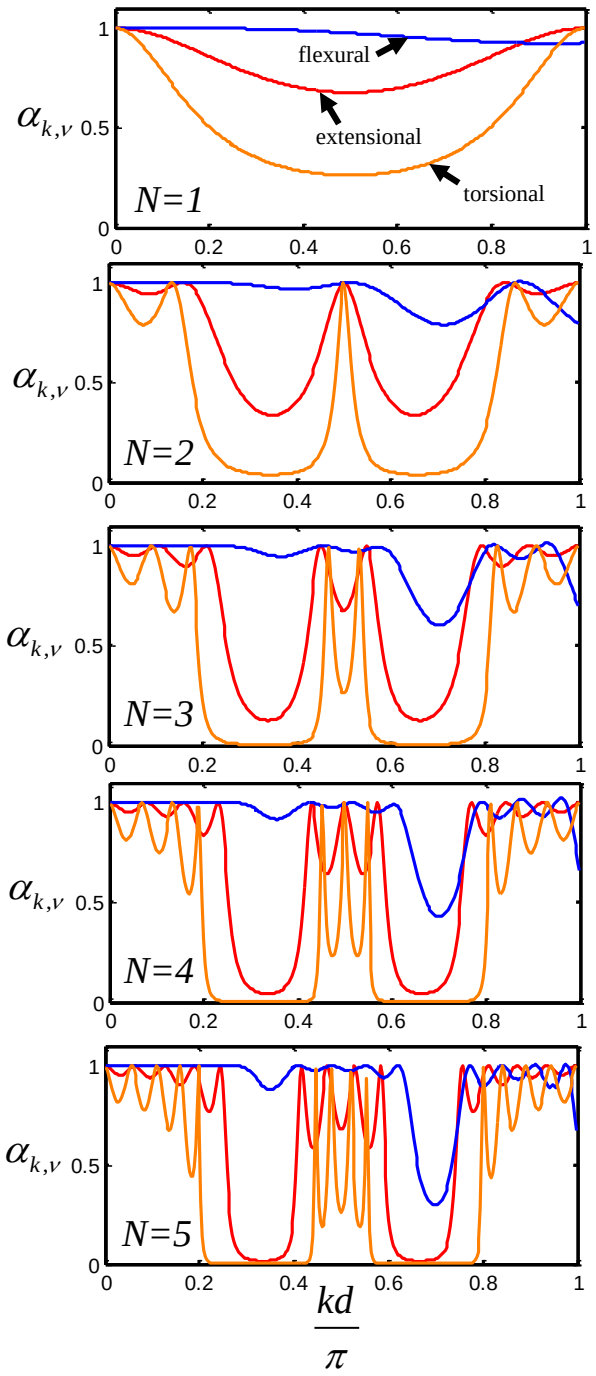

Figure 6.15: Modal transmission of zeroth order modes calculated using simple beam theory model (Section 5.2.3) for different numbers of modulation. The size ratio, D_{II}/D_{I} =1.38, is the same as that presented in Figure 6.13. Note that the valley width saturates with larger N which results in the saturation of the average transmission coefficient plotted in Figure 6.16.

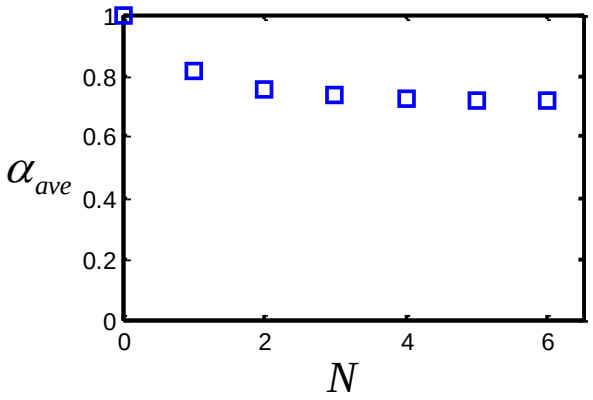

Figure 6.16: Average transmission of all four zeroth order modes over the intervals plotted in Figure 6.15 as calculated using the simple beam theory model. The saturation of average transmission with larger N is qualitatively consistent with the result calculated using the much more rigorous LD-SBM computational procedure.

6.5.4 *Investigation of Modulation Length: Low Temperature Effects*

The previous analysis whereby aggregate phonon transmission was quantified through the parameter σ_C^* is most useful for higher temperature cases when the modal contribution to thermal conductance $\eta_{k,\nu}$ is spread across the entire phonon spectrum and no single mode or group of modes dominates the thermal conductance. However, at lower temperatures, $\eta_{k,\nu}$, is significant only for the longest wavelength modes belonging to first several lowest frequency phonon branches. This is the case because the magnitude of modal specific heat term of the Landauer thermal conductance is negligible for the higher frequency modes. Additionally, at low temperatures it is possible to identify a range of wavenumbers that are dominant contributors to thermal conductance. This behavior is illustrated in Figure 6.17 which plots the normalized modal contribution to thermal conductance for the unmodulated nanowire versus wavenumber for a low

temperature example case (T=12K). The contribution of all branches combined, the first four branches combined, and the contribution of each zeroth order branch are plotted versus wavenumber. As Figure 6.17 shows, the first four branches account for the great majority of thermal conductance at this temperature. The phenomena of having a wavenumber or band of wavenumbers that dominate thermal conductance is associated with the combined behavior of the four zeroth order branches. The extensional and torsional branches are very strong contributors to thermal conductance at low frequencies since they have high group velocities. In fact, their contribution to the thermal conductance is maximum for frequencies approaching zero. Conversely, the two flexural branches are not strong contributors to thermal conductance at low frequencies as their group velocities approach zero in the low frequency limit. However, the contribution of the flexural modes grows substantially with increasing wavenumber since the group velocity of the flexural modes is linearly related to wavenumber in the long wavelength limit. Thus, the combined effect of the extensional, torsional, and two flexural branches at low frequencies results in a wavenumber at which the contribution to thermal conductance is maximized. This "peaked" behavior affords some opportunity to design the nanostructure modulation such that phonon transmission is minimized at the wavenumbers that deliver maximum contribution to thermal conductance. Such targeted reduction in phonon transport via tuning d is not possible at higher temperatures (as discussed in section 6.5.2) since many more modes contribute to the thermal conductance and the interactions of one mode or one band of modes has a less significant effect on

overall thermal transport. This effect accounts for the relative insensitivity of the classical conductance ratio on modulation length.

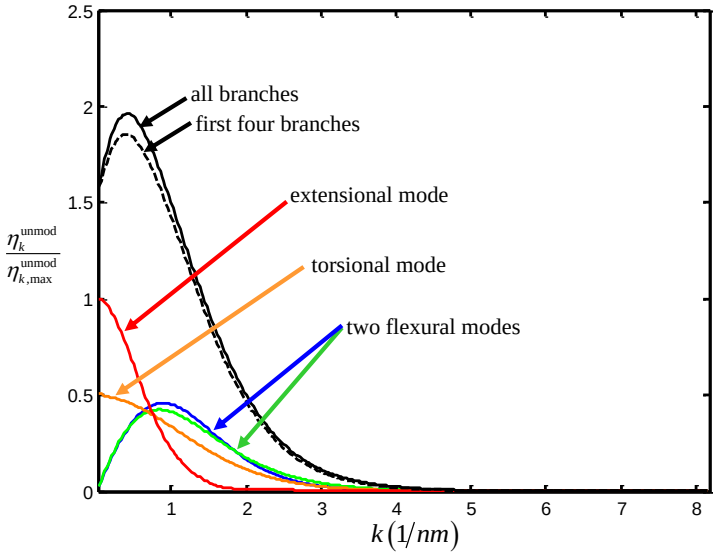

Figure 6.17: Normalized modal contributions to thermal conductance for an unmodulated nanowire (D_I=1.72 nm) at T=12K. The first four branches dominate thermal transport in this regime and account for the nearly all of the contribution to thermal conductance. The extensional and torsional modes' contribution is maximum at k=0, while the two flexural modes do not contribute at k=0 due to their low group velocities. The combined contribution of the four zeroth order modes results in a wavenumber peak at k=0.42 (1/nm).

To demonstrate enhanced dependence of σ^* on modulation length at lower temperatures and the ability to target a particular band of modes, the conductance ratio versus modulation length is plotted versus d for a low temperature (T=12K) case (Figure 6.18). Both the N=1 and N=2 cases are considered. At this temperature, the thermal conductance is dominated by the behavior of the peak modes and therefore exhibits greater dependence on modulation length than at classical temperatures (Figure 6.12). While the variability of the conductance ratio with d is still small relative to the characteristic changes in conductance that occur due to changing the size ratio or the

number of modulations, a clear minimum in the conductance ratio is discernible. For both the N=1 and N=2 cases, the minimum thermal conductance ratio occurs at around $d \approx 2.3$ nm. This minimum can be understood through analysis of Figure 6.19. This figure shows the modal contributions to thermal conductance, the differential modal contribution to thermal conductance, and the modal transmission coefficients for unmodulated nanowires and nanowires with one or two modulations. A local minimum in thermal conductance is obtained when the modulation length, *d*, causes a strong transmission minimum in the extensional and torsional phonon branches that is well aligned with the wavenumbers of the dominant phonon modes. Contrastingly, when the modulation length is chosen such that the resultant minimum in the transmission of the extensional and torsional branches is not aligned with the peak wavenumber (Figure 6.19: Case B), the conductance ratio is appreciably larger. As Figure 6.18 and Figure 6.20 show the effect is greater for N=2 case since the additional modulation results in a deeper transmission valley (Figure 6.20) which causes a greater differential between the conductance of the unmodulated nanowire and the modulated nanowire near the peak wavenumber band. Note that the behavior of the two flexural modes does not impact this analysis since they exhibit less variability in transmission at low frequencies (see, for example, Figure 5.9 and Figure 6.15). Thus, at low wavenumbers their transmission is relatively high irrespective of *d* which affords less opportunity to tune the conductance of these modes.

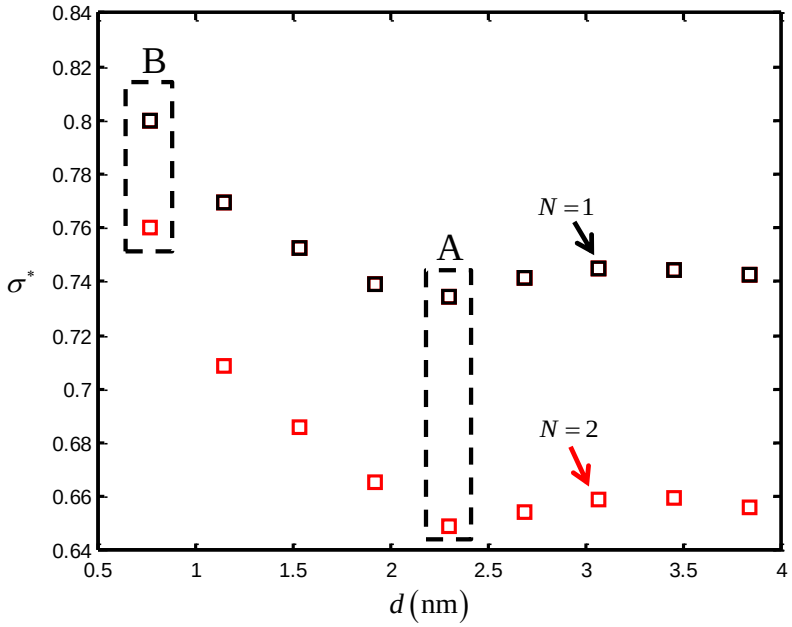

Figure 6.18: Conductance versus modulation length for T=12K. D_I is 1.72 nm and D_{II} is 2.37 nm. Boxed cases correspond to plots shown in Figure 6.19 and Figure 6.20.

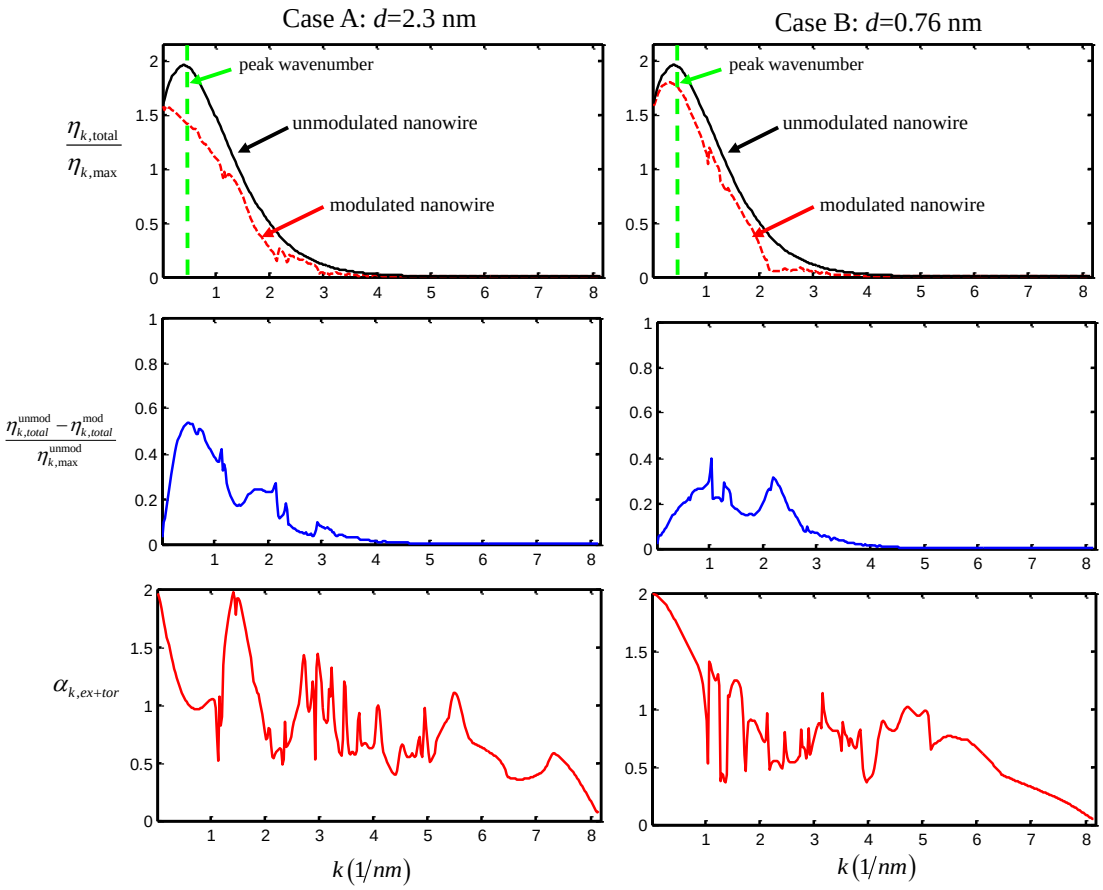

Figure 6.19: Normalized contribution to thermal conductance (top row), differential contribution to thermal conductance (middle row) and combined phonon transmission of extensional and torsion phonon branches (bottom row). Each column corresponds to the cases boxed in Figure 6.18. Contribution to thermal conductance is normalized by the mode that is the maximum contributor to thermal conductance in the straight nanowire at temperature of interest (T=17 K). For the case shown, the maximum contributors are the longest wavelength modes belonging to the extensional branch. N=1, D_I=1.72 nm and D_{II}=2.37 nm.

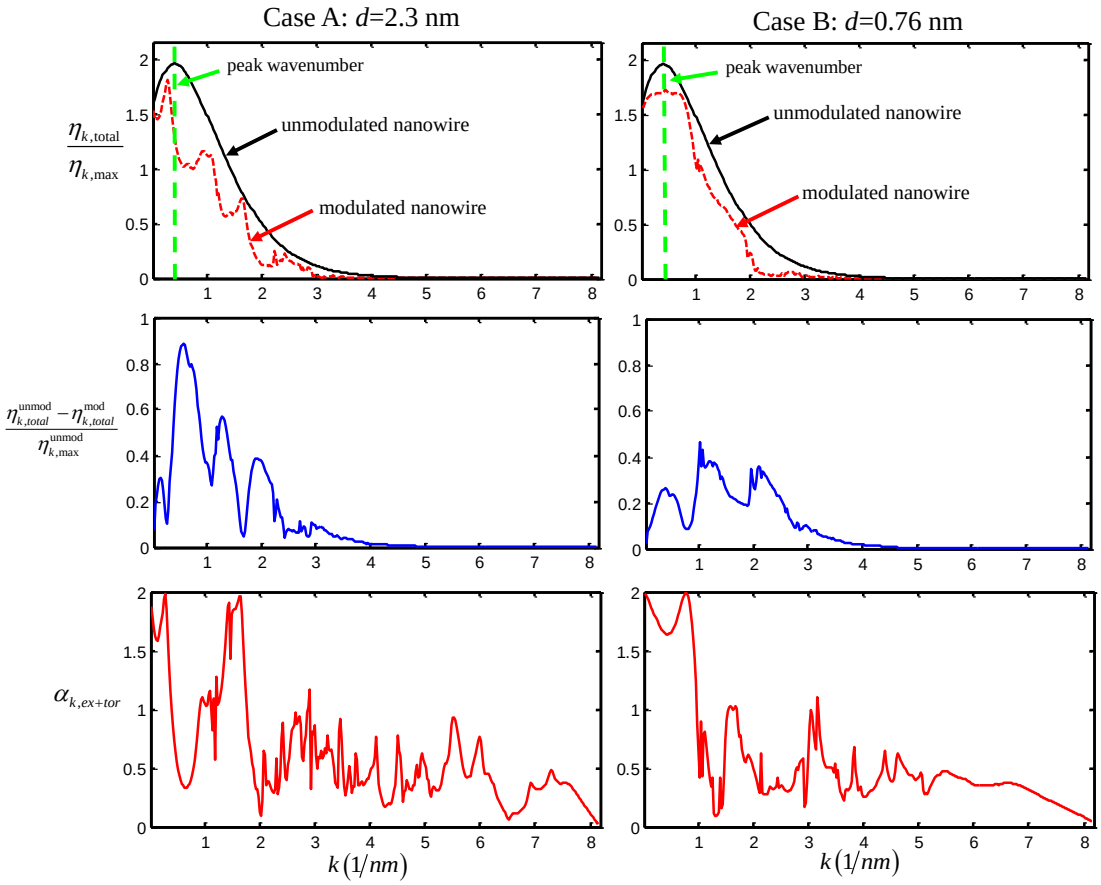

Figure 6.20: Normalized contribution to thermal conductance (top row), differential contribution to thermal conductance (middle row) and combined phonon transmission of extensional and torsion phonon branches (bottom row). Each column corresponds to the cases boxed in Figure 6.18. For this case, N=2, D_I=1.72 nm and D_{II}=2.37 nm. The phonon suppression effect is stronger than for the N=1 case. Inspection of the differential contribution to thermal conductance plot for each case demonstrates that d can be chosen to target the dominant band of phonon modes at this temperature.

6.6 Proposed Framework for a Simple Phonon Transmission Model

It was noted in section 6.4.2 that the dependence of the total phonon transmission on frequency is dominated by the number of modes at a given frequency rather than being characterized by any strong wavenumber or mode type dependence. This results from the fact that there are, in general, a very large number of modes present at a given frequency such that the total phonon transmission at each frequency manifests itself as an

average over many modes. The most important exception to this type of behavior occurs for the zeroth order phonons modes whose long wavelength behavior is adequately described by the beam theory model developed in Chapter 5. These two observations provide inspiration for a simplified model for phonon transmission whereby the phonon transmission is approximated by:

$$\alpha_{\omega,\nu}^{simple} = \begin{cases} \alpha_{\omega,\nu}^{beam} & \text{for } \omega \le \frac{1}{2}\ \omega_c \\ \alpha_c & \text{for } \omega > \frac{1}{2}\ \omega_c \end{cases} \tag{67}$$

Here $\alpha_{\omega,\nu}^{simple}$ is approximated by the transmission, $\alpha_{\omega,\nu}^{beam}$, as estimated by the simple beam theory model developed in Chapter 5 for phonons with frequencies less than or equal to one half the cutoff frequency of the first higher order mode, ω_c. The transmission coefficients of all other modes are modeled by a constant phonon transmission, α_c. Since the classical conductance ratio, σ_C^*, can be thought of as a frequency dependent number of modes weighted average transmission (see Eq. (65)) it serves as an appropriate choice for α_c. For illustration of this simplified model, $\alpha_{\omega,\nu}^{simple}$ is plotted with the actual phonon transmission as calculated using the LD-SBM method in Figure 6.21. The total phonon transmission associated with the simple model is obtained by multiplying $\alpha_{\omega,\nu}^{simple}$ by the number of modes, N_ω. As shown in Figure 6.21(a) the simple model is able to capture most of the character of the more rigorously calculated phonon transmission curve.

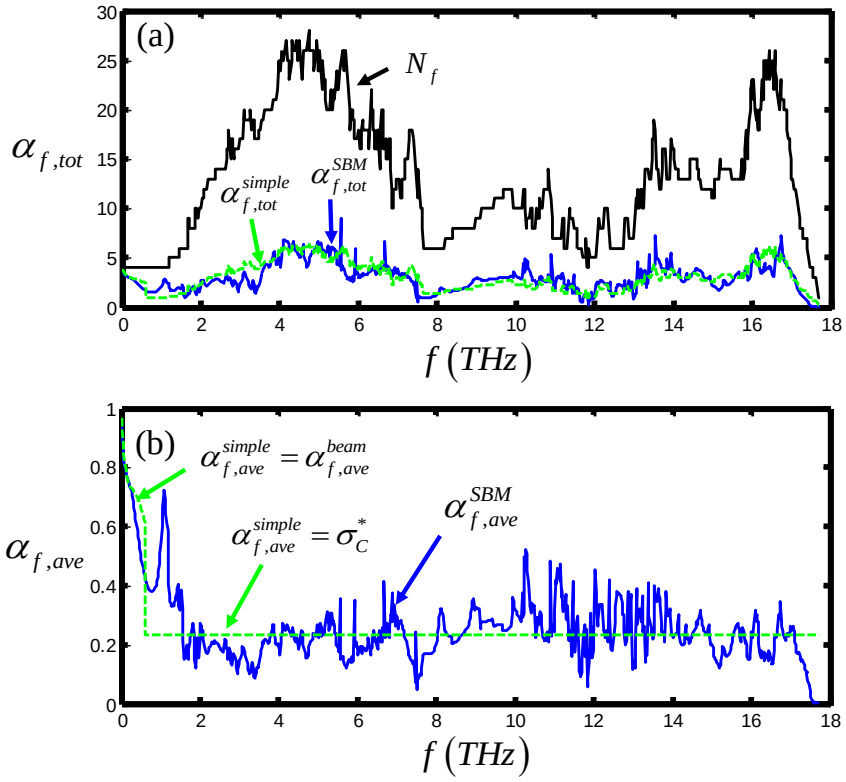

Figure 6.21 (a) total phonon transmission as a function of frequency for both the LD-SBM model and the simple model which is described in Eq. (67). (b) average phonon transmission as a function of frequency for both models. Simple model uses a constant value for all modes greater than one half the cutoff frequency of the first higher order mode. Beam theory is used to model the low frequency transmission. Since the transmission is plotted as a function of ordinary frequency, *f*, the number of phonon modes and the transmission coeffiecients are indexed using ordinary frequency.

To demonstrate the application of the simple model toward the calculation of the thermal conductance, the thermal conductance versus temperature is plotted for three different example geometries in Figure 6.22. In all three cases, the result from the simple model gives a good approximation for the full calculation obtained from the detailed LD-SBM calculations of the phonon transmission of every mode. A more expansive survey of how well the simple model matched the conductance results was performed for the 71

different geometric combinations of D_I, D_{II}, d, and N presented herein. The conductance results were compared over a temperature range of 1 to 400 K and the average error, δ_{ave}, and maximum error, $\delta_{\max}$, over the temperature range as a percentage of the unmodulated nanowire's thermal conductance (of equivalent D_I) was calculated. The average value of δ_{ave} for the 71 geometries surveyed was 3.7% and the average value of $\delta_{\max}$ for the 71 geometries surveyed was 9%. The maximum error always occurred at lower temperatures (T<30K) and coincided with the transition between the regime that can be adequately modeled using beam theory and the classical regime which is effectively characterized by σ_C^*.

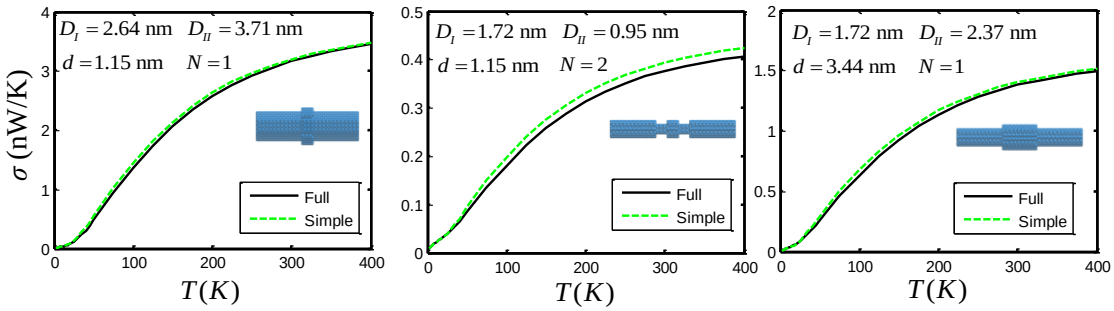

Figure 6.22: Comparison of simple transmission model with LD-SBM for the calculation of thermal conductance. The results for three different example geometries are presented.

The advantage of this simple model is that the thermal conductance can be estimated for all temperatures without the need to calculate the phonon transmission of every mode. Since the beam model has been clearly presented in Chapter 5, all that is needed to estimate the conductance are appropriate models for the phonon spectra of the nanowire leads and an understanding of how σ_C^* varies with geometry. Phonon spectra,

which are required to calculate N_ω, ω, and ω_c can be found using harmonic lattice dynamics and the methods described in Chapter 2 of this dissertation. Harmonic lattice dynamics calculations of nanowire phonon spectra, while still computationally demanding, are considerably less complicated calculations to perform than the SBM calculations that are required to determine the modal transmission coefficients. Open source computer programs are also available to aid in the determination of phonon spectra [108]. While additional future research is required to develop a comprehensive description of how the key geometric parameters affect σ_C^*, the trends that emerged from the study undertaken in this chapter suggest that empirical/analytical models relating D_I, D_{II}, d, and N to σ_C^* are probably within reach.

6.7 Summary

In this chapter, the LD-SBM computational model that was described in Chapters 2 and 3 of this dissertation was used to calculate phonon transmission and thermal conductance through a modulated nanowire system. Detailed results were presented for a baseline constricted nanowire and the effect of structural relaxation was investigated. Higher relaxation temperatures resulted in greater reorganization of the atomic configuration, enhanced suppression of higher frequency phonon modes, and reduced conductance relative to the base unrelaxed structure. However, structural relaxation was shown to have little effect on the transmission of low frequency phonons and low temperature overall thermal transport. The model was then used to explore the effect of

several geometric parameters on the overall suppression of the phonon transport. The results show that the most important parameter influencing phonon transport in these systems is the size ratio between the modulated section and the nanowire lead. The number of modulations is also a dominant parameter in the governance of phonon transport. Consistent with the previously published results of Zianni and an analysis of phonon transmission using a simple beam theory model, the LD-SBM results showed that multiple modulations result in reduced aggregate phonon transmission and that the reduction saturates for larger values of N. While varying the modulation length can be used to tune the transmission behavior of individual phonon branches, its effect on overall thermal transport is negligible except at low temperatures where only the zeroth order branches are strong contributors to the modal specific heat. This study demonstrated that thermal conductance is slightly tunable at low temperatures by manipulation of modulation length through the selected targeting of dominant wavenumber modes. In addition to surveying geometrical effects on phonon transport in the diameter modulated nanowire, a framework for a simple model for phonon transmission was proposed that could be useful by eliminating the need to perform detailed phonon transmission calculations while still providing an adequate description of how geometry affects aggregate phonon transport.

7 Conclusion

7.1 Contributions

The following is a summary of the most important contributions made by this dissertation.

This dissertation presented an implementation of an atomistic and mode-dependent computational model for calculating phonon transmission in geometrically irregular confined silicon nanostructures. Prior to this work, the LD-SBM approach had only been used to calculate modal phonon transmission across bulk material interfaces and nanotube junctions. The vast majority of previous computational and theoretical investigations on coherent phonon-geometry interactions in confined nanostructures and their implications to thermal transport have either relied on MD simulation or transmission results based on continuum elastic wave theory. The computational approach implemented for this dissertation is an improvement over conventional MD in that it can analyze specific mode behavior and it is an improvement over the continuum approach since the effects of the discrete lattice are taken in account. While similar work had been done before via an "Atomistic Green's Functions" (AGF) formulation, the AGF approach only produces frequency dependent phonon transmission and is thus unable to isolate the wavenumber/wavelength or mode type dependent behavior of individual modes. The computational model implemented for this dissertation enabled the investigation of how individual modes interact with irregular geometric features. This

new computational capability aids in understanding fundamental phonon-geometry scattering processes, and has implications to nanostructure design by linking the properties and transmission behavior of individual modes to the size and shape of individual geometric features. In addition, the mode dependent capability of the model allowed for mode-level comparisons with alternative computational methods.

This dissertation, along with a corollary work (Ref. [93]), presented the first ever comparison of atomistic and continuum models for the calculation of mode-dependent phonon transmission in geometrically irregular nanostructures. The comparison of methods enabled the critical evaluation of a computational approach that has been used by many previous researchers to predict phonon transport in nanoscale systems. The comparison confirmed the accuracy of the continuum models for the analysis of long wavelength acoustic phonons, but indicated that continuum models should only be used to model phonons with wavelengths greater than around 4-8 nm. This dissertation also presented a detailed accounting of the various wavelength and nanostructure size dependent atomistic effects that can cause deviations between an atomistic and continuum model and proposed an original simple model that can be used to estimate an upper bound on continuum model error due to dimensional uncertainty when modeling a nanoscale system.

Another key contribution of this work was the creation of an original simple analytical model based on long wavelength beam theory that can be used to estimate modal phonon transmission coefficients in geometrically irregular nanowires. The model

was generalized so that it may be applied for systems with an arbitrary number of abrupt geometric or material discontinuities. In addition to the general formulation, some closed form analytical expressions for modal phonon transmission were derived for systems of reduced geometric complexity. The simple model provides a pathway for other researchers and engineers to investigate the effect of material and geometric discontinuities on thermal transport without requiring complicated and computationally expensive atomistic transmission calculations.

Lastly, this dissertation presented a focused investigation of the geometric parameter space that governs phonon transport in diameter modulated silicon nanowires. In addition to presenting and analyzing detailed transmission and thermal conductance results, a general framework was proposed that can be used to estimate temperature dependent thermal conductance through a geometrically irregular nanowire without the need for tedious and computationally expensive atomistic calculations. Such an approach could be used as a guideline for future analysis and characterization of geometrical effects on phonon transport in modulated nanowire systems. The analytical framework could also be applied to other related nanoscale systems such as nanowire superlattices.

7.2 Suggestions for future work

The lattice dynamics - scattering boundary method computational tool, as currently written and utilized for the writing of this dissertation, can only analyze phonon transport and predict thermal properties in very small nanostructures. The largest nanowires that

can currently be investigated in a reasonable amount of time (i.e. calculating phonon transmission for enough modes to determine the thermal conductance in less than a week) have diameters between 3 and 5 nm depending on the length and complexity of the irregular geometry and the desired level of frequency or wavenumber dependent resolution. Because of the computational savings associated with the additional periodicity of plate-like nanostructures, plates with confined height between 15 and 20 nm can currently be simulated. While these sizes are large enough to capture most of the relevant physics, perform comparisons with continuum theory, and gain general insight regarding phonon transmission and thermal conductance, they are probably not large enough to be compared with experimental results. Optimizing the code and executing on tens or hundreds of processors could enable validation of the computations via comparison with experimental results and open the possibility to simulate mode dependent phonon scattering in larger, more elaborate nanoscale systems.

Because the focus of this dissertation was to develop and compare computational tools, not exhaustively use them to investigate geometries, only a narrow portion of the possible geometry design space was investigated. Since much of the interest in the geometrical investigation thus far was in the concurrent development and comparison with simple analytical models, the geometries investigated thus far have all had abrupt interfaces with intermediate sections that had constant cross-section. Investigating smoothly varying geometries, nanostructures with randomly rough boundaries, and nanostructures with amorphous layers would provide a better match to nanostructures

currently attainable in the laboratory and expand the structural-geometry design space. Fortunately, because of the atomistic nature of the computational method, additional geometric and material complexity could easily be included in the model.

The focus of this dissertation was on creating a computational model for geometry dependent phonon transport in nanostructures. However, the LD-SBM model that was deployed for geometrically irregular nanostructures could easily be adapted to investigate phonon transmission in nanowire systems comprised of more than one material such as nanowire superlattices. Nanowire superlattices are nanowires comprised of alternating, periodic layers of different materials. Thermal conductivity measurements of Si-SiGe nanowire superlattices were performed by Li, et. al [109] , and because of their low thermal conductivities relative to nanowires comprised only of silicon, have been proposed for use in higher efficiency thermoelectric materials. The phonon thermal conductivity of superlattice nanowires has been investigated theoretically through incoherent phonon particle models [110] and through non-equilibrium molecular dynamics simulation [111]. Greater insight concerning their potential to serve as a medium for tuned thermal transport could be found through a LD-SBM based computational study whereby the transmission of individual modes could be calculated. Such an approach would fully account for confined phonon spectra (not included in the particle approach) and low temperature phonon occupation (not accounted for in the MD approach). Additionally, the beam theory model developed in Chapter 5 of this work could also be easily applied to nanowire superlattice systems. Expanding the

nanostructure design space to include the possibility for varying material properties as well as boundary geometry may enable increased tunability of phonon transport and could result in structures that suppress phonon transport even more than nanowires comprised of single materials.

8 References

1. Ju Y. S., and Goodson K. E., 1999, "Phonon scattering in silicon films with thickness of order 100 nm," Applied Physics Letters, **74**, p. 3005-3007.

2. Liu W., and Asheghi M., 2006, "Thermal conductivity measurements of ultra-thin single crystal silicon layers," Journal of heat transfer, **128**, pp. 75-83.

3. Li D., Wu Y., Kim P., Shi L., Yang P., and Majumdar A., 2003, "Thermal conductivity of individual silicon nanowires," Applied Physics Letters, **83**, pp. 2934-2936.

4. Chen R., Hochbaum A. I., Murphy P., Moore J., Yang P., and Majumdar A., 2008, "Thermal conductance of thin silicon nanowires," Physical Review Letters, **101**, 105501.

5. Hochbaum A. I., Chen R., Delgado R. D., Liang W., Garnett E. C., Najarian M., Majumdar A., and Yang P., 2008, "Enhanced thermoelectric performance of rough silicon nanowires," Nature, **451**, pp. 163–167.

6. Park Y. H., Kim J., Kim H., Kim I., Lee K. Y., Seo D., Choi H. J., and Kim W., 2011, "Thermal conductivity of VLS-grown rough Si nanowires with various surface roughnesses and diameters," Applied Physics A: Materials Science & Processing, **104**, pp. 7–14.

7. Blanc, C., Rajabpour, A., Volz, S., Fournier, T., & Bourgeois, O., 2013, "Phonon Heat Conduction in Corrugated Silicon Nanowires Below the Casimir Limit" *arXiv preprint arXiv:1302.4422*.

8. Heron J. S., Bera C., Fournier T., Mingo N., and Bourgeois O., 2010, "Blocking phonons via nanoscale geometrical design," Physical Review B**, 82**, 155458.

9. Yadav G. G., Susoreny J. A., Zhang G., Yang H., and Wu Y., 2011, "Nanostructure-based thermoelectric conversion: an insight into the feasibility and sustainability for large-scale deployment," Nanoscale, **3**, pp. 3555–3562.

10. Boukai A. I., Bunimovich Y., Tahir-Kheli J., Yu J. K., Goddard Iii W. A., and Heath J. R., 2008, "Silicon nanowires as efficient thermoelectric materials," Nature, **451**, pp. 168–171

11. De Padova P., Quaresima C., Perfetti P., Olivieri B., Leandri C., Aufray B., Vizzini S., and Le Lay G., 2008, "Growth of Straight, Atomically Perfect, Highly Metallic Silicon Nanowires with Chiral Asymmetry," Nano letters, **8**, pp. 271–275.

12. Wang N., Zhang Y., Tang Y., Lee C., and Lee S., 1998, "SiO-enhanced synthesis of Si nanowires by laser ablation," Applied physics letters, **73**, p. 3902-3904.

13. Wu Y., Cui Y., Huynh L., Barrelet C. J., Bell D. C., and Lieber C. M., 2004, "Controlled growth and structures of molecular-scale silicon nanowires," Nano Letters, **4**, pp. 433–436.

14. Trivedi K., Yuk H., Floresca H. C., Kim M. J., and Hu W., 2011, “Quantum Confinement Induced Performance Enhancement in Sub-5-nm Lithographic Si Nanowire Transistors,” Nano letters. 11(4):1412-7.

15. Li F., Nellist P. D., Lang C., and Cockayne D. J. H., 2010, “Dependence of Surface Facet Period on the Diameter of Nanowires,” ACS nano, **4**(2), pp. 632–636.

16. Peng H., Wang N., Shi W., Zhang Y., Lee C., and Lee S., 2001, “Bulk-quantity Si nanosphere chains prepared from semi-infinite length Si nanowires,” Journal of Applied Physics, **89**, p. 727.

17. Ghosh A., “Glancing Angle Deposition (GLAD): Nano Structures and Applications.” IWSG 2010 <http://www.nnin.org/doc/iWSG_2010/Day4_1400_Ghosh_GLAD.pdf>

18. Cumming D., Thoms S., Beaumont S., and Weaver J., 1996, “Fabrication of 3 nm wires using 100 keV electron beam lithography and poly (methyl methacrylate) resist,” Applied physics letters, **68**, p. 322.

19. Yazji S., Zardo I., Soini M., Postorino P., Fontcuberta i Morral A., and Abstreiter G., 2011, “Local modification of GaAs nanowires induced by laser heating,” Nanotechnology, **22**, 325701.

20. Wang D., Qian F., Yang C., Zhong Z., and Lieber C. M., 2004, “Rational growth of branched and hyperbranched nanowire structures,” Nano Letters, **4**, pp. 871–874.

21. Tian B., Xie P., Kempa T. J., Bell D. C., and Lieber C. M., 2009, "Single-crystalline kinked semiconductor nanowire superstructures," Nature nanotechnology, **4**, pp. 824–829.

22. Turney, J., 2009, "Prediction Phonon Properties and Thermal Conductivity Using Anharmonic Lattice Dynamics Calculation," Ph.D. Dissertation, Carnegie Mellon University, Pittsburgh, PA.

23. Ziman J. M., 2000, Electrons and phonons: the theory of transport phenomena in solids, Oxford University Press, New York, NY.

24. Moore A. L., Saha S. K., Prasher R. S., and Shi L., 2008, "Phonon backscattering and thermal conductivity suppression in sawtooth nanowires," Applied Physics Letters, **93**, pp. 083112–083112.

25. Chen Y., Li D., Lukes J. R., and Majumdar A., 2005, "Monte Carlo simulation of silicon nanowire thermal conductivity," Journal of heat transfer, **127**, pp. 1129-1137.

26. Roberts N., and Walker D., 2011, "Phonon transport in asymmetric sawtooth nanowires." Proceedings of ASME/JSME 2011 8th Thermal Engineering Joint Conference, March 13-17, Honolulu, Hawaii, AJTEC2011-44341.

27. Allen, M.P., and Tildesley, D.J., 1987, Computer simulation of liquids, Clarendon Press, Oxford.

28. Gomes C. J., Madrid M., Goicochea J. V., and Amon C. H., 2006, "In-plane and out-of-plane thermal conductivity of silicon thin films predicted by molecular dynamics," Journal of heat transfer, **128**, pp. 1114-1121.

29. Volz S. G., and Chen G., 1999, "Molecular dynamics simulation of thermal conductivity of silicon nanowires," Applied Physics Letters, **75**, pp. 2056-2058.

30. Donadio D., and Galli G., 2010, "Temperature dependence of the thermal conductivity of thin silicon nanowires," Nano Letters, **10**, pp. 847–851.

31. Wang S., Liang X., Xu X., and Ohara T., 2009, "Thermal conductivity of silicon nanowire by nonequilibrium molecular dynamics simulations," Journal of Applied Physics, **105**, p. 014316–014316.

32. Thomas J. A., Iutzi R. M., and McGaughey A. J. H., 2010, "Thermal conductivity and phonon transport in empty and water-filled carbon nanotubes," Physical Review B, **81**, 045413.

33. Sevik C., Sevinçli H., Cuniberti G., and Cagin T., 2011, "Phonon engineering in carbon nanotubes by controlling defect concentration," Nano Letters. **11** pp. 4971-4977.

34. Liu L., and Chen X., 2010, "Effect of surface roughness on thermal conductivity of silicon nanowires," Journal of Applied Physics, **107**, 033501.

35. Qiu B., Sun L., and Ruan X., 2011, "Lattice thermal conductivity reduction in Bi2Te3 quantum wires with smooth and rough surfaces: A molecular dynamics study," Physical Review B, **83**, 035312.

36. Evans W. J., Hu L., and Keblinski P., 2010, "Thermal conductivity of graphene ribbons from equilibrium molecular dynamics: Effect of ribbon width, edge roughness, and hydrogen termination," Applied Physics Letters, **96**, 203112.

37. Huang Z., Yu J., and Bai S., 2011, "Temperature-dependent thermal conductivity of bent carbon nanotubes by molecular dynamics simulation," Journal of Applied Physics, **109**, 104316.

38. He, Y., & Galli, G., 2012, "Microscopic Origin of the Reduced Thermal Conductivity of Silicon Nanowires," Physical Review Letters, **108**, 215901.

39. Termentzidis, K., Barreteau, T., Ni, Y., Huedro, H., Delaye, A. L., Zianni, X., Chalopin, Y., Chantrenne, P., Volz, S., 2012, "Thermal conductivity and Kapitza resistance of diameter modulated SiC nanowires, a molecular dynamics study," Journal of Physics: Conference Series **395**, 012107.

40. Rego, L. G., & Kirczenow, G., 1998, "Quantized thermal conductance of dielectric quantum wires" Physical Review Letters, **81**, 232-235.

41. Nishiguchi, N., Ando, Y. and Wybourne, M.N., 1997, "Acoustic phonon modes of rectangular quantum wires," Journal of Physics: Condensed Matter, **9**, pp. 5751-5764.

42. Turney J., McGaughey A., and Amon C., 2010, “In-plane phonon transport in thin films,” Journal of Applied Physics, **107**, 024317.

43. Sellan D., Turney J., McGaughey A., and Amon C., 2010, “Cross-plane phonon transport in thin films,” Journal of Applied Physics, **108**, p. 113524.

44. Dove M. T., 1993, Introduction to lattice dynamics, Cambridge University Press, New York, NY.

45. Tersoff, J., 1988, “Empirical interatomic potential for silicon with improved elastic properties,” Physical Review B, **38**, pp. 9902-9905.

46. Bazant, M. Z., Kaxiras, E., & Justo, J. F., 1997, “Environment-dependent interatomic potential for bulk silicon,” Physical Review B, **56**, pp. 8542-8551.

47. Baskes, M. I., Nelson, J. S., & Wright, A. F. (1989). “Semiempirical modified embedded-atom potentials for silicon and germanium,” Physical Review B, **40**, pp. 6085-6100.

48. Stillinger, F.H., and Weber, T.A., 1985, “Computer simulation of local order in condensed phases of silicon,” Physical Review B, **31**, pp. 5262–5271.

49. Cook, S. J., & Clancy, P., 1993, “Comparison of semi-empirical potential functions for silicon and germanium,” Physical Review B, **47**, 7686-7699.

50. Thomas, J. A., Turney, J. E., Iutzi, R. M., Amon, C. H., and McGaughey, A. J. H., 2010 "Predicting phonon dispersion relations and lifetimes from the spectral energy density." Physical Review B, **81,** 081411.

51. Cheney, D. A., & Lukes, J. R., 2012., "Excitation of Single Phonon Modes in Nanoscale Waveguides" Journal of Heat Transfer, **134**, 042403.

52. Kong, L. T., 2011, "Phonon dispersion measured directly from molecular dynamics simulations," Computer Physics Communications, **182**, pp. 2201-2207.

53. Solie, L.P., and Auld, B.A., 1973, "Elastic waves in free anisotropic plates," The Journal of the Acoustical Society of America, **54**, pp. 50-65.

54. Auld, B.A., 1990, Acoustic Waves and Fields in Solids Vol. 2, Krieger Publishing Company, Malabar, FL.

55. Cowley, E.R., 1998, "Lattice dynamics of silicon with empirical many-body potentials," Physical Review Letters **60**, 2379–2381.

56. Li W. X., Chen K. Q., Duan W., Wu J., and Gu B. L., 2004, "Acoustic phonon transport through a T-shaped quantum waveguide," Journal of Physics: Condensed Matter, **16**, p. 5049-5059.

57. Yang P., Sun Q., Guo H., and Hu B., 2007, "Thermal transport in a dielectric T-shaped quantum wire," Physical Review B, **75**, 235319.

58. Xie F., Chen K. Q., Wang Y. G., and Zhang Y., 2008, "Effect of the evanescent modes on ballistic thermal transport in quantum structures," Journal of Applied Physics, **103**, 084501.

59. Zou M. L., Huang W. Q., Huang G. F., Yao J. J., and Zhang J. H., 2011, "Ballistic phonon transmission in a symmetric converging–diverging contact of a semiconductor nanowire," Journal of Physics D: Applied Physics, **44**, 105102.

60. Li W. X., Liu T., and Liu C., 2006, "Phonon transport through a three-dimensional abrupt junction," Applied physics letters, **89**, 163104.

61. Liu Z., Yu X., and Chen K., 2009, "Thermal transport associated with ballistic phonons in asymmetric quantum structures," Frontiers of Physics in China, **4**, pp. 420–425.

62. Tang L. M., Wang L. L., Chen K. Q., Huang W. Q., and Zou B. S., 2006, "Coupling effect on phonon thermal transport in a double-stub quantum wire," Applied Physics Letters, **88**, 163505.

63. Huang W. Q., Huang B. Y., Yi D. Q., Wang M. P., Huang G. F., and Wang L. L., 2009, "Selective transmission and enhanced thermal conductance of ballistic phonon by nanocavities embedded in a narrow constriction," Journal of Physics D: Applied Physics, **42**, 015101.

64. Mo Y., Huang W. Q., Huang G. F., Chen Y., Hu W., Wang L. L., and Pan A., 2011, "Ballistic phonon transmission in quasiperiodic acoustic nanocavities," Journal of Applied Physics, **109**, 084310.

65. Mo Y., Huang W. Q., Huang G. F., Hu W., Wang L. L., and Pan A., 2011, "Ballistic phonon transport through a Fibonacci array of acoustic nanocavities in a narrow constriction," Physics Letters A. **375**, pp. 2000-2006.

66. Li S. J., Huang G. F., Huang W. Q., Chen Y., Wang L. L., Hu W., and Pan A., 2011, "Effect of Gaussian acoustic nanocavities in a narrow constriction on ballistic phonon transmission," Applied Physics A: Materials Science & Processing, **104**, pp. 635-642.

67. Huang W. Q., Chen K. Q., Shuai Z., Wang L., Hu W., and Zou B. S., 2005, "Acoustic-phonon transmission and thermal conductance in a double-bend quantum waveguide," Journal of Applied Physics, **98**, 093524.

68. Li W. X., Chen K. Q., Duan W., Wu J., and Gu B. L., 2004, "Acoustic phonon mode splitting behavior of an asymmetric y-branch three terminal junction," Applied Physics Letters, **85**, p. 822-824.

69. Huang W. Q., Yi D. Q., Huang B. Y., Wang M. P., Huang G. F., and Wang L. L., 2008, "Selective transport of ballistic phonon modes by an acoustic nanocavity in a Psi-shaped semiconductor nanowire," Journal of Applied Physics, **104**, 054309.

70. Chen K. Q., Li W. X., Duan W., Shuai Z., and Gu B. L., 2005, "Effect of defects on the thermal conductivity in a nanowire," Physical Review B, **72**, 045422.

71. Li S. H. U. J., Huang G. U. I. F., Chen Y., Huang W. E. I. Q., Hu W., Wang L. L., And Pan A., 2011, "Ballistic Phonon Transport Through Gaussian Acoustic Nanocavities," Modern Physics Letters B, **25**, pp. 1631–1642.

72. Tamura H., and Ando T., 1991, "Conductance fluctuations in quantum wires," Physical Review B, **44**, pp. 1792-1800.

73. Galán J. M., and Abascal R., 2003, "Elastodynamic guided wave scattering in infinite plates," International Journal for Numerical Methods in Engineering, **58**, pp. 1091–1118.

74. Al-Nassar Y. N., Datta S. K., and Shah A. H., 1991, "Scattering of Lamb waves by a normal rectangular strip weldment," Ultrasonics, **29**, pp. 125–132.

75. Zhang W., Mingo N., and Fisher T., 2007, "Simulation of phonon transport across a non-polar nanowire junction using an atomistic Green's function method," Physical Review B, **76**. 195429.

76. Huang Z., Fisher T. S., and Murthy J. Y., 2010, "Simulation of thermal conductance across dimensionally mismatched graphene interfaces," Journal of Applied Physics, **108**, 114310.

77. Huang Z., Fisher T. S., and Murthy J. Y., 2010, "Simulation of phonon transmission through graphene and graphene nanoribbons with a Green's function method," Journal of Applied Physics, **108**, 094319.

78. Zhang W., Fisher T. S., and Mingo N., 2007, "Simulation of Interfacial Phonon Transport in Si–Ge Heterostructures Using an Atomistic Green's Function Method," Journal of Heat Transfer, **129**, pp. 483-491.

79. Khomyakov P., Brocks G., Karpan V., Zwierzycki M., and Kelly P., 2005, "Conductance calculations for quantum wires and interfaces: Mode matching and Green's functions," Physical Review B, **72**, 035450.

80. Wang J. S., Wang J., and Lü J. T., 2008, "Quantum thermal transport in nanostructures," The European Physical Journal B-Condensed Matter and Complex Systems, **62**, pp. 381–404.

81. Zhao H., and Freund J. B., 2005, "Lattice-dynamical calculation of phonon scattering at ideal Si–Ge interfaces," Journal of Applied Physics, **97**, 024903.

82. Landry E. S., 2009, "Thermal transport by phonons across semiconductor interfaces, thin films, and superlattices," Ph.D. Dissertation, Carnegie Mellon University, Pittsburgh, PA.

83. Young D. A., and Maris H. J., 1989, "Lattice-dynamical calculation of the Kapitza resistance between fcc lattices," Physical Review B, **40**, p. 3685.

84. Landry E., and McGaughey A., 2010, "Effect of film thickness on the thermal resistance of confined semiconductor thin films," Journal of Applied Physics, **107**, 013521.

85. Wang J., and Wang J. S., 2006, "Mode-dependent energy transmission across nanotube junctions calculated with a lattice dynamics approach," Physical Review B, **74**, 054303.

86. Khater A., Belhadi M., and Abou Ghantous M., 2011, "Phonons heat transport at an atomic well boundary in ultrathin solid films," The European Physical Journal B-Condensed Matter and Complex Systems, **80**, pp. 363–369.

87. Schelling P. K., Phillpot S. R., and Keblinski P., 2002, "Phonon wave-packet dynamics at semiconductor interfaces by molecular-dynamics simulation," Applied Physics Letters, **80**, pp. 2484-2486.

88. Becker B., Schelling P. K., and Phillpot S. R., 2006, "Interfacial phonon scattering in semiconductor nanowires by molecular-dynamics simulation," Journal of Applied Physics, **99**, 123715.

89. Kondo N., Yamamoto T., and Watanabe K., 2006, "Phonon wavepacket scattering dynamics in defective carbon nanotubes," Japanese Journal of Applied Physics, **45**, pp. 963–965.

90. Zuckerman N., and Lukes J. R., 2008, "Acoustic phonon scattering from particles embedded in an anisotropic medium: A molecular dynamics study," Physical Review B, **77**, 094302.

91. Tian Z. T., White B. E., and Sun Y., 2010, "Phonon wave-packet interference and phonon tunneling based energy transport across nanostructured thin films," Applied Physics Letters, **96**, 263113.

92. Mingo, N., 2008, "Calculation of Si Nanowire Thermal Conductivity Using Complete Phonon Dispersion Relations," Physical Review B, **68**, 113308.

93. Cheney, D.A., and Lukes, J.R., 2013, "Comparison of Atomistic and Continuum Methods for Calculating Ballistic Phonon Transmission in Nanoscale Waveguides**,"** Journal of Heat Transfer, **135**, 091101.

94. Ku, H.H., 1966, "Notes on the use of propagation of error formulas," Journal of Research of the National Bureau of Standards, **70C**, pp. 263-273.

95. Achenbach, J. D., 1984, Wave propagation in elastic solids, Elsevier Scientific Publishers, Amsterdam, Netherlands.

96. Fung, Y.C., 1965, Foundations of Solid Mechanics, Prentice-Hall, Englewood Cliffs, N.J.

97. Cross, M. C., & Lifshitz, R., 2001, "Elastic wave transmission at an abrupt junction in a thin plate with application to heat transport and vibrations in mesoscopic systems," Physical Review B, **64**, 085324.

98. Mavaddat, R. 1996, Network Scattering Parameters Vol. 2, World Scientific Publishing Company Incorporated, Hackensack, NJ.

99. Auld, B.A., 1990, Acoustic Waves and Fields in Solids Vol. 1, Krieger Publishing Company, Malabar, FL.

100. Svensson, J. L., Andersson, P. B., Scheuren, J., & Kropp, W., 2008, "Active scattering control of flexural waves at beam junctions: The influence of beam properties on power flow and control effort," Journal of Sound and Vibration, **313**, 418-432.

101. Kinsler, L. E., Coppens, A.B., and Sanders, J.V., 1982, Fundamentals of Acoustics, John C. Wiley and Sons, New York, NY.

102. Ugural A.C., and Fenster, S.K., 1995, Advanced Strength and Applied Elasticity, Prentice Hall PTR, Upper Saddle River, NJ.

103. Nika, D. L., Cocemasov, A. I., Isacova, C. I., Balandin, A. A., Fomin, V. M., & Schmidt, O. G., 2012. "Suppression of phonon heat conduction in cross-section-modulated nanowires" Physical Review B, **85**, 205439.

104. Zianni, X. ,2012, "The effect of the modulation shape in the ballistic thermal conductance of modulated nanowires" Journal of Solid State Chemistry, **193**, 53-57

105. S. Plimpton, Fast Parallel Algorithms for Short-Range Molecular Dynamics, J Comp Phys, 117, 1-19 (1995)

106. Large-scale Atomic/Molecular Massively Parallel Simulator, lammps.sandia.gov

107. Fix/heat command: http://lammps.sandia.gov/doc/fix_heat.html

108. Gale, J.D. and Rohl, A.L. "The general utility lattice program (GULP)." Molecular Simulation, **29**, pp. 291-341. <http://projects.ivec.org/gulp/>

109. Li, D, Wu, Y. Fan, R. Yang, P, and Majumdar, A., 2003, "Thermal conductivity of Si/SiGe superlattice nanowires," Applied Physics Letters, 83, pp. 3186-3188

110. Dames, C. and Chen, G., 2004, "Theoretical phonon thermal conductivity of Si/Ge superlattice nanowires, Journal of Applied Physics, **95**, pp. 682-693.

111. Chen, Y., Li, D. Yang, Juekuan, Y, Wu, Y., Lukes, J.R., and Majumdar, A., 2004, "Molecular dynamics study of the lattice thermal conductivity of Kr/Ar superlattice nanowires," Physica B: Condensed Matter, **349**, pp. 270-280.